

# Mixing, Chemical Reactions, and Combustion in Supersonic Flows

Thesis by  
Niccolo Cymbalist

In Partial Fulfillment of the Requirements  
for the Degree of  
Doctor of Philosophy

The logo for the California Institute of Technology (Caltech), featuring the word "Caltech" in a bold, orange, sans-serif font.

California Institute of Technology  
Pasadena, California

2016

(Submitted May 25, 2016)

© 2016

Niccolo Cymbalist

All Rights Reserved

© 2016

Niccolo Cymbalist

All Rights Reserved

To my family.

# Acknowledgements

First and foremost, I would like to thank my advisor, Paul Dimotakis. In addition to providing me with ample resources, technical mentorship, and encouragement when the ‘going got tough’, he gave me a comprehensive education that extends well beyond science and engineering.

I would also like to thank Daniel Lang, whose optics and electronics expertise was critical to the success of the experimental portion of this work.

I very much enjoyed collaborating with Graham Candler on the development of LES-EVM. Seeing the project come to fruition was immensely fulfilling. I also enjoyed working with Elizabeth Luthman on the schlieren image-correlation velocimetry and chemically reacting experiments. Her good humor and attentive eye during the long days spent in the lab are particularly appreciated.

I’d like to thank the machine shop for their fabrication help, as well as Bahram Valiferdowski and Prakhar Mehrotra, who assisted in the early stages of the experimental work.

This work was funded by the Air Force Office of Scientific Research, Grant Nos. FA9550-10-1-0262 and FA9550-12-1-0461. Support was also provided by the NSF Major Research Instrumentation (MRI) Grant EIA-0079871, and the Defense University Research Instrumentation Program (DURIP) AFOSR Grant FA9550-10-1-0553.

# Abstract

Experiments were conducted at the GALCIT supersonic shear-layer facility (S<sup>3</sup>L) to investigate aspects of reacting transverse jets in supersonic crossflow using chemiluminescence and schlieren image-correlation velocimetry. In particular, experiments were designed to examine mixing-delay length dependencies on jet-fluid molar mass, jet diameter, and jet inclination.

The experimental results show that mixing-delay length depends on jet Reynolds number, when appropriately normalized, up to a jet Reynolds number of  $5 \times 10^5$ . Jet inclination increases the mixing-delay length, but causes less disturbance to the crossflow when compared to normal jet injection. This can be explained, in part, in terms of a control-volume analysis that relates jet inclination to flow conditions downstream of injection.

In the second part of this thesis, a combustion-modeling framework is proposed and developed that is tailored to large-eddy simulations of turbulent combustion in high-speed flows. Scaling arguments place supersonic hydrocarbon combustion in a regime of autoignition-dominated distributed reaction zones (DRZ). The proposed evolution-variable manifold (EVM) framework incorporates an ignition-delay data-driven induction model with a post-ignition manifold that uses a Lagrangian convected ‘balloon’ reactor model for chemistry tabulation. A large-eddy simulation incorporating the EVM framework captures several important reacting-flow features of a transverse hydrogen jet in heated-air crossflow experiment.

# List of Figures

1.1	Three-dimensional schematic of a transverse jet in supersonic crossflow (TJISCF), from Gruber et al. (1995) . . . . .	20
2.1	Gas-delivery system diagram (Bond 1991, Fig. A.1) . . . . .	25
2.2	Test-section dimensions, in inches . . . . .	26
2.3	RN1 ( $d_j = 0.20$ in., left), RN2 ( $d_j = 0.25$ in., center), and RI1 ( $d_j = 0.25$ in., right) injector-orifice geometry . . . . .	27
2.4	Optical system combining schlieren/shadowgraph (right-propagating light), and chemiluminescence (left-propagating light, diagram not to scale) . . . . .	29
2.5	Image A (top), and image B (bottom), $\Delta t_{IF} = 6 \mu s$ (Run ss1694) . . . . .	30
2.6	Streamwise velocity component of convected refractive-index interfaces of a helium jet in supersonic nitrogen crossflow (Run ss1694) overlaying a shadowgraphy image of the same flow . . . . .	31
2.7	Binning structure (top) used to produce average convective-velocity estimates (bottom) of Run ss1694. Error bars mark the standard deviation ( $\pm\sigma$ ) of the measured convective velocity within the bin. The freestream velocity is estimated as $U_\infty = 420$ m/s. . . . .	32
2.8	Simulated shadowgraphy image, courtesy of Dr. Elizabeth Luthman . . . . .	33

2.9	Velocity magnitude slice (left), jet-fluid concentration slice (center), and conditional velocity slice (right), derived from the LES results by E. Luthman. The $Y_{\text{He}} = 0.1$ contour is outlined in red. . . . .	34
2.10	Binned SICV measurements using simulated-shadowgraph image pairs, and velocity magnitude of fluid with a jet-fluid mass-fraction of $0.1 < Y_{\text{He}} < 0.9$ . Uncertainty bars in the SICV estimates mark the $\pm\sigma$ estimated convective velocity within each bin. . .	34
2.11	Normalized atomic fluorine and hydrogen mole fractions, and estimated average HNO*+NOF* chemiluminescence in a homogeneous reactor, assuming equal contributions from each species . . . . .	37
2.12	Typical reacting TJICF chemiluminescence image showing the mixing-delay length and jet body (Run ss1708) . . . . .	38
2.13	Chemical timescale for M1 and M2 mixtures, defined as the time at 0.6 of maximum chemiluminescence. See text for details. . . . .	39
2.14	Chemiluminescence, $I_{\text{lum}}$ , and temperature rise, $\Delta T$ , normalized by the adiabatic, equilibrium temperature rise, $\Delta T_{\text{f}}$ , for mixture M1 in Table 2.2, at $T_0 = 200$ K, and $p_0 = 1$ bar. . . . .	40
2.15	Overlaid time-averaged chemiluminescence and schlieren image (Run ss1708) . . . .	41
3.1	From top to bottom, chemiluminescence images of Runs ss1708 (helium jet), ss1714, ss1718, and ss1722 (argon jet). The mixing-delay length decreases with increasing jet-fluid diluent molar mass, $W_{\text{j}}$ . The colorbar scale ranges from 0 to 1 and corresponds to the chemiluminescence intensity normalized by its maximum value. The blue contour is the 0.6 locus of the maximum chemiluminescence signal. . . . .	45
3.2	Jet-fluid molar-mass effects on mixing-delay length. Uncertainty bars represent the individual measurement uncertainties discussed in Section 2.2.2. . . . .	46
3.3	Convective-velocity estimated using SICV. The uncertainty bars represent the typical standard deviation of the convective velocity measurements in the bin, $\pm\sigma$ , at that location (cf. Fig. 2.7) . . . . .	47

3.4	Shear-layer velocity ratio (top left), convective velocity with measured TJISCF near-jet convective velocity (top right), growth rate (bottom left), start of mixing transition ( $Re_\delta > 10^4$ , Konrad 1977, Dimotakis 1991, 2000) in jet diameters, for $d_j=0.2$ in. (bottom right) . . . . .	49
3.5	From top to bottom, chemiluminescence images from $\varpi = 4.11$ (He+N <sub>2</sub> jet fluid) Runs ss1714, $d_j = 0.20$ in. (top) and ss1719, $d_j = 0.25$ in. (center top), from $\varpi = 0.66$ (Ar jet fluid) Runs ss1722, $d_j = 0.20$ in. (center bottom) and ss1720, $d_j = 0.25$ in. (bottom). . . . .	53
3.6	Mixing-delay length normalized by the physical orifice diameter plotted against jet Reynolds number. The uncertainty bars reflect the estimated measurement uncertainty discussed in Section 2.2.2. . . . .	54
3.7	Mixing-delay length normalized by jet-source diameter plotted against jet Reynolds number. The uncertainty bars reflect the estimated measurement uncertainty discussed in Section 2.2.2. . . . .	55
3.8	Mixing-delay length criteria of 0.5 (green), 0.6 (blue), and 0.7 (magenta) of maximum chemiluminescence signal . . . . .	56
3.9	Mixing-delay length normalized by jet-source diameter plotted against jet Reynolds number, for mixing-delay length criteria of 0.5, 0.6, and 0.7 of the maximum chemiluminescence signal. Uncertainty bars omitted for clarity. . . . .	57
3.10	Chemiluminescence images from $\varpi = 4.11$ Runs ss1714, $t_{\text{chem}} = 21\mu\text{s}$ (top) and ss1712, $t_{\text{chem}} = 10\mu\text{s}$ (bottom). . . . .	58
3.11	Chemiluminescence images from Runs ss1719, normal jet (top) and ss1724, 30° inclined jet (bottom). . . . .	61
3.12	Superimposed schlieren and chemiluminescence images from Runs ss1719, normal jet (top) and ss1724, 30° inclined jet (bottom). The $\lambda$ -shock structure ( $\star$ symbol) and spherical acoustic waves emanating from the near field of the jet ( $\triangle$ symbol) are evident in the normal jet-injection case. . . . .	62

3.13	Average (binned) convective velocity from Runs ss1719 (normal jet), and ss1724 (inclined jet). . . . .	63
3.14	Inclined jet-in-crossflow system . . . . .	64
3.15	Velocity, Mach number, total-pressure, and stream thrust function, $Sa$ , change plotted against injection angle, $\theta_j$ . . . . .	66
4.1	Non-premixed hydrocarbon flame (left, Dimotakis 1997, reproduced with permission), and OH-PLIF in a burning ethylene jet in supersonic, heated $O_2$ crossflow (right, Ben-Yakar 2000, reproduced with permission) . . . . .	72
4.2	Premixed ethylene-air flame structure at combustor inlet conditions anticipated in a $M_\infty = 6$ scramjet . . . . .	74
4.3	Convected material element . . . . .	78
4.4	Product mass-fraction source term for various values of $\chi$ , for a WSR entraining burnt fluid (top), and unburnt fluid (bottom) . . . . .	82
4.5	Radical-pool concentration-evolution predictions using detailed chemical kinetics . . . . .	87
4.6	Ethylene ignition radical-pool growth (UCSD mechanism) . . . . .	89
4.7	Decrease in maximum residual with iteration number $k$ (solid black). The $k$ -value cutoff is selected when the residual decay approaches a smooth curve (dashed red). . . . .	91
4.8	Reciprocal ignition-delay surface . . . . .	93
4.9	Residuals as a function of temperature (left) and pressure (right) . . . . .	93
4.10	Overall reaction rate plotted against the combustion-evolution variable $\tau_c$ , conditional on $Z$ and $h$ , for $\tau_{c,en} \in [0, 1]$ . . . . .	99
4.11	Fuel mass-fraction plotted against the combustion-evolution variable, conditional on $Z$ and $h$ , for $\tau_{c,en} \in [0, 1]$ . . . . .	100
4.12	Table (left) in $[Z, h, \tau_c]$ -space tabulating $\zeta_c$ (right). . . . .	102

4.13	Definition of the overall reaction-evolution variable, $\tau$ , during the various stages of combustion. . . . .	104
5.1	LES-EVM interaction diagram . . . . .	109
5.2	Instantaneous OH mass fraction at the centerplane from an LES incorporating a flamelet model with compressibility corrections (Saghafian et al. 2015, Fig. 8, reproduced with permission), of the Gamba and Mungal (2015a) experiment (cf. Fig. 5.5) . . . . .	111
5.3	Hydrogen-air manifold discretization for the evolution-variable coordinate $\tau$ (top left), mixture fraction $Z$ (top right), internal energy $e$ (bottom left), and density $\rho$ (bottom right), in terms of the coordinate value plotted against the corresponding index. . . . .	113
5.4	Left: H <sub>2</sub> O mass-fraction slices as a function of $[Z, \rho, \tau]$ , with $e = 0$ J/kg. Right: H <sub>2</sub> O mass-fraction slices as a function of $[Z, e, \tau]$ , with $\rho = 0.5$ kg/m <sup>3</sup> . . . . .	114
5.5	OH-PLIF image of the crossplane in a reacting hydrogen-air TJISCF, from Gamba (2015a), Fig. 9, reproduced with permission. . . . .	115
5.6	Centerplane OH concentration from an EVM-LES simulation of the G15a experiment. Figure based on LES data courtesy of G. Candler. . . . .	115
5.7	Experimental OH-PLIF image (top, Gamba 2015a, Fig. 18, reproduced with permission) and simulated OH mass fraction (bottom, figure based on LES data courtesy of G. Candler.) on a plane parallel to the lower guidewall, at $y/d_j = 0.25$ . . . . .	116
5.8	Centerplane H <sub>2</sub> O mass fraction (top), and temperature (bottom) from the LES-EVM simulation of the G15a experiment. Figure based on LES data courtesy of G. Candler. . . . .	118
5.9	OH contours for simulations with grid resolution of 14 million elements, with fourth-order spatial accuracy (top), and 70 million elements, with second-order spatial accuracy (bottom). Figure based on LES data courtesy of G. Candler. . . . .	119
A.1	Representative $\mathbf{I}_{A,n}$ (top), $\bar{\mathbf{I}}$ (middle), and $\tilde{\mathbf{I}}_{A,n}$ (bottom) . . . . .	136

A.2	Average cross-correlation signal $\bar{C}$ at a location in the jet wake region produced with 32 image pairs. $x$ and $y$ axes have units of pixels, while the $z$ axis is the normalized cross-correlation coefficient, $R$ , that ranges from -1 to 1 . . . . .	137
A.3	Four randomly selected sample individual cross-correlation signals $C_n$ . $x$ and $y$ axes have units of pixels, while the $z$ axis is the normalized cross-correlation coefficient, $R$ , that ranges from -1 to 1 . . . . .	138
B.1	Chemiluminescence system calibration curve illustrating a quasi-linear response. The $x$ -axis is the normalized applied intensity, and the $y$ -axis is the normalized measured intensity. . . . .	143
C.1	Comparison of various potential ignition criteria . . . . .	145
C.2	Logarithmic variance between recent chemical-kinetics mechanisms and experimental ignition-delay data plotted as a function of initial mixture temperature. The thick black line represents the variance between the proposed EVM method and experimental data. 147	
C.3	Logarithmic variance between heritage chemical-kinetics mechanisms and experimental ignition-delay data plotted as a function of initial mixture temperature. The thick black line represents the variance between the proposed EVM method and experimental data. 148	
C.4	Mean variance between experimental ignition-delay data and ignition models including detailed chemical-kinetic simulations and the proposed EVM model . . . . .	149

# List of Tables

2.1	Injector-block specifications . . . . .	27
2.2	Reacting-gas composition . . . . .	39
3.1	Jet-fluid molar-mass effects . . . . .	44
3.2	Jet-diameter effects . . . . .	52
3.3	Chemical-timescale effects . . . . .	59
3.4	Jet-inclination effects . . . . .	60
4.1	Turbulence-chemistry scaling in an ethylene-fueled $M_\infty = 6$ scramjet . . . . .	76
4.2	Detailed chemical-kinetic mechanisms . . . . .	85
4.3	Experimental (shock-tube) ethylene ignition-delay data sets . . . . .	86
4.4	Fit coefficients . . . . .	92
4.5	Mixture fraction, $Z$ , example . . . . .	96
5.1	Gamba (2015a) experimental conditions . . . . .	112
B.1	Hydrogen-fluorine chemical-kinetic mechanism . . . . .	142

D.1	Run parameters . . . . .	150
-----	--------------------------	-----

# Contents

<b>Acknowledgements</b>	<b>v</b>
<b>Abstract</b>	<b>vi</b>
<b>1 Background and introduction</b>	<b>18</b>
1.1 Reacting jet in supersonic crossflow . . . . .	20
1.2 Thesis objectives . . . . .	23
<b>2 Experimental setup and diagnostics</b>	<b>24</b>
2.1 Facility overview . . . . .	24
2.2 Diagnostics and data processing . . . . .	27
2.2.1 Schlieren image-correlation velocimetry (SICV) system . . . . .	28
2.2.1.1 Comparison with artificial shadowgraph SICV . . . . .	32
2.2.2 Nitrosyl fluoride (NOF) and nitroxyl (HNO) chemiluminescence system . . . . .	35
<b>3 Experimental results</b>	<b>42</b>
3.1 Jet-fluid molar mass effects . . . . .	42

3.2	Jet-diameter effects . . . . .	50
3.3	Sensitivity to mixing-delay length criteria . . . . .	56
3.4	Chemical timescale effects . . . . .	57
3.5	Jet-inclination effects . . . . .	59
3.6	Control-volume analysis . . . . .	63
3.7	Conclusions . . . . .	68
<b>4</b>	<b>The evolution variable manifold (EVM) framework</b>	<b>70</b>
4.1	Background and introduction . . . . .	70
4.2	Small-scale structure of supersonic combustion . . . . .	71
4.2.1	Autoignition-dominated distributed reaction zone (DRZ) combustion . . . . .	73
4.2.2	Unit model for DRZ combustion . . . . .	77
4.2.3	The effects of $\chi$ . . . . .	81
4.3	Induction modeling in autoignition-dominated flows . . . . .	83
4.3.1	Chemical-kinetic mechanisms for induction modeling . . . . .	84
4.3.2	Induction evolution based on characteristic ignition-delay time . . . . .	86
4.3.3	Induction-evolution modeling based on shock-tube data . . . . .	89
4.4	Post-ignition manifold . . . . .	94
4.4.1	Manifold-construction process . . . . .	100
4.4.2	Combined data-driven induction model and post-ignition manifold . . . . .	104
<b>5</b>	<b>Application of EVM to large-eddy simulations</b>	<b>106</b>

5.1	LES-EVM overview . . . . .	107
5.2	LES-EVM implementation for a reacting hydrogen jet in supersonic crossflow . . . . .	110
5.2.1	Manifold construction . . . . .	111
5.2.2	Results . . . . .	114
<b>6</b>	<b>Conclusions</b>	<b>120</b>
	<b>Bibliography</b>	<b>122</b>
	<b>Appendices</b>	<b>134</b>
<b>A</b>	<b>Schlieren image-correlation velocimetry (SICV)</b>	<b>135</b>
<b>B</b>	<b>Nitrosyl fluoride (NOF) and nitroxyl (HNO) chemiluminescence</b>	<b>140</b>
<b>C</b>	<b>Detailed chemical kinetics assessment</b>	<b>144</b>
<b>D</b>	<b>Experimental conditions</b>	<b>150</b>

# Nomenclature

## Roman alphabet

<b>A</b>	Cross-correlation tile	
<i>A</i>	Jet-trajectory fit coefficient	
$A_f$	Stoichiometric coefficient	
<i>a</i>	Temperature power-law fit parameter	
$A_{TS}$	Test-section cross-sectional area	[m <sup>2</sup> ]
<b>B</b>	Cross-correlation template	
<i>B</i>	Jet-trajectory fit coefficient	
$B_f$	Virtual mixing origin	
<i>b</i>	Pressure power-law fit parameter	
$B_l$	Mixing-length expression fit parameter	
<b>C</b>	Cross-correlation signal	
$\overline{C}$	Average cross-correlation signal	
<i>c</i>	Ethylene mass fraction power-law fit parameter	
$c_m$	Mixing-length expression fit parameter	
<i>C</i>	Progress variable	
$C_\delta$	Shear-layer growth rate coefficient	
<i>d</i>	Oxygen mass fraction power-law fit parameter	
$d^*$	Jet-source diameter	[m]
$d_j$	Jet diameter	[m]
$Da$	Damköhler number	
<i>e</i>	Specific internal energy	[J/kg]
<i>h</i>	Specific enthalpy	[J/kg]

$h\nu$	Photon energy	
$\hat{\mathbf{I}}$	Mean intensity	
$I$	Intensity	
$\tilde{\mathbf{I}}$	Mean intensity difference	
$J$	Jet-to-crossflow momentum-flux ratio	
$k$	Iteration number	
$ke$	Kinetic energy	[J/kg]
$k_n$	Rate constant	
$ke'_R$	Reactor-scale kinetic-energy	[J/kg]
$Ka_R$	Karlovitz number based on the reaction-zone thickness	
$L_f$	Flame length	[m]
$l_{m,char}$	Characteristic mixing-delay length	[m]
$l_m$	Mixing-delay length	[m]
$l_{tr,SL}$	Shear-layer laminar-to-turbulent mixing transition location	[m]
$l_0$	Integral turbulence length scale	[m]
$\dot{m}$	Mass flux	[kg/s]
$\dot{m}_{en}$	Mass flux entrained into the reactor	[kg/s]
$\dot{m}_j$	Jet-exit mass flux	[kg/s]
$\dot{m}_{out}$	Mass flux out of the reactor	[kg/s]
$M$	Mach number	
$M_\infty$	Crossflow Mach number	
$M_j$	Jet-exit Mach number	
$m_R$	Reactor mass	[kg]
$N_i$	Number of shock-tube experiments	
$N_\alpha$	Number of species	
$p$	Pressure	[Pa]
$p_{0,\infty}$	Crossflow stagnation pressure	[Pa]
$p_{0,j}$	Jet-plenum stagnation pressure	[Pa]
$P_j$	Jet-exit momentum flux	[kg·m/s <sup>2</sup> ]
$R$	Normalized cross-correlation coefficient	
$r$	Residual	
$r_{SL}$	Shear layer low to high-speed stream velocity ratio	

$r_{\log}$	Logarithmic variance	
$R_s$	Gas constant	[J/(kg·K)]
$Re$	Reynolds number	
$Re'$	Turbulence Reynolds number	
$Re_\delta$	Reynolds number based on shear-layer thickness	
$Re'_b$	Burnt-fluid turbulence Reynolds number	
$Re_j$	Reynolds number based on jet-orifice diameter	
$Re'_u$	Unburnt-fluid turbulence Reynolds number	
$s$	Shear layer low to high-speed stream density ratio	
$Sa$	Stream-thrust function	[N·s/kg]
$T$	Temperature	[K]
$T_f$	Adiabatic flame temperature	[K]
$T_{\text{amb}}$	Ambient temperature	[K]
$t_{\text{chem}}$	Chemical timescale	[s]
$t_{d,c}$	Characteristic ignition-delay time	[s]
$t_d$	Ignition-delay time	[s]
$t_{\text{flow}}$	Flow timescale	[s]
$t_{\text{LED}}$	Schlieren light source pulse duration	[s]
$\Delta t_{\text{IF}}$	Schlieren camera interframe time	[s]
$\mathbf{u}$	Velocity vector	[m/s]
$\bar{\mathbf{u}}$	Bulk-fluid velocity	[m/s]
$\mathbf{u}'_R$	Reactor-scale velocity fluctuations	[m/s]
$u'$	Fluctuating (rms) component of velocity	[m/s]
$u, v, w$	Velocity vector components	[m/s]
$U_\infty$	Freestream velocity	[m/s]
$U_{c,\text{SL}}$	Shear-layer convective velocity	[m/s]
$U_c$	Convective velocity	[m/s]
$U_j$	Jet-exit velocity	[m/s]
$u'_R$	Reactor-scale velocity fluctuation magnitude	[m/s]
$\mathbf{v}_\alpha$	$\alpha$ -species diffusion velocity	[m/s]
$\mathbf{v}_Z$	Mass fraction, $Z$ , diffusion velocity	[m/s]
$\mathbf{v}_C$	Progress variable, $C$ , diffusion velocity	[m/s]

$V$	Volume	[m <sup>3</sup> ]
$V_R$	Reactor volume	[m <sup>3</sup> ]
$\partial V_R$	Reactor area	[m <sup>2</sup> ]
$W_\infty$	Crossflow-fluid molar mass	[g/mol]
$W_j$	Jet-fluid molar mass	[g/mol]
$\mathbf{x}$	Position vector	[m]
$X$	Mole fraction	
$X_{j,dil}$	Jet-fluid diluent mole fractions	
$Y$	Mass fraction	
$Y_\alpha$	$\alpha$ -species mass fraction	
$Y_{P,eq}$	Equilibrium product mass fraction	
$Y_P$	Product mass fraction	
$Y_{rad,d}$	Radical mass fraction at ignition	
$Y_{rad}$	Radical mass fraction	
$\hat{Y}_{rad}$	Normalized radical mass fraction	
$\mathcal{Y}$	Elemental (atomic) mass fraction	

### Greek alphabet

$\beta$	Exponential activation-energy fit parameter	
$\gamma$	Heat-capacity ratio	
$\chi$	Small-scale entrainment	[1/s]
$\delta_R$	Reaction-zone thickness	[m]
$\Delta_R$	Reactor length scale	[m]
$\delta_{SL}/x$	Shear-layer growth rate	
$\dot{\omega}_\alpha$	$\alpha$ -species production rate	[kg/(m <sup>3</sup> ·s)]
$\dot{\omega}_{Y_\alpha}$	$\alpha$ -species mass-fraction production rate	[1/s]
$\dot{\omega}_{Y_P}$	Product mass-fraction production rate	[1/s]
$\dot{\omega}_C$	Progress-variable source term	[1/s]
$\epsilon$	Combustion-product mass-fraction premixed in reactor	
$\eta$	Exponential pressure-dependence fit parameter	
$\kappa$	Induction-evolution variable value at ignition	

$\lambda$	Wavelength	[nm]
$\lambda_K$	Kolmogorov length scale	[m]
$\Theta$	Thermodynamic state $[h, p]$ or $[e, \rho]$	
$\mu$	Shear/dynamic (molecular) viscosity	[Pa·s]
$\nu$	Kinematic viscosity	[m <sup>2</sup> /s]
$\phi$	Stoichiometry	
$\pi$	Normalized pressure ( $p/1$ bar)	
$\rho$	Density	[kg/m <sup>3</sup> ]
$\rho_\infty$	Crossflow density	[kg/m <sup>3</sup> ]
$\rho_j$	Jet-fluid density	[kg/m <sup>3</sup> ]
$\sigma$	Standard deviation	
$\tau$	Overall reaction-evolution variable	
$\tau_{i,0}$	Background induction-evolution variable	
$\tau_i$	Induction-evolution variable	
$\tau_c$	Combustion-evolution variable	
$\theta$	Normalized temperature ( $T/1000$ K)	
$\theta_c$	Critical jet-injection angle	[deg]
$\theta_{\text{div}}$	Test-section sidewall divergence angle	[deg]
$\theta_j$	Jet-inclination angle	[deg]
$\varpi$	Crossflow-to-jet molar mass ratio	
$\zeta$	Overall reaction-evolution rate	[1/s]
$\zeta_i$	Induction-evolution rate	[1/s]
$\zeta_0$	Pre-exponential fit parameter in characteristic ignition-delay time expression	[1/s]
$\zeta_c$	Combustion-evolution rate	[1/s]

### Frequently used subscripts

$()_1$	Upstream of jet injection
$()_2$	Downstream of jet injection
$()_j$	Jet-fluid property
$()_\infty$	Crossflow-fluid property
$()_{\text{en}}$	Entrained-fluid property

- $()_{\text{eq}}$  Thermochemical-equilibrium fluid property
- $()_{\text{F}}$  Fuel-stream fluid property
- $()_{\text{Ox}}$  Oxidizer-stream fluid property

# Chapter 1

## Background and introduction

Recent proof-of-concept developments in ground and flight testing of air-breathing vehicles in the flight Mach 5-7 range have renewed interest in fundamental physical processes that contribute to combustion and energy release in supersonic flows. High-speed and supersonic combustion is characterized by intense turbulence, short residence times available for fuel-air dispersion, mixing, and reaction, and, at low flight Mach numbers, only moderate pre-ignition temperatures to promote autoignition. Improved understanding of relevant physical processes would help develop predictive engineering models for the spatial and temporal distribution of heat-release in supersonic and high-subsonic combustors.

Experimental investigation of supersonic reacting flows in ground-based facilities is challenging. The main difficulties lie in generating sufficiently-high total enthalpy to obtain freestream static temperatures above hydrogen or hydrocarbon autoignition temperatures (if such fuels are used), and in obtaining experimental data from such flows. Available supersonic or high Mach number subsonic reacting flow data are typically obtained using impulse facilities, such as shock or expansion tubes (e.g., Rothstein 1992, Heltsley et al. 2007, Ben-Yakar 2000, Ben-Yakar et al. 2006, Gamba and Mungal 2015a), or vitiated-air blow-down facilities (e.g., Mathur et al. 2001, Micka and Driscoll 2012). Alternately, hypergolic reactants that ignite and react on contact at lower enthalpy corresponding to ambient conditions can be used in a blow-down facility (Hall 1991, Slessor 1998, Bond 2000, and others). There are challenges associated with hypergolic fuels, however, related to their extreme reactivity.

Measurements in supersonic reacting flows typically include wall pressure, stagnation temperature using thermocouples, and increasingly, optical measurements. Optical flow measurements include high-speed schlieren imaging (e.g., Ben-Yakar 2000), chemiluminescence (e.g., Nakaya et al. 2015b), OH planar laser fluorescence (OH-PLIF) (Lee et al. 1991, Rothstein 1992, Ben-Yakar 2000, and others), and, more recently, CH or formaldehyde PLIF (e.g., Micka and Driscoll 2012). Due to the complexity and effort involved in generating ground-based supersonic reacting flows and obtaining data from such flows, however, only a few parametric studies exist that use multiple experiments to isolate and focus on the effects of individual flow parameters.

Simulating supersonic combustion has its own challenges. Resolving all scales anticipated in the turbulence environment of supersonic combustors through direct numerical simulation (DNS) is not currently feasible, nor anticipated in the foreseeable future. Reynolds-averaged Navier-Stokes (RANS) or large-eddy simulations (LES, Sabelnikov et al. 1998, Berglund et al. 2010, Saghafian et al. 2015, and others) are less computationally expensive, and are currently the ‘go-to’ methods for simulating supersonic combustion. Even in such reduced-order methods, however, it is computationally prohibitively expensive to transport all reaction intermediate species that contribute to detailed chemical-kinetic modeling of complex hydrocarbon combustion in supersonic flows. As a result, reduced chemical kinetic mechanisms are derived from detailed mechanisms and used in RANS and LES simulations. Decreasing the resolution, or number of species and reactions, of a detailed chemical-kinetic mechanism can affect the accuracy of the resulting reduced mechanism.

An alternative approach is to model the small-scale structure of the reacting flow using an appropriate unit model with detailed chemical kinetics, and tabulate the detailed state of the fluid as a function of a reduced number of variables (typically 5 or less) that are then transported in the flow. An example of this approach is the flamelet-generated manifold approach that has been used extensively in low Mach number combustion simulations. The flamelet model has also been applied to supersonic combustion, under the assumption that supersonic combustion can be approximated as a collection of flamelets, at the smallest scales (e.g. Terrapon et al. 2009, Saghafian et al. 2015).

In supersonic combustors, flow timescales, defined by the time-of-flight of a convected, reacting material element, and chemical-induction timescales, defined by the time required for mixed fluid to ignite, are often of the same order of magnitude. This places considerable importance on reliable modeling of induction processes that precede autoignition. Detailed chemical-kinetic mechanisms are

reliable at intermediate or high temperatures and near-stoichiometric conditions, but less so at low temperatures and off-stoichiometric conditions. In simulating flows where autoignition is important, large uncertainties in induction modeling propagate to the overall reacting flowfield, compromising the overall predictive capability of the model.

Typical flow configurations used in supersonic combustion research, both numerically and experimentally, are the planar shear layer and, increasingly, the transverse jet in supersonic crossflow. These canonical flows can also form the building blocks for practical fuel-injection strategies. Experiments and simulations reported in this thesis investigate the transverse jet in supersonic crossflow (TJISCF).

## 1.1 Reacting jet in supersonic crossflow

The transverse jet in supersonic crossflow is a canonical flow, rich in complex physics and of practical relevance to scramjet fuel injection.

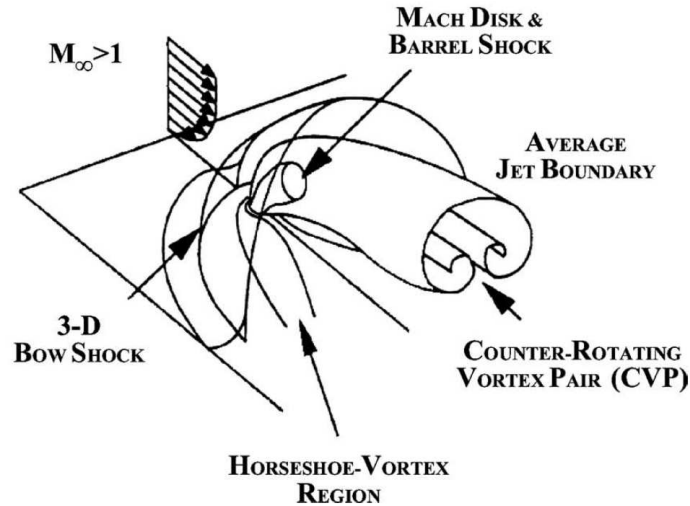


Figure 1.1: Three-dimensional schematic of a transverse jet in supersonic crossflow (TJISCF), from Gruber et al. (1995)

It is highly three-dimensional, with several distinct flow features. These include sheared regions near the jet orifice, a counter-rotating vortex pair in the jet wake region, recirculation zones upstream and downstream of the jet (in the case of normal injection), and the characteristic barrel and detached three-dimensional bow-shock structures, as shown in Fig. 1.1 (Gruber et al. 1995).

In a scramjet combustor, the TJISCF can provide a means of accessing a larger fraction of the oxygen in the freestream than non-penetrating flow configurations, such as a planar shear layer, while generating intense turbulence that enables efficient molecular mixing of freestream and jet fluid. The downside, of course, is the higher cost in terms of total-pressure losses. If the jet and crossflow fluids are compatible reactants at suitable conditions, chemical reactions occur within the molecularly mixed regions that lead to autoignition, strong combustion, and heat release.

The trajectory and penetration of a normal TJISCF depend primarily on the jet-orifice diameter  $d_j$  and the momentum-flux ratio,

$$J = \frac{\rho_j U_j^2}{\rho_\infty U_\infty^2}, \quad (1.1)$$

where  $U$  and  $\rho$  are velocity and density, and subscripts  $j$  and  $\infty$  denote the jet and crossflow, respectively. The jet trajectory is typically expressed as

$$\frac{y}{Jd_j} = f(x, d_j, J), \quad (1.2)$$

where  $x$  is the streamwise coordinate. The function  $f(x, d_j, J)$  can take a logarithmic form, or, more commonly, a power-law of the form,

$$\frac{y}{Jd_j} = A \left( \frac{x}{Jd_j} \right)^B, \quad (1.3)$$

where  $B$  is empirically found to be close to 0.3. Mahesh (2013) provides an overview of relevant jet in supersonic crossflow trajectory and penetration expressions. The momentum-flux ratio  $J$  also determines whether the jet is in the strong ( $J \gg 1$ ) or weak ( $J \sim 1$ ) regime. The trajectory of a strong jet is determined by the streamwise momentum of the entrained crossflow fluid while that of a weak jet is dominated by pressure effects (e.g., Hasselbrink and Mungal 2001). Andreopoulos and

Rodi (1984) performed weak transverse jet-in-crossflow experiments ( $0.5 \leq J \leq 2$ ) in incompressible flow with uniform-density fluids, reporting a recirculation zone upstream of the jet, and the effects of  $J$  on measured turbulence intensity in the jet-in-crossflow. Haven and Kurosaka (1997) performed weak transverse jet-in-crossflow experiments with several jet-orifice shapes, and found that near-field parameters (jet-orifice geometry) affects far-field flow characteristics including jet penetration and vorticity. Available literature contains considerable experimental TJISCF trajectory and penetration data (Schetz and Billig 1966, Rogers 1971, McDaniel and Raves 1988, Rothstein 1992, and others), as well as limited jet-fluid entrainment and mixing (Ben-Yakar et al. 2006, Gruber et al. 1997a, Lin et al. 2010, VanLerberghe et al. 2000, and others), and velocity and turbulence intensity (Santiago and Dutton 1997) data, mainly for non-reacting TJICF systems. Available reacting TJISCF data, however, are limited.

Reacting-jet experiments in supersonic crossflow with oxygen and hydrogen or hydrocarbon reactions are particularly difficult to perform, as discussed above. Notable reacting-jet in supersonic, or high-speed crossflow experiments include those by Lee et al. (1991), Rothstein (1992), Ben-Yakar et al. (2006), Micka and Driscoll (2012), and Gamba and Mungal (2015a). Lee as well as Rothstein independently demonstrated the viability of OH-PLIF for investigating hydrogen-air TJISCF combustion. Ben Yakar investigated reacting ethylene and hydrogen jets in crossflow using OH-PLIF, combined with fast-framed schlieren in an expansion tube, with emphasis on the differences between the two fuels, as will be discussed. Gamba also investigated reacting hydrogen jets in crossflow using OH-PLIF and chemiluminescence, focusing on jet-to-crossflow momentum-flux ratio ( $J$ ) effects on the near-wall and far-field reaction-zone structure. Micka used CH, OH and formaldehyde PLIF, and CH\* chemiluminescence to investigate the flame structure of a sonic jet in high Mach number subsonic ( $M_\infty = 0.62$ ) vitiated air crossflow. He identified the importance of the ignition-delay length in a reacting jet in crossflow, as well as the ‘distributed reaction zone’ (DRZ) nature of such reacting flows in that regime.

The TJISCF experiments described in this thesis were performed with hypergolic reactants. This choice allowed access to a wide, well-controlled parameter space. While such hypergolic reactants would not be used as practical fuels for high-speed propulsion, reactant concentrations in this set of experiments are tailored so that the fundamental physical processes are similar to those anticipated in scramjet combustors, i.e., flow and combustion timescales are comparable. The primary difference is that heat release is negligible in these experiments. The results add to and complement the existing

body of reacting TJISCF data. They reveal new insights on the effects of jet molar mass, jet diameter, and jet inclination on the structure of the reaction zone, and, in particular, on mixing-delay length.

## 1.2 Thesis objectives

This thesis focuses on two main subtopics and objectives.

1. **Experimentally investigate aspects of entrainment, molecular mixing, and chemical reactions in supersonic reacting flow (Chapters 2 and 3).**

Reacting transverse jet in supersonic crossflow (TJISCF) experiments using hypergolic reactants were conducted to investigate entrainment and molecular-mixing processes in supersonic reacting flows. In the course of the investigations, new results were obtained and are reported on the effects of jet molar mass, orifice diameter, and jet inclination on the reacting flowfield.

2. **Develop and implement a combustion-modeling framework for large-eddy simulations of supersonic reacting flow with complex chemistry (Chapters 4 and 5).**

A proposed ignition-delay data-driven approach to induction modeling is combined with a tabulated chemistry (manifold) approach for post ignition, based on a Lagrangian unsteady well-stirred reactor (WSR, or balloon reactor) unit model. The resulting methodology is used in a large-eddy simulation of a hydrogen jet in heated air supersonic crossflow experiment.

## Chapter 2

# Experimental setup and diagnostics

### 2.1 Facility overview

Experimental results presented in this thesis were obtained from experiments performed at the GALCIT supersonic shear-layer laboratory (S<sup>3</sup>L) facility. The shear-layer facility originally operated as a subsonic facility for about a decade (Mungal 1983, Mungal and Dimotakis 1984) before its upgrade to its supersonic S<sup>3</sup>L configuration in 1991, and has since undergone several upgrades to the gas-handling system, diagnostics, and infrastructure (Hall 1991, Slessor 1998, Bond 2000, Bergthorson et al. 2009, Bonanos et al. 2009), expanding fundamental understanding of molecular mixing and combustion in high-speed and supersonic flows. The centerpiece of the lab in its present configuration is a blowdown wind tunnel capable of a mass flux up to 10 kg/s and freestream Mach numbers of up to 3.2 in both chemically reacting and non-reacting configurations. The wind tunnel has an optically accessible test section (cross-sectional area  $A_{TS} \approx 5.2 \times 10^{-3} \text{ m}^2$ , see Fig. 2.2) and is capable of test times of 4 seconds, or so. A brief overview of the facility is provided. Additional details can be found in Hall (1991), Bond (2000), Bergthorson et al. (2009), and Bonanos et al. (2009).

A schematic of the gas-delivery system is shown in Fig. 2.1.<sup>1</sup> For the experiments described here, the top-stream reactant tank ( $V = 1.2 \text{ m}^3$ ) supplies diluted hydrogen ( $\text{H}_2$ ) premixed with nitric oxide (NO) through a modular converging-diverging nozzle section to produce supersonic crossflow (Mach

---

<sup>1</sup>The gas delivery system was evolved to its present state over several years by G. Mungal, J. Hall, C. Bond, M. Slessor, J. Bergthorson, A. Bonanos, D. Lang, and P. Dimotakis.

number  $M_\infty = 1.5$  in the current configuration), while the bottom-stream reactant tank ( $V = 0.57 \text{ m}^3$ ) supplies diluted-fluorine ( $\text{F}_2$ ) jet fluid to the jet-fluid plenum. The jet fluid is held in a Teflon bladder bag within the  $\text{F}_2$  reactant tank. This keeps the reactant-tank pressure almost constant for the duration of the run, by equalizing the pressure exterior of the bag with the pressure in a much-larger surge tank ( $V = 12 \text{ m}^3$ ). Flow rates are controlled by an active, computer-controlled metering valve on the hydrogen (crossflow) side, and a passive micrometer valve on the fluorine (jet-fluid) side. Crossflow mass-flow rates are on the order of  $5 \text{ kg/s}$  for the experiments discussed here. The jet-fluid stream is typically initiated a few seconds before the supersonic crossflow starts, to displace the purge gas in the lower plenum with pure jet-fluid before measurements are recorded.

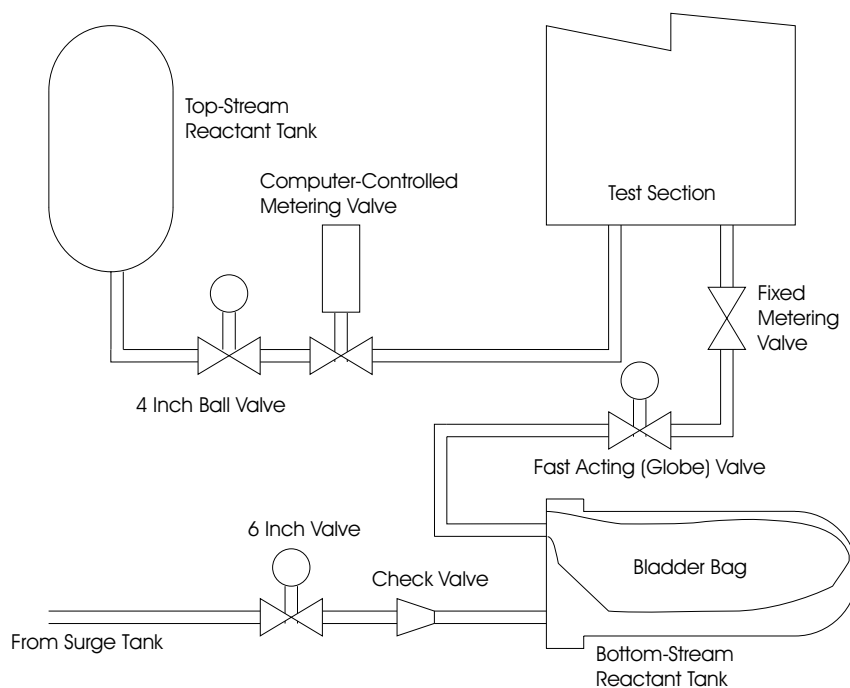


Figure 2.1: Gas-delivery system diagram (Bond 1991, Fig. A.1)

The optically accessible portion of the test section is shown in Fig. 2.2.<sup>2</sup> For the experiments described here, the upper guidewall diverges slightly ( $\theta_{\text{div}} = 1.05^\circ$ , with a spline transition over a 1.5 in. (38 mm) interval centered around point (D) in Fig. 2.2) to offset boundary-layer growth and

<sup>2</sup>Conception, design and manufacturing of the present jet-in-crossflow configuration, and test section modifications, performed by L. Maddalena and P. Dimotakis.

avoid imposed streamwise pressure gradients. The distance between the upper and lower guidewalls in the parallel region upstream of the flexure hinge is 1.26 in. (32 mm). A  $30^\circ$  expansion ramp follows the quasi-uniform area section and accelerates the flow, isolating the upstream flow from downstream boundary conditions and blockage effects, while providing a recirculation region to promote additional mixing and reaction before exhaust.

The jet orifice is located upstream of the ramp by either 3.75 in. (95 mm, RN1 injector, see Table 2.1) or 3.44 in. (87 mm, RN2, RI1), depending on the injector block, and is fed from the lower plenum. The width of the test section is 6 in. (152 mm) throughout. The sidewalls of the optically accessible portion of the test section are 2 in. (51 mm) thick BK7 glass, lined with replaceable 0.125 in. (3.2 mm) thick Pyrex sheets on both interior sides. Hydrogen fluoride (HF) in the reaction products etches the sidewall glass, eventually affecting schlieren and chemiluminescence image quality. This is mitigated by periodic replacement of the sacrificial HF-exposed Pyrex sheets.

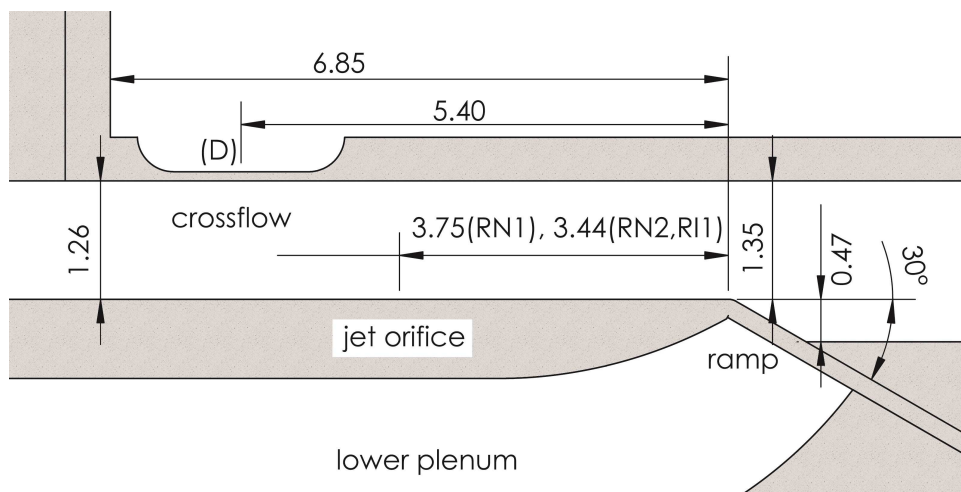


Figure 2.2: Test-section dimensions, in inches

Jet orifices are machined into modular, interchangeable injector blocks.<sup>3</sup> Injector blocks in the present experiments include two round, normal (RN) transverse jets, and a round inclined (RI) jet, which are listed in Table 2.1, and whose geometry is shown in Fig. 2.3. The RI1 injector has a nacelle-like inlet to minimize vorticity imparted on the inclined jet. An inclined jet injector with

<sup>3</sup>Conception, design, and manufacturing of the interchangeable injector-block configuration was performed by P. Mehrotra, L. Maddalena, B. Valiferdowski, and P. Dimotakis.

a flush inlet would generate a counter-rotating vortex pair in the jet orifice, by a similar vorticity-generation mechanism that produces a counter-rotating vortex pair in a jet-in-crossflow wake. The plate thickness for all injector orifices is  $3/8$  inches (9.5 mm).

Table 2.1: Injector-block specifications

Name	diameter ( $d_j$ ), in. (mm)	inclination (deg.)	inlet style
RN1	0.20 (5.08)	$90^\circ$	flush
RN2	0.25 (6.35)	$90^\circ$	nacelle
RI1	0.25 (6.35)	$30^\circ$	nacelle

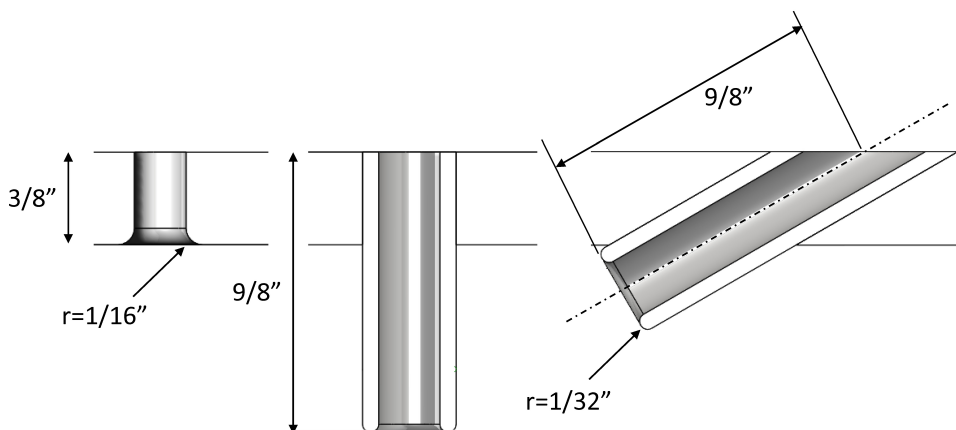


Figure 2.3: RN1 ( $d_j = 0.20$  in., left), RN2 ( $d_j = 0.25$  in., center), and RI1 ( $d_j = 0.25$  in., right) injector-orifice geometry

## 2.2 Diagnostics and data processing

A fast-framing, high-resolution schlieren/shadowgraphy system captures time-correlated image pairs for convective-velocity measurements using a schlieren image-correlation velocimetry (SICV) technique with novel image-processing. Simultaneously, an intensified time-averaged chemiluminescence measurement system images the large-scale reaction-zone structure of the transverse jet in supersonic

crossflow (TJISCF) and helps determine mixing-delay lengths.<sup>4</sup>

## 2.2.1 Schlieren image-correlation velocimetry (SICV) system

Turbulent structures marked by refractive-index gradients at their interfaces are generated as jet fluid entrains, disperses, and mixes with crossflow fluid. These structures move at the convective velocity of the local flow, an important quantity that relates the convected frame in which molecular mixing and reactions take place (e.g., Dimotakis 1991) to the lab frame. These structures can be imaged by schlieren or shadowgraphy techniques, reviewed in Settles (2001). The convective velocity of these interfaces can be determined from sequences of (two or more) time-correlated images. Ben-Yakar et al. (2006) [BY06] successfully used sequences of eight schlieren images to track the instantaneous convection velocity of individual, manually-identified eddies at the leading edge of the TJISCF. Using a similar approach, Gruber et al. (1997b) used particle-seeded jet fluid and a laser sheet to capture time-correlated pairs of images, from which the instantaneous eddy convection velocity was estimated by manually estimating eddy displacement.

A more-general schlieren-based velocimetry approach was used by Jonassen et al. (2006) that combined focused-schlieren images with commercial PIV software to estimate the convective velocity in simple test flows including a boundary layer and an axisymmetric jet. This technique demonstrated the potential of schlieren-based velocimetry methods, but would have limitations in complex, inherently unsteady flows such as jets in supersonic crossflow of interest here.

A schlieren image correlation velocimetry (SICV) method is developed and used to extract time-averaged convective velocity from sets of time-correlated schlieren image pairs using a frame-averaged cross-correlation algorithm. SICV shares elements with the approach proposed by Meinhart et al. (2000) for applications in microfluidics that extracts time-averaged velocity from multiple sparse, intermittent, PIV image pairs using a frame-averaged cross-correlation algorithm. The SICV approach has advantages over existing methods for estimating convective velocity in high-speed flows. It lacks the bias that could be introduced by manual structure-displacement measurements, or manual structure identification. Additionally, convective velocity field estimates are possible with sufficiently high quality schlieren images (cf. Fig. 2.6). The SICV method is described in detail in Appendix A.

---

<sup>4</sup>The design, manufacturing, and assembly of the fast-framing schlieren and intensified chemiluminescence system was performed by N. Cymbalist, D. Lang, P. Mehrotra, and P. Dimotakis.

A high-speed camera captures time-correlated, high-resolution schlieren/shadowgraph image pairs using a folded-Z schlieren/shadowgraph system with a pulsed LED light source. The folded-Z schlieren system is built around a pair of 10-inch spherical mirrors (SM1 and SM2 in Fig. 2.4) as detailed in Hermanson (1985), and uses high-quality 85mm,  $f/1.4$ , lenses (SL1 and SL2) at full aperture to form the image on the camera sensor. Figure 2.4 shows a diagram of the schlieren system. The chemiluminescence sensing system uses the schlieren system optics in reverse, as illustrated in the same figure, and is discussed in the following section.

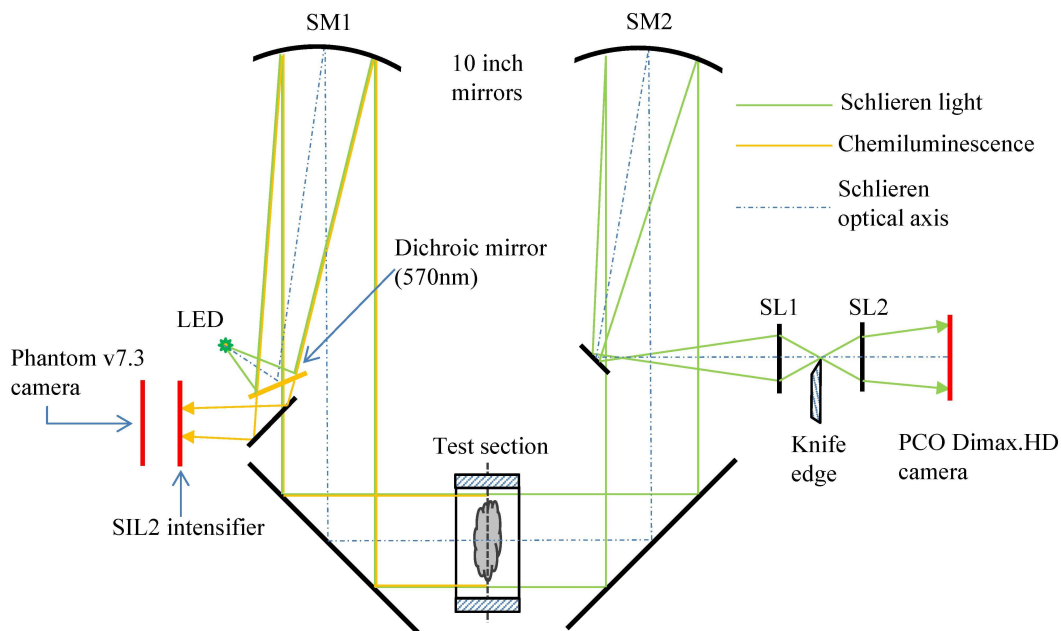


Figure 2.4: Optical system combining schlieren/shadowgraph (right-propagating light), and chemiluminescence (left-propagating light, diagram not to scale)

A PCO.Dimax HD camera was modified to support double-framing capable of  $\Delta t_{IF} = 5 \mu\text{s}$  interframe time, and either a white CREE XM-L (for non-reacting runs), or a green Luminus SBT-70 (for reacting runs) LED with a custom driver<sup>5</sup> were pulsed on each side of the interframe (pulse duration,  $0.5 \mu\text{s} < t_{LED} < 1.0 \mu\text{s}$ ) to generate the image pair. White light produces better images, but interferes with the intensified chemiluminescence system that is also active during a reacting run. The system is capable of capturing up to 1500 image-pairs per second at HD-level resolution

<sup>5</sup>The LED and high-speed camera timing system was designed, developed, and built by D. Lang.

( $1920 \times 1080$  pixels). Fig. 2.5 shows a sample image-pair (A+B) of a non-reacting helium jet in a nitrogen crossflow (Run ss1694), captured using a white LED pulsed at  $t_{LED} = 0.6 \mu s$ .

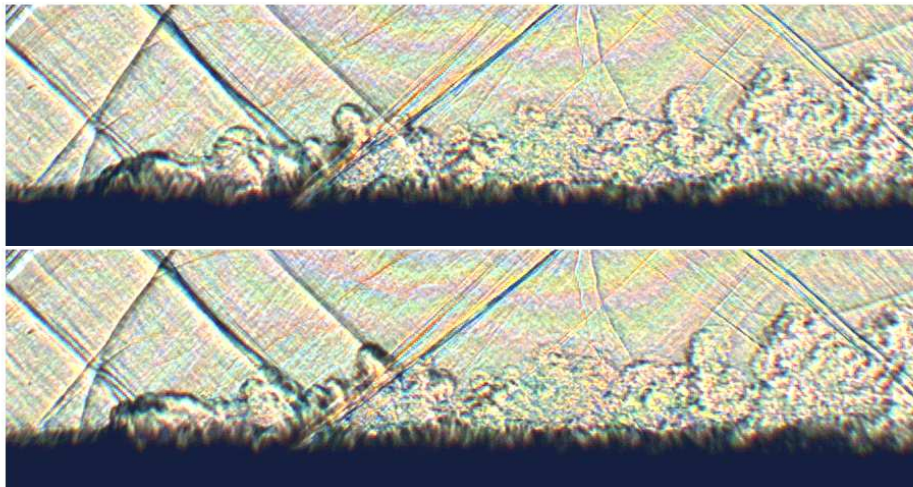


Figure 2.5: Image A (top), and image B (bottom),  $\Delta t_{IF} = 6 \mu s$  (Run ss1694)

The displacement of refractive-index interfaces is clearly discernible. Small imperfections in the test guide-walls cause the oblique Mach waves that are present, starting upstream of the jet, that help accurate local flow Mach number estimation. For example, the freestream Mach number was estimated as  $M_\infty = 1.43 \pm 0.02$  based on the angle of the Mach waves upstream of the jet. Sets of image pairs are post-processed using a frame-averaged cross-correlation algorithm, explained in detail in Appendix A, to produce convective velocity estimates.

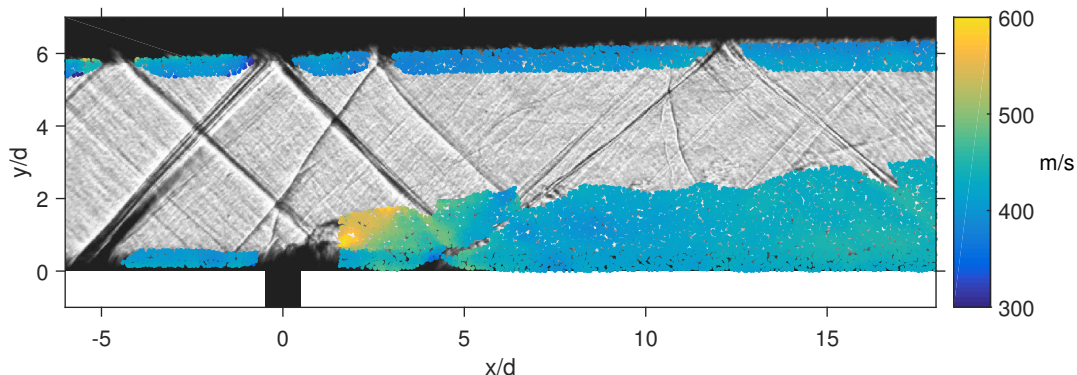


Figure 2.6: Streamwise velocity component of convected refractive-index interfaces of a helium jet in supersonic nitrogen crossflow (Run ss1694) overlaying a shadowgraphy image of the same flow

Figure 2.6 plots the time- and spanwise-averaged streamwise velocity of convected turbulent structures formed by a sonic helium jet in supersonic nitrogen crossflow (Run ss1694) obtained using SICV. The regions without a sufficiently strong contrast cannot be tracked and correspond to laminar regions outside the jet body and boundary layer. Velocity estimates very close to the jet-orifice ( $-0.5 < x/d < 1.5$  centered around the jet orifice axis) were deemed unreliable and ignored.

For the purpose of comparing measured convective velocity (estimated as the refractive-index interface velocity) against theory or simulations, average convective velocities at a given streamwise location are estimated, determined by binning all measurements in a given  $x/d$  range. These regions are shown in Fig. 2.7 (top) and the average convective velocity at intervals of  $x/d$  interval underneath. Variation in the velocity measurements in each interval bin are caused by measurement uncertainties, as well as by subregions within the bin that may have velocity variations. The standard deviation of the velocity measurements in each bin,  $\sigma$ , is plotted as uncertainty bars in Fig. 2.7.

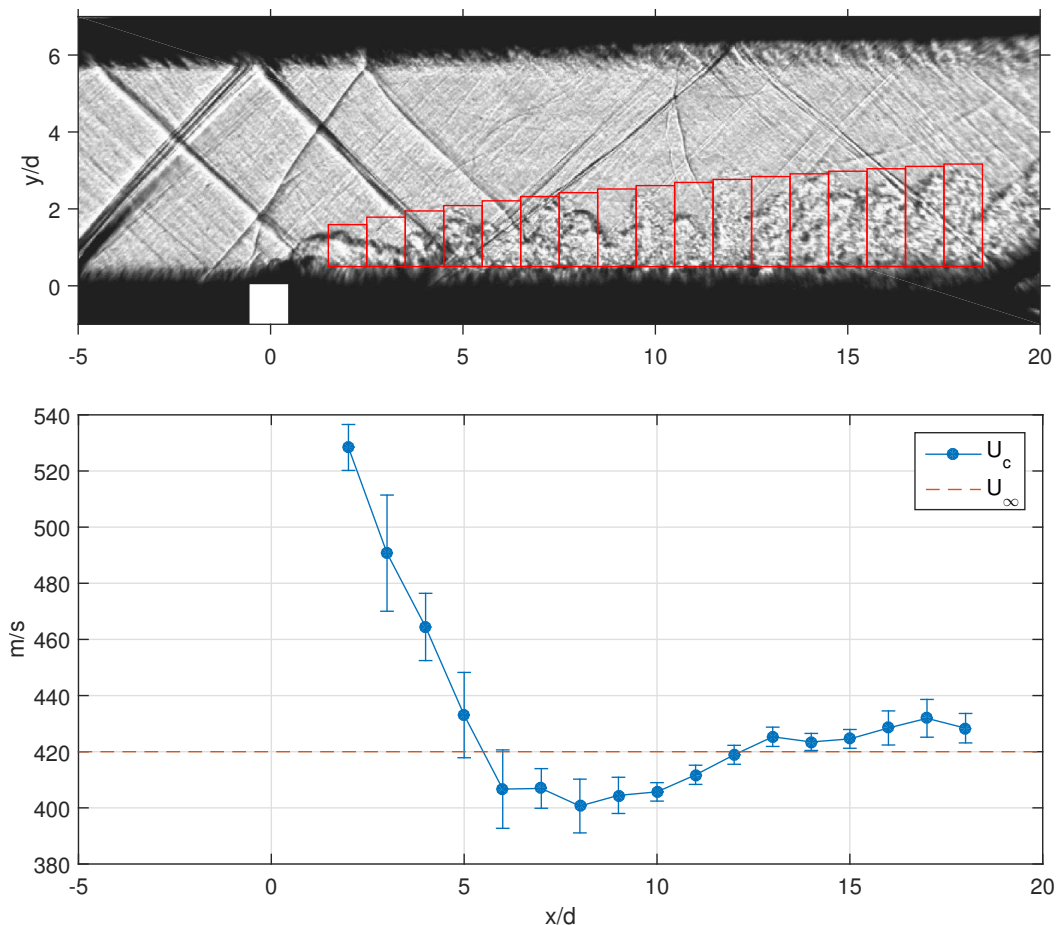


Figure 2.7: Binning structure (top) used to produce average convective-velocity estimates (bottom) of Run ss1694. Error bars mark the standard deviation ( $\pm\sigma$ ) of the measured convective velocity within the bin. The freestream velocity is estimated as  $U_\infty = 420$  m/s.

### 2.2.1.1 Comparison with artificial shadowgraph SICV

To determine what SICV measures, a set of 32 artificial shadowgraph image pairs were generated using simulated refractive-index fields extracted from large-eddy simulation (LES) data,<sup>6</sup> analyzed using the same SICV algorithm, and compared to conditional velocity data from the LES. The artificial schlieren and shadowgraph images were generated by ray tracing through an accurate

<sup>6</sup>The large-eddy simulations and numerical shadowgraphy images were generated by Dr. Elizabeth Luthman. She kindly provided both the image sets and velocity data from the simulations for this analysis. These will appear in Cymbalist, et al. (2016) and Luthman, et al. (2016)

model of the optical system used to obtain the experimental schlieren images, and a refractive-index field obtained from a LES simulation of Run ss1794. Further details are reported in Cymbalist et al. (2016, in preparation), and Luthman et al. (2016, in preparation). Figure 2.8 shows an example of such a simulated shadowgraphy image.

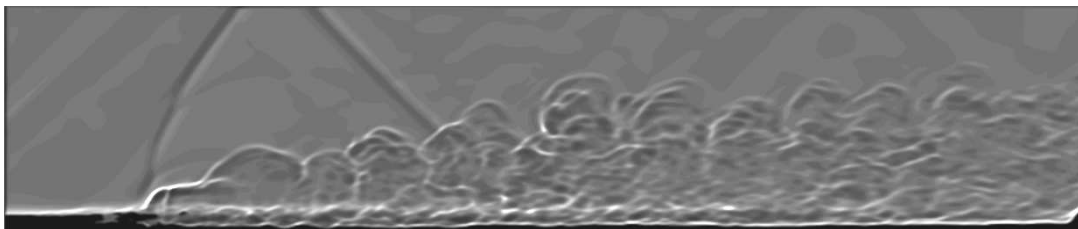


Figure 2.8: Simulated shadowgraphy image, courtesy of Dr. Elizabeth Luthman

SICV was performed on the artificial-schlieren image pairs to extract the convective velocity from the simulations. The convective velocity measured from the simulated schlieren image pairs was compared to flow velocity extracted from the simulations, conditioned by the jet-fluid mass fraction. It was found that the binned SICV measurements of convective velocity from the simulated-schlieren image pairs provide a good estimate for the spatially and 32-frame averaged velocity magnitude ( $|\mathbf{u}| = \sqrt{u^2 + v^2}$ ) of fluid with a (helium, in this case) jet-fluid mass fraction  $0.1 < Y_{\text{He}} < 0.9$ ,

$$U_{c,\text{SICV}} \simeq \langle \bar{\mathbf{u}}_{\text{LES}} \rangle_{0.1 < Y_{\text{He}} < 0.9} , \quad (2.1)$$

where  $\bar{\mathbf{u}}_{\text{LES}}$  is the averaged velocity from the LES (see below), and  $\langle \dots \rangle_{0.1 < Y_{\text{He}} < 0.9}$  denotes a conditional average over fluid with a jet-fluid concentration between 0.1 and 0.9. The spanwise component of velocity,  $w$ , is not expected to contribute to the SICV measurements, and was excluded from the velocity magnitude  $|\bar{\mathbf{u}}|$ .

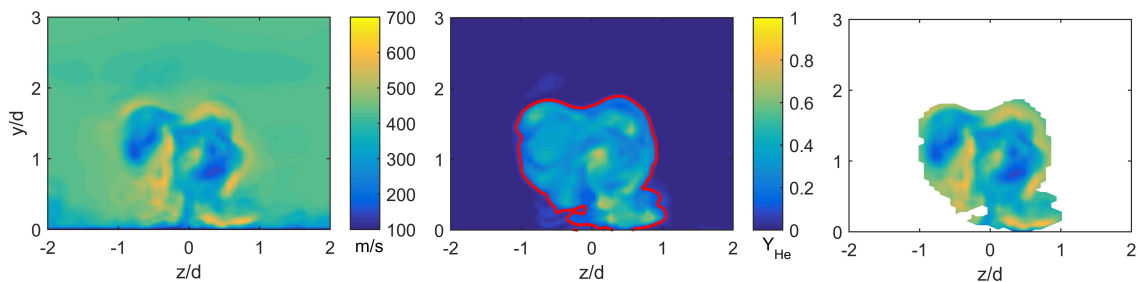


Figure 2.9: Velocity magnitude slice (left), jet-fluid concentration slice (center), and conditional velocity slice (right), derived from the LES results by E. Luthman. The  $Y_{\text{He}} = 0.1$  contour is outlined in red.

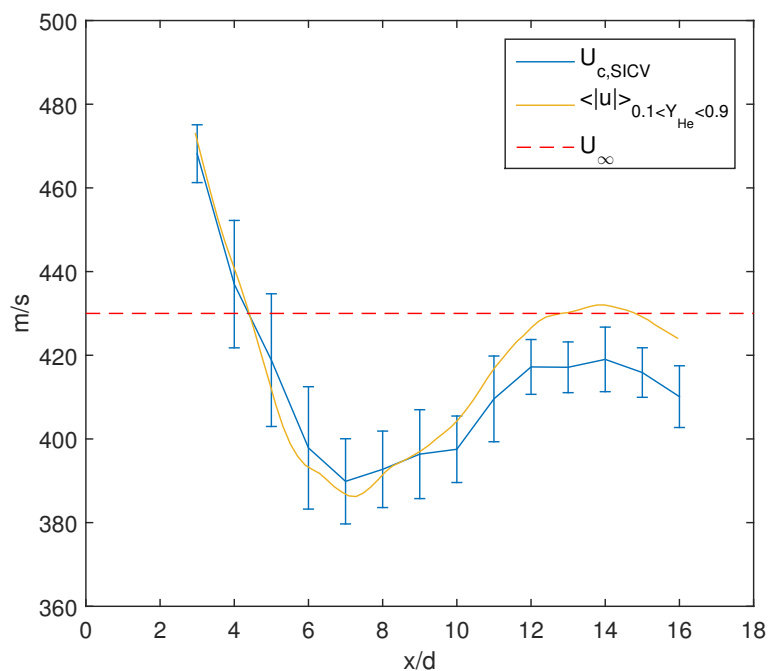


Figure 2.10: Binned SICV measurements using simulated-shadowgraph image pairs, and velocity magnitude of fluid with a jet-fluid mass-fraction of  $0.1 < Y_{\text{He}} < 0.9$ . Uncertainty bars in the SICV estimates mark the  $\pm\sigma$  estimated convective velocity within each bin.

Figure 2.9 shows the process of conditioning the velocity magnitude (left) of a given frame and

streamwise location by the jet-fluid mass-fraction (center), to generate a conditional velocity slice (right). The  $Y_{\text{He}} = 0.1$  contour is outlined in red. At this location, the jet fluid has a maximum concentration lower than 0.9. The mean conditional velocity at the particular streamwise location is then determined by spatially averaging the conditional velocity for each of the 32 frames, and averaging that value over the 32 frames. Figure 2.10 plots the frame- and spatially averaged velocity from the LES, and the binned convective velocity estimated using SICV on a 32-frame pair set of artificial shadowgraphy images. These results indicate that the SICV measurements provide a good estimate for the conditional velocity in a TJISCF.

## 2.2.2 Nitrosyl fluoride (NOF) and nitroxyl (HNO) chemiluminescence system

Optical emissions are widely used in reacting flows for diagnostic applications. One source of emission is chemiluminescence, the emission of photons from excited molecules as they relax to a lower state. In reacting flows, sources of chemiluminescence are typically short-lived excited species that exist primarily in combustion reaction zones. A chemiluminescence image is a 2D projection, or a path integral, of chemiluminescence emitted by a volume of reacting and optically emitting fluid, as opposed to planar laser induced fluorescence (PLIF), for example. Chemiluminescence is then well suited to measuring line-integral quantities such as heat release (e.g., Gaydon and Wolfhard 1970). In the hypergolic system of premixed hydrogen and nitric oxide reacting with fluorine, chemical reactions and chemiluminescence begin almost instantaneously (within 1 microsecond) in molecularly mixed fluid, and without an appreciable ignition delay. In the current set of experiments, chemiluminescence is used as a marker of regions of molecularly mixed fluid that is reacting to produce short-lived atomic fluorine and hydrogen. These are then intermediates to the formation of chemiluminescent species.

Excited nitrosyl fluoride (NOF\*) and nitroxyl (HNO\*) are, in turn, intermediate species in the reactions of atomic fluorine with nitric oxide, and atomic hydrogen with nitric oxide, i.e.,



that emit light as they decay to a lower state,



Further detail on the chemical mechanism describing the reactions of premixed hydrogen and nitric oxide with fluorine is shown in Appendix B. Johnston and Bertin (1959) found that the reaction of F with NO produces a continuous visible emission between 510 and 640 nm, with a maximum intensity at  $609.5 \pm 0.5$  nm. NOF\* chemiluminescence has been used to investigate reaction kinetics by Skolnik et al. (1975) and Rapp and Johnston (1960). It shares some similarities, including the emission spectrum, with the ‘air afterglow’ effect that occurs during the recombination of atomic oxygen with NO (see Becker et al. 1972). The reaction of H with NO produces a complex emission spectrum (see Cashion and Polanyi 1959, Clyne and Thrush 1962, Ibaraki et al. 1972) with high-intensity bands between 690 nm and 800 nm. Both NOF\* and HNO\* chemiluminescence intensities are directly proportional to the concentration of atomic fluorine and hydrogen, respectively, as shown in Appendix B. The details of the chemiluminescence system spectral response are discussed at the end of this section.

The relative intensity of HNO\* to NOF\* chemiluminescence is unknown in the current set of experiments. However, the concentration profiles of atomic hydrogen and fluorine bound the overall emission profile (cf. Appendix B). Figure 2.11 shows the normalized mole fraction of F and H in a homogeneous, constant-pressure ( $p = 1$  bar,  $T = 220$  K) reactor for a typical H<sub>2</sub>+F<sub>2</sub>+NO+diluents (2% H<sub>2</sub>, 0.5% F<sub>2</sub>, 0.15% NO, He+N<sub>2</sub> diluents) mixture as a function of reactor time, and the combined chemiluminescence signal,  $I_{\text{HNO}^*+\text{NOF}^*}$ , assuming an equal contribution of HNO\* and NOF\* emission to the overall chemiluminescence signal. The normalized  $X_{\text{F}}$  and  $X_{\text{H}}$  profiles bound the uncertainty in the interpretation of the chemiluminescence signal.

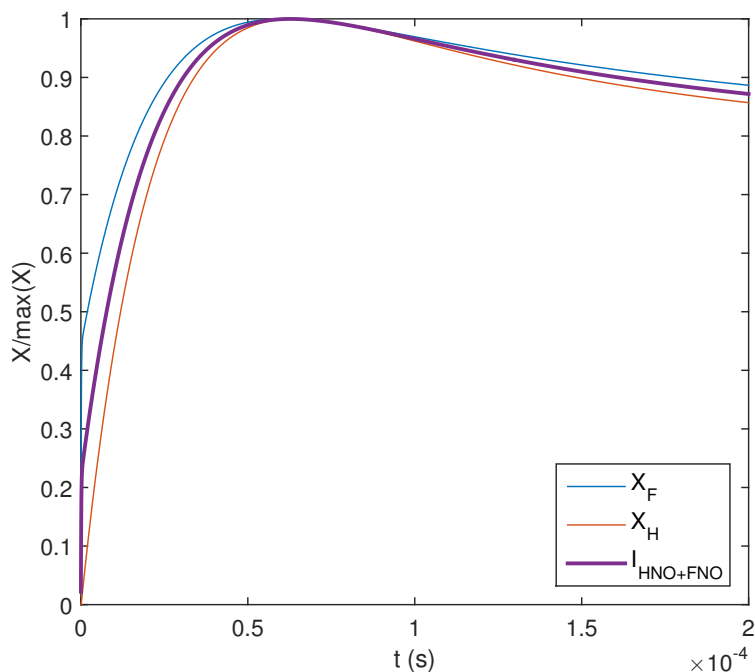


Figure 2.11: Normalized atomic fluorine and hydrogen mole fractions, and estimated average HNO\*+NOF\* chemiluminescence in a homogeneous reactor, assuming equal contributions from each species

In the experiments reported in this thesis, combined HNO\* and NOF\* chemiluminescence marks jet (diluted fluorine) and crossflow (diluted hydrogen and nitric oxide) fluid that is molecularly mixed and reacts to produce atomic fluorine and hydrogen that are responsible for chemiluminescence. Appendix B describes details of the  $F_2+NO+H_2$  chemical-kinetic mechanism incorporating NOF\* and HNO\* chemiluminescence.

Chemiluminescence passes through a 570 nm highpass dichroic filter that splits the light into the range used by the schlieren system ( $\lambda < 570$  nm) and that used by the chemiluminescence system ( $\lambda > 570$  nm). A Specialized Imaging SIL2 gated intensifier is paired with a Phantom v7.3 high-speed camera to record intensified chemiluminescence images. The intensified camera system has a quasi-linear intensity response in the range of interest, shown in Appendix B. The intensifier uses an Enhanced Red GaAsP-type photocathode with a spectral response between 320 nm and 800 nm.

The chemiluminescence system shares the same optics with the schlieren system (in reverse, see Fig. 2.4), with the intensifier time-gate closed during the time the LED is pulsed to avoid any interference. The system captures 1200 chemiluminescence images per second, each dodging the LED pulses and integrated for  $750 \mu\text{s}$ . A typical, time-averaged chemiluminescence image, as shown in Fig. 2.12, is generated by subtracting the average background noise from the average chemiluminescence signal obtained from 100 images, obtained over a period of 75 ms. For each run,  $N_I = 10$  time-averaged chemiluminescence images are obtained.

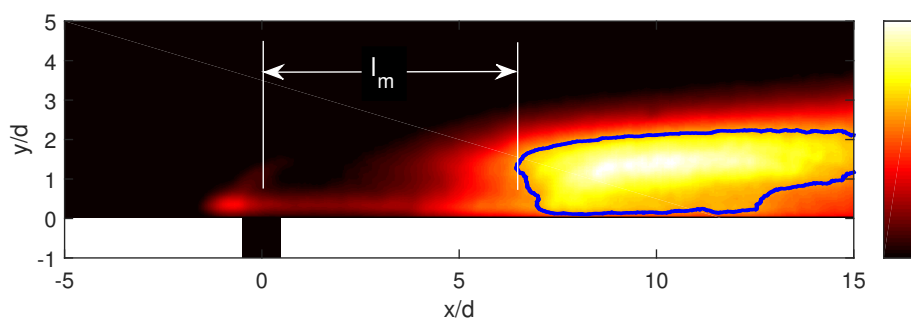


Figure 2.12: Typical reacting TJICF chemiluminescence image showing the mixing-delay length and jet body (Run ss1708)

The mixing-delay length for each image is defined as the distance between the center of the injector orifice and the region where the time- and spanwise-averaged chemiluminescence intensity is at least 0.6 of maximum signal in the jet wake. This region is outlined in blue in Figure 2.12. The mixing-delay length for the run,  $l_m$ , is obtained by averaging the individual ( $N_I = 10$ ) mixing-delay lengths. The uncertainty of the measurement is defined as the spread (difference between maximum and minimum value) in the individual mixing-delay measurements, and is represented using uncertainty bars in the results.<sup>7</sup> The sensitivity of the results to the chosen 0.6 threshold value is discussed in Section 3.3.

Experiments are performed with two jet and crossflow reactant concentrations (see Table 2.2), each with a different characteristic chemical timescale  $t_{\text{chem}}$ , defined as the time at 0.6 of the maximum estimated combined chemiluminescence signal,  $I_{\text{HNO}^*+\text{FNO}^*}$ , shown in Fig. 2.13. The chemical

<sup>7</sup>This uncertainty-quantification approach is typical for data obtained in S<sup>3</sup>L (e.g., Bergthorson et al. 2009)

timescale is obtained using homogeneous reactors at  $T = 220$  K,  $p = 1$  bar (typical of the experimental conditions), reactant concentrations in Table 2.2, with He+N<sub>2</sub> diluents, shown in Appendix D.

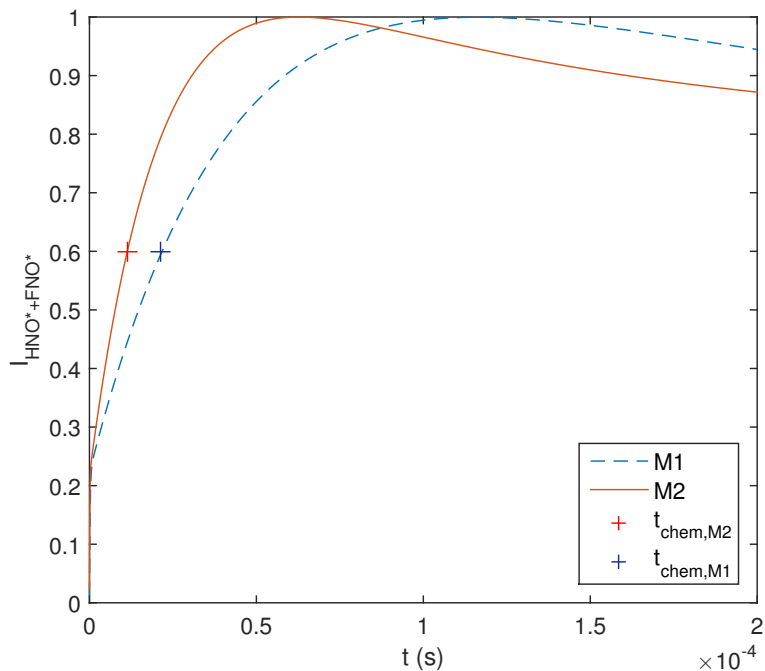


Figure 2.13: Chemical timescale for M1 and M2 mixtures, defined as the time at 0.6 of maximum chemiluminescence. See text for details.

Table 2.2: Reacting-gas composition

Name	$X_{\text{H}_2}$ (crossflow)	$X_{\text{NO}}$ (crossflow)	$X_{\text{F}_2}$ (jet)	$t_{\text{chem}}$ ( $\mu\text{s}$ )	$Da$
M1	0.02	0.0015	0.005	21	3.5
M2	0.04	0.0030	0.01	11	7.0

These reactant concentrations produce chemical timescales that are shorter than the convective flow timescales. The convective flow timescale,  $t_{\text{flow}}$ , can be defined, *a posteriori*, in terms of the characteristic mixing-delay length and the crossflow speed, i.e.,  $t_{\text{flow}} = l_{\text{m, char.}}/U_{\infty}$ . The convective flow timescale can be interpreted as the time-of-flight of a jet-fluid element between injection, and

molecular mixing, chemical reaction, and chemiluminescence. The characteristic mixing-delay length  $l_{m,\text{char.}}$  is defined as a representative value of the measured mixing-delay length,  $l_m$ , in the current set of experiments, as illustrated in Fig. 2.12. Based on the experimental results presented in the following chapter, the characteristic mixing-delay length is defined as  $l_{m,\text{char.}} \sim 6 d_{j,\text{RN1}} \sim 30$  mm. The chemical timescale is defined as the chemical reaction time at 0.6 of the maximum estimated combined chemiluminescence signal. The chemiluminescence timescale is considerably smaller than the temperature-rise timescale for the mixtures used in the present set of experiments, as shown in Fig. 2.14, and is also the measured quantity (cf. Figs. 2.13 and 2.12).

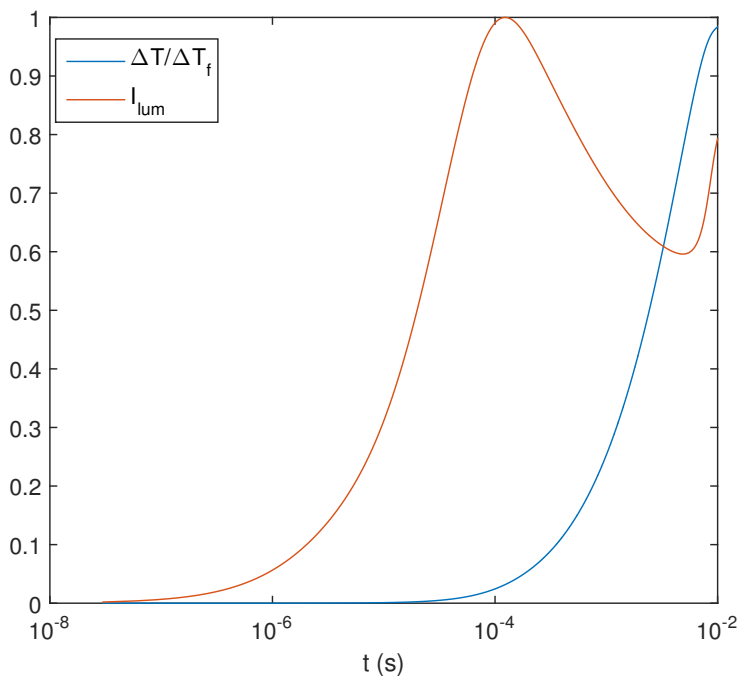


Figure 2.14: Chemiluminescence,  $I_{\text{lum}}$ , and temperature rise,  $\Delta T$ , normalized by the adiabatic, equilibrium temperature rise,  $\Delta T_{\text{f}}$ , for mixture M1 in Table 2.2, at  $T_0 = 200$  K, and  $p_0 = 1$  bar.

The Damköhler number, or ratio of flow to chemical timescales defined in the previous paragraph,

$$Da = \frac{t_{\text{flow}}}{t_{\text{chem}}}, \quad (2.6)$$

is larger than unity both mixtures for the flow conditions in the present set of experiments. It will be shown in Section 3.4 that halving the chemical timescale only decreases the length between the jet orifice and the location of 0.6 of maximum chemiluminescence by less than 15%, confirming that measured distance is primarily a mixing-delay length.

The dual-use optics system records simultaneous schlieren and chemiluminescence images that are then coregistered and combined in a post-processing phase to form overlaid schlieren-luminescence images. The combined overlaid image provides more-complete information and marks where chemical reactions occur with respect to the TJISCF flowfield. Figure 2.15, for example, illustrates where chemical reactions occur, i.e., primarily in the wake region of the jet body.

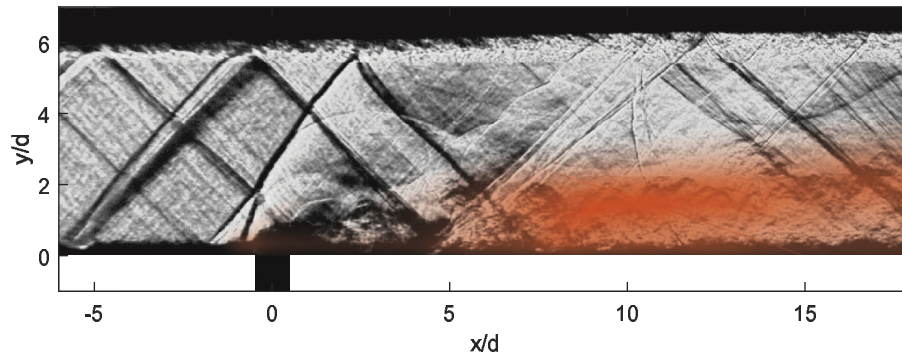


Figure 2.15: Overlaid time-averaged chemiluminescence and schlieren image (Run ss1708)

## Chapter 3

# Experimental results

This chapter presents results of experiments that examine the effects of jet-fluid molar-mass, jet-orifice diameter, and jet inclination on the reacting flowfield of transverse jets in supersonic crossflow (TJISCF).

### 3.1 Jet-fluid molar mass effects

Recent interest, investment, and research and development efforts have pivoted away from high Mach number, hydrogen-fueled scramjets (e.g., the NASP, X-43, and Kholod programs, see Curran 2001, Roudakov et al. 1996) towards lower Mach number, hydrocarbon-fueled scramjets (e.g., the X-51 and HIFiRE programs, see Hank et al. 2008, Dolvin 2008). This has motivated research into differences between hydrogen and complex-hydrocarbon fuels in the context of supersonic mixing and combustion with jet-in-crossflow fuel injection. One aspect that has received attention is the effect of jet-fluid molar mass,  $W_j$ , on crossflow fluid entrainment, dispersion, and molecular mixing in the jet body. Ben-Yakar et al. (2006), Gruber et al. (1997a), Gamba et al. (2015), and others reported a correlation between jet-fluid molar mass and jet spreading and molecular mixing. Lower- $W_j$  jets are reported by these authors to remain coherent further downstream than higher- $W_j$  jets. Gruber performed cold-flow, non-reacting experiments with sonic helium and air transverse (normal) jets injected into a supersonic ( $M_\infty = 1.98$ ) air crossflow, and attributed the increased mixing<sup>1</sup> observed

---

<sup>1</sup>What Gruber et al. (1997a) refers to as ‘mixing’ is referred to as ‘dispersion’ in this thesis

in the air-air TJICF system to compressibility effects. The faster helium jet has a higher convective Mach number,  $M_c$ , at the leading edge shear layer formed at the interface between jet-fluid and freestream fluid upstream of the jet than an air jet, whose velocity is closer to that of the crossflow. Compressibility effects associated with a large convective Mach number decrease the growth rate of a planar shear-layer, as reviewed in Dimotakis (1991), and Gruber argues that the same applies to sheared regions of a jet in crossflow.

Ben-Yakar performed reacting experiments with cold sonic hydrogen and ethylene jets in a heated supersonic air crossflow ( $T_\infty = 1290$  K,  $M_\infty = 3.38$ ). OH-PLIF measurements at the center plane of the jet revealed that the hydrogen-jet reaction zone is thin and located primarily at the interface of the jet and crossflow, while the ethylene jet reaction zone is more distributed in and encroaches on the jet body. Based on these observations, Ben-Yakar concluded that improved mixing between the (higher- $W_j$ ) ethylene jet and heated-air crossflow was responsible for the more-distributed nature of the reaction zone. She attributed improved mixing to larger velocity differences between the ethylene jet and crossflow than between the hydrogen jet and crossflow. It should be noted, however, that ethylene and hydrogen have different combustion characteristics that could be at least partly responsible for the observed differences in reaction-zone structure.<sup>2</sup>

Gamba et al. (2015) performed cross-plane non-reacting toluene-PLIF measurements to visualize the structure of  $J = 2.4$  jets in supersonic ( $M_\infty = 2.3$ ) crossflow across a wide range of jet molar-mass values. He found that the jet potential core in low- $W_j$  jets remains coherent farther downstream when compared to high- $W_j$  jets. He observed that the jet leading edge mixing-layer structure depends on jet-fluid molar mass. The mixing region of a low- $W_j$  jet just downstream of the bow shock remains thin and regular around the jet potential core, with a structure reminiscent of a planar shear layer. In a high- $W_j$  jet, the mixing region rapidly develops large-scale structures that penetrate and break down the potential core structure. He suggests that the turbulent structure of the jet depends on the injectant-fluid molar mass and plays an important role in entrainment and mixing in such a flow.

Experiments were performed in the S<sup>3</sup>L facility to isolate the effects of jet-fluid molar-mass on molecular mixing and convective velocity in TJISCF. In particular, a transition from entrained and dispersed jet and crossflow fluid to molecularly-mixed, reacting fluid was observed in the jet

---

<sup>2</sup>The theory put forth by Ben-Yakar et al. (2006) is challenged by the data of Gruber (1997b), and *vice versa*. The lighter jet in the Gruber data has higher velocity gradients than the heavier jet, yet remains coherent farther downstream, and the heavier jet in Ben-Yakar's experiments has a higher convective Mach number, yet mixes faster than the lighter jet.

body several diameters downstream of injection (the mixing-delay length,  $l_m$ , cf. Fig. 2.12), whose location exhibits a dependence on jet-fluid molar mass,  $W_j$ .

The range of jet molar-mass, or ratio of crossflow-to-jet molar mass,  $\varpi = W_\infty/W_j$ , considered is shown in Table 3.1. Reactant concentrations correspond to the M1 mixture shown in Table 2.2. The injector geometry was that of the RN1 injector (see Fig. 2.3). Chemiluminescence was measured and processed for each one, and the convective velocity estimated from double-pulsed schlieren image sets using SICV, as discussed above. It will be shown in the following discussion that lower- $W_j$ , faster normal jets lead to higher streamwise convective velocities in the vicinity of the jet orifice. These persist some distance downstream into the jet wake, and are correlated with longer mixing-delay lengths,  $l_m$ .

Table 3.1: Jet-fluid molar-mass effects

Run	$U_\infty$ (m/s)	$U_j$ (m/s)	$J$	$\varpi$	$l_m$ ( $x/d$ )	$p_{0,j}^\dagger$	$p_{0,\infty}^\dagger$	$X_{j,dil}$
ss1708	419	855	0.88	6.59	6.6	545	510	He:0.995
ss1714	427	686	0.97	4.11	6.2	531	558	He:0.9,N <sub>2</sub> :0.095
ss1718	427	372	0.98	1.20	6.0	531	558	He:0.495,Ar:0.5
ss1722	427	277	0.98	0.66	5.1	531	558	Ar:0.995

$^\dagger$  (kPa)

While the crossflow-fluid molar mass  $W_\infty$  and velocity was kept approximately constant, the composition of the jet diluents ranged from pure argon (crossflow-to-jet molar mass ratio  $\varpi = W_\infty/W_j = 0.66$ , jet exit velocity  $U_j = 277$  m/s) to pure helium ( $\varpi = 6.59$ ,  $U_j = 855$  m/s). The crossflow diluent molar composition was 4% He, 93.85%N<sub>2</sub>, with the exception of Run ss1708, whose crossflow diluent was pure N<sub>2</sub>. The He-N<sub>2</sub> mixture was employed to maintain a sound speed that is independent of reactant concentration, by offsetting the decrease in sound speed at low H<sub>2</sub> reactant concentrations with helium. Momentum-flux ratios were  $J = 0.97 \pm 0.02$ , except for Run ss1708 that was performed at a slightly lower  $J$  value. The jet-fluid stagnation temperature was ambient,  $T_{amb} \simeq 295$  K, and the crossflow fluid temperature was  $T_{amb} - 6 = 289$  K.<sup>3</sup>

<sup>3</sup>The 6 K temperature drop in the crossflow is noted in Hall (1991) and is attributable to the Joule-Thomson effects.

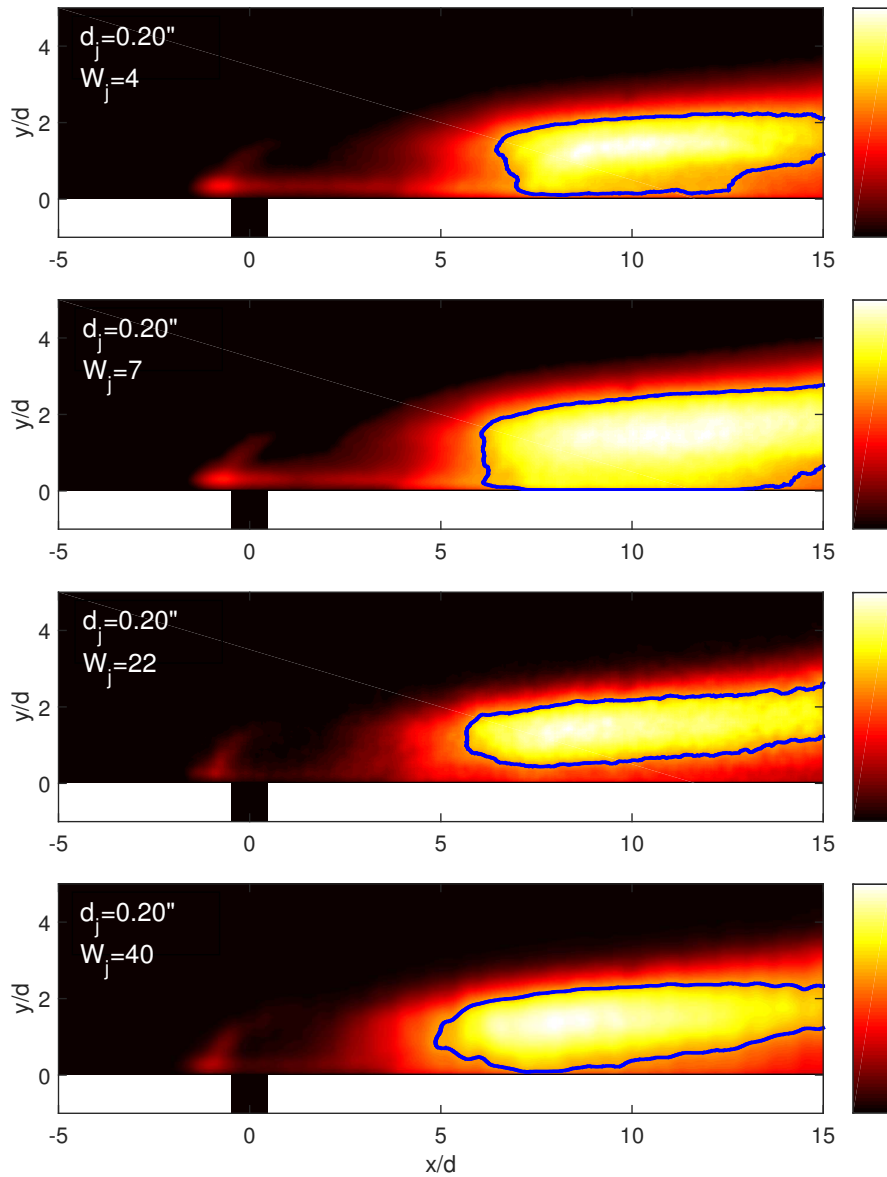


Figure 3.1: From top to bottom, chemiluminescence images of Runs ss1708 (helium jet), ss1714, ss1718, and ss1722 (argon jet). The mixing-delay length decreases with increasing jet-fluid diluent molar mass,  $W_j$ . The colorbar scale ranges from 0 to 1 and corresponds to the chemiluminescence intensity normalized by its maximum value. The blue contour is the 0.6 locus of the maximum chemiluminescence signal.

The mixing-delay length  $l_m$  is defined as the location downstream of the jet orifice of 0.6 of the maximum chemiluminescence intensity (cf. Fig. 2.12). The chemiluminescence images recorded in the experiments listed in Table 3.1, shown in Fig. 3.1, help qualitatively illustrate the upstream shift, as jet-fluid molar mass increases, of the location at which the jet body transitions to a state of molecularly mixed, chemically reacting fluid. The colorbar of each image ranges from zero to unity, and corresponds to the chemiluminescence intensity normalized by the maximum chemiluminescence signal in each image.

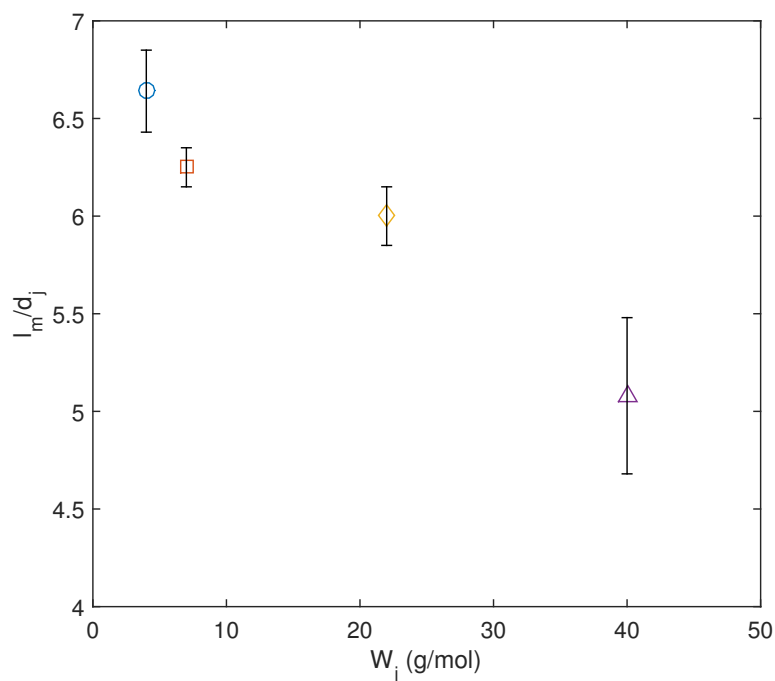


Figure 3.2: Jet-fluid molar-mass effects on mixing-delay length. Uncertainty bars represent the individual measurement uncertainties discussed in Section 2.2.2.

In all cases, there is a clear transition in the jet body to molecularly-mixed, reacting fluid that emits chemiluminescence. The transition occurs between five and seven jet diameters downstream of injection, depending on jet-fluid molar mass. Molecular mixing, reaction, and chemiluminescence also occur in the recirculation zone upstream of the jet, and in the boundary layer surrounding the jet orifice. These regions are of particular importance in a reactant system subject to induction autoignition delays (i.e., non-hypergolic fuels). Ben-Yakar (2000) and Gamba and Mungal (2015a)

identified the upstream recirculation zone as an important flameholding mechanism in reacting hydrogen and ethylene TJISCF systems. Gamba also showed that the near-wall reaction zone in the boundary layer can be as extensive as that in the jet body, in the case of hydrogen-air. This was also observed in simulations (see Ch. 5).

The jet-diameter-normalized mixing-delay lengths are plotted in Fig. 3.2 (note displaced origin), against the jet-fluid molar-mass,  $W_j$ . Increasing the jet-fluid molar mass decreases the mixing-delay length. While the effect of jet-fluid molar mass on the mixing-delay length is unmistakable, it is weak. Increasing the jet-fluid molar mass from approximately 7 g/mol (Run ss1714) to 40 g/mol (Run ss1722, a factor of six) decreases the mixing-delay length by only about 20%.

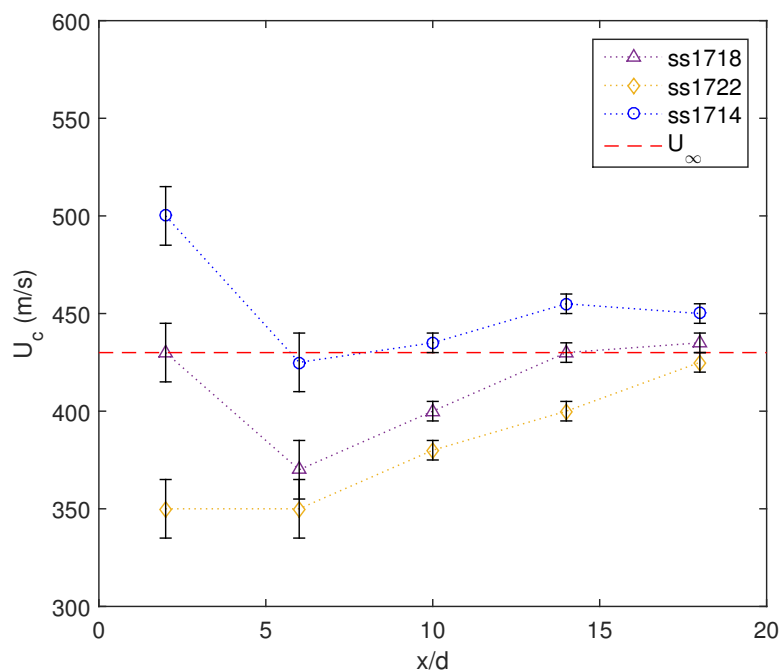


Figure 3.3: Convective-velocity estimated using SICV. The uncertainty bars represent the typical standard deviation of the convective velocity measurements in the bin,  $\pm\sigma$ , at that location (cf. Fig. 2.7)

Convective velocity in the jet body was estimated using SICV for  $J$ -matched and  $U_\infty$ -matched Runs ss1714, ss1718, and ss1722, at five downstream stations (bins) as shown in Fig. 3.3. Jets with

lower- $W_j$  jet-fluid and higher soundspeed have higher convective velocities immediately downstream of the jet orifice ( $x/d \sim 2$ ) than the jets with lower soundspeed values. In all cases, the convected fluid quickly decelerates to a minimum (at approximately  $x/d = 6$ ), then re-accelerates to values close to the freestream velocity. The higher convective velocity of the lower- $W_j$  jets persists downstream even after the jet-fluid re-accelerates, as shown in Fig. 3.3.

The deceleration then re-acceleration of the jet fluid can be explained by the interaction of the jet with the crossflow just downstream of the bow shock. The crossflow gas is shocked down to  $M_{\infty,2} < 1$  by the near-normal bow shock ahead of the jet and re-accelerates downstream of the shock to match the free stream. The under-expanded jet exits the orifice at sonic conditions, and rapidly accelerates to  $M_{j,2} > 1$ . Santiago and Dutton (1997) report a jet Mach number of  $\sim 2$  just upstream of the Mach disk and barrel shock structure (cf. Fig. 1.1) for comparable conditions (sonic air jet in  $M_\infty = 1.6$  crossflow,  $J = 1.7$ ). The jet fluid rapidly decelerates as it entrains (possibly) subsonic post-shock crossflow fluid, but re-accelerates as the crossflow accelerates to approach the pre-shock freestream velocity.

It is tempting, and typical (e.g., Gruber et al. 1997a), to interpret the mixing-delay length and convective-velocity observations in terms of the well-understood, experimentally validated expressions for entrainment, mixing, and convective velocity of planar shear layers (reviewed in Dimotakis 1991). The convective velocity,  $U_{c,SL}$ , at the  $x/d = 2$  location, in fact, is close to that predicted for an incompressible planar shear layer formed between a (hypothetical) sonic stream of (Ar+He) jet fluid, and a  $M = 1.5$  stream of ( $N_2$ ) crossflow fluid, at conditions typical of those in the experiments considered here, i.e.,

$$\frac{U_{c,SL}}{U_1} \simeq \frac{1 + r_{SL}s^{1/2}}{1 + s^{1/2}}, \quad (3.1)$$

where  $U_1$  is the high-speed stream velocity, and  $r_{SL}$  and  $s$  are the low-to-high speed stream velocity and density ratios, as shown in Fig. 3.4 (top right).

However, the predicted incompressible shear-layer growth rate (Dimotakis et al. 1984),

$$\frac{\delta}{x}(r_{SL}, s) \simeq C_\delta \frac{(1 - r_{SL})(1 + s^{1/2})}{2(1 + s^{1/2}r_{SL})} \left[ 1 - \frac{(1 - s^{1/2})/(1 + s^{1/2})}{1 + 2.9(1 + r_{SL})/(1 - r_{SL})} \right], \quad (3.2)$$

where  $\delta$ , here, is the visible thickness, and empirically,  $C_\delta \simeq 0.37$ , and the predicted mixing transition region,  $l_{tr,SL}$ , i.e., the predicted region at which the Reynolds number based on the shear-layer thickness ( $\delta$ ) reaches  $\approx 10^4$  (Konrad 1977, Dimotakis 1991, 2000), in such a planar shear layer do not account for the TJISCF behavior observed in the present experiments.

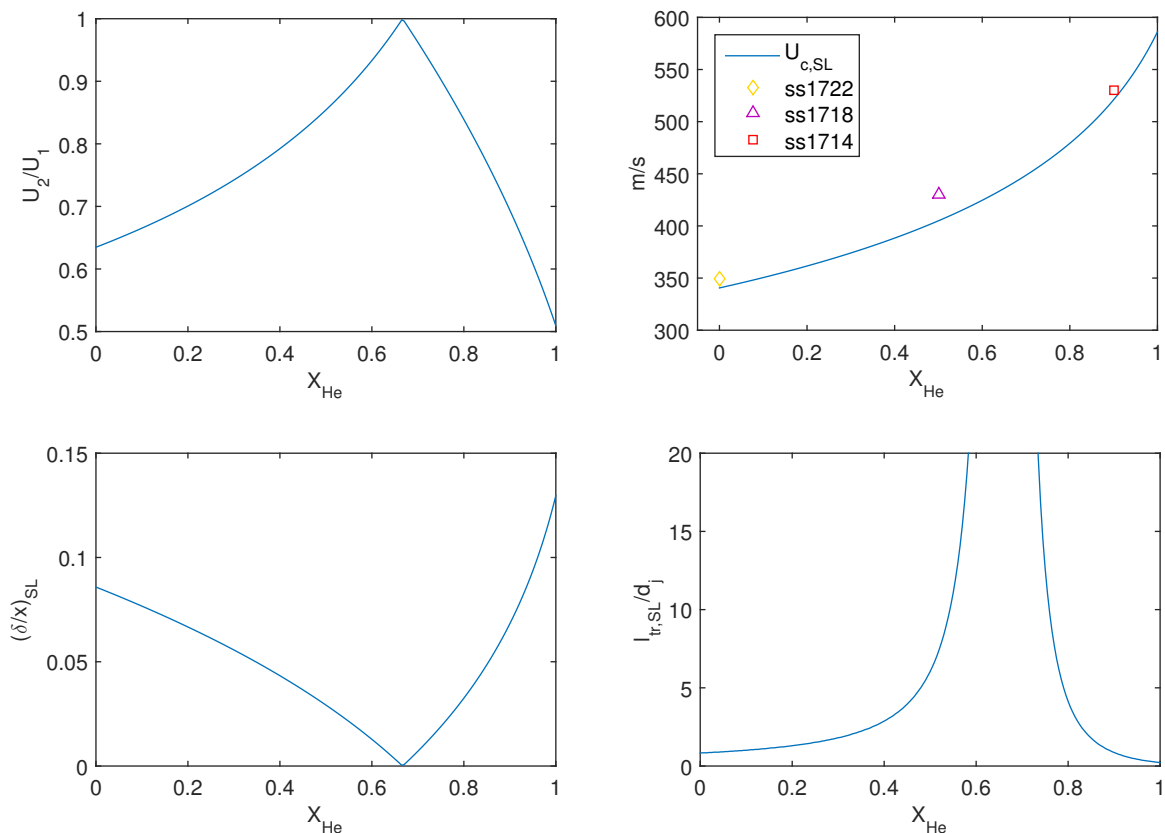


Figure 3.4: Shear-layer velocity ratio (top left), convective velocity with measured TJISCF near-jet convective velocity (top right), growth rate (bottom left), start of mixing transition ( $Re_\delta > 10^4$ , Konrad 1977, Dimotakis 1991, 2000) in jet diameters, for  $d_j=0.2$  in. (bottom right)

Figure 3.4 (bottom left) plots the growth rate of a planar shear layer as a function of jet fluid helium mole fraction. If applied to a TJISCF, these relations would predict that a helium jet would have a higher growth rate, and transition to molecular mixing farther upstream than an argon jet. Moreover, at certain helium concentrations, it should exhibit near-zero growth rate (if  $U_1 \approx U_2$ , Fig.

3.4, bottom left), and would not transition to the  $Re > 10^4$  turbulent mixing regime at all (Fig. 3.4, bottom right). These predictions do not agree with available experimental data, indicating that planar shear-layer relations do not apply to the TJISCF.

While sheared regions are certainly present at the interface between the leading edge of the jet and the post-shock crossflow, for example, fluid streams that form the mixing region are not uniform or well characterized. Moreover, the toluene PLIF images of Gamba et al. (2015) show that the jet leading-edge mixing-region structure is different than that of a planar shear layer. Instead of deconstructing the TJISCF into smaller elements, it may be better to interpret the TJISCF as a whole and focus on its response to global parameters. An important global parameter is the jet Reynolds number, whose influence is discussed in the following section.

## 3.2 Jet-diameter effects

Most properties of a transverse jet in crossflow are reported to scale with jet diameter. In particular, both weak-jet (low- $J$ ) and strong-jet (high- $J$ ) expressions for jet penetration and trajectory are normalized by the jet diameter (cf. Section 1.1). The mean jet-fluid concentration decay as a result of dispersion and mixing along the jet axis of momentum-dominated (strong) jets in crossflow scales with jet diameter by mass and momentum conservation arguments (cf. Hasselbrink and Mungal 2001). Lin et al. (2010) measured time-averaged jet-fluid concentration using Raman scattering in a weak ( $J \sim 2$ ) jet in supersonic crossflow for two jet diameters and found that the mean jet-fluid concentration scales with jet diameter. Changing the jet diameter directly affects the Reynolds number, for example, that influences mixing and combustion processes across a range of scales. We pose the question: does mixing-delay length in a TJISCF scale with jet diameter, or have a different dependence on jet diameter and associated jet Reynolds number?

The Reynolds number plays a fundamental role in the transition to turbulent molecular mixing. In a planar shear layer, the transition to rapid molecular mixing (Konrad 1977, Koochesfahani and Dimotakis 1986) begins some distance downstream of the splitter plate, at a local Reynolds number based on the shear-layer thickness of approximately  $10^4$ , that has since been identified as a quite-general threshold value for transition to turbulent mixing by Dimotakis (2000). Reynolds number effects become weak at Reynolds numbers beyond the mixing transition. This is also true in the

far-field, self-similar regions of axisymmetric jets (Gilbrech 1991, Dimotakis 2000).

Mixing in the near field of a gas-phase axisymmetric jet, however, remains Reynolds-number dependent even beyond the mixing transition. Gilbrech performed fast-chemistry axisymmetric gas phase jet experiments using diluted  $F_2$  in NO, complementing the liquid phase jet measurements of Dahm and Dimotakis (1987, 1990), and others. The liquid-phase data of Dahm and Dimotakis (1987) and gas-phase data of Gilbrech (1991) showed the flame length,  $L_f$ , has a dependence on stoichiometry,  $\phi$ , of the form

$$\frac{L_f}{d^*} = A_f \phi + B_f . \quad (3.3)$$

$d^*$  is the jet source (or momentum) diameter (e.g., Dahm and Dimotakis 1987), and is a length scale defined by the ratio of the mass flux to the (square root of) the momentum flux, with constants added that force  $d^*$  to  $d_j$  if the ambient and jet densities are equal, and if the jet exit velocity profile can be approximated by a top-hat, i.e.,

$$d^* = \frac{2\dot{m}_j}{\sqrt{\pi\rho_\infty P_j}} , \quad (3.4)$$

with  $\rho_\infty$  the ambient density, and  $\dot{m}_j$  and  $P_j$  the jet mass and momentum flux, respectively, i.e.,

$$\dot{m}_j = \rho_j A_j U_j ; \quad P_j = \rho_j A_j U_j^2 . \quad (3.5)$$

$A_f$  is the stoichiometric coefficient that was used as a measure of mixing in the far-field, self-similar region.  $B_f$  is the intercept, or ‘virtual mixing origin’. Gilbrech showed that for a given  $\phi$ ,  $A_f$  decreased with Reynolds number up to approximately  $2 \times 10^4$ , and did not change beyond that value. The ‘virtual mixing origin’, however, decreased through and beyond the transitional value of  $Re = 2 \times 10^4$  and did not approach asymptotic behavior even at a Reynolds number of 150,000. As Dimotakis (2000) notes, the Reynolds number for a jet is typically based on the jet diameter and not the transverse extent across which shear is applied, which is the radius, and as a consequence there is a factor of 2 between the mixing transition Reynolds number of a jet and that of a shear layer, and most other flows.

There are parallels between the ‘virtual mixing origin’ of an axisymmetric high-speed jet and the mixing-delay length observed in these TJISCF experiments that imply a possible mixing-delay length dependence on jet Reynolds number,

$$Re_j = \frac{\rho_j U_j d_j}{\mu_j} . \quad (3.6)$$

A set of experiments (see Table 3.2) was performed with two sets of identical jet- and crossflow-fluid compositions and pressures, but different jet-orifice diameters.

Table 3.2: Jet-diameter effects

Run	Inj.	$U_\infty$ (m/s)	$U_j$ (m/s)	$J$	$\varpi$	$l_m$ ( $x/d$ )	$X_{j,dil}$
ss1719	RN2	427	686	0.96	4.11	5.1	He:0.9,N <sub>2</sub> :0.095
ss1714*	RN1	427	686	0.97	4.11	6.2	He:0.9,N <sub>2</sub> :0.095
ss1720	RN2	427	277	0.95	0.66	4.2	Ar:0.995
ss1722*	RN1	427	277	0.98	0.66	5.1	Ar:0.995

\*cf. Table 3.1

The results help examine the effects of jet diameter and associated jet Reynolds number ( $Re_j$ ) on the reacting flowfield, and in particular, help determine whether the mixing-delay length has an  $Re_j$  dependence.

Figure 3.5 shows chemiluminescence images of lower- $W_j$  (He+N<sub>2</sub>, ss1714, ss1719) and higher- $W_j$  (Ar, ss1722, ss1720) jets with dimensions scaled by the jet diameter, where  $d_j$  is either 0.508 cm (0.20 in.), or 0.635 cm (0.25 in.). While jet penetration is also observed here to scale with jet diameter, as expected and reported in the literature (e.g., Lin et al. 2010), chemiluminescence measurements show that jets with a larger diameter,  $d_j$ , mix, react and emit chemiluminescence earlier, i.e., further upstream (in diameter-normalized units), than jets with a smaller diameter.

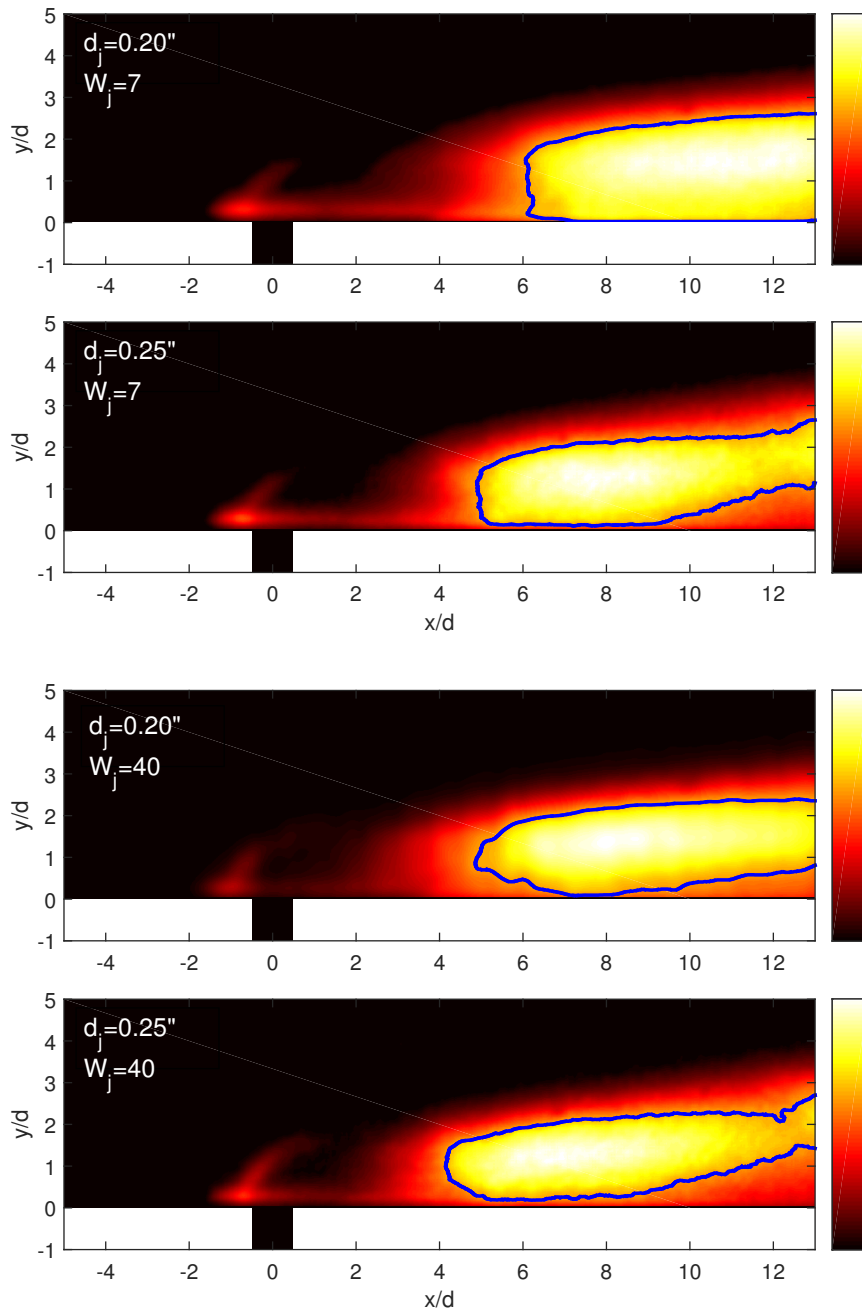


Figure 3.5: From top to bottom, chemiluminescence images from  $\varpi = 4.11$  (He+N<sub>2</sub> jet fluid) Runs ss1714,  $d_j = 0.20$  in. (top) and ss1719,  $d_j = 0.25$  in. (center top), from  $\varpi = 0.66$  (Ar jet fluid) Runs ss1722,  $d_j = 0.20$  in. (center bottom) and ss1720,  $d_j = 0.25$  in. (bottom).

Normalizing the mixing-delay length by the physical jet diameter does not collapse the data (cf. Fig. 3.6). Molecular mixing and reaction occur some distance downstream of injection, where the flow has likely ‘forgotten’ about the physical jet diameter<sup>4</sup> and the large amount of entrained mass sets the local density to that of the reservoir fluid, i.e.,  $\rho_\infty$ . An appropriate normalizing length scale would need to take density ratios into account. Such a length scale is the jet-source diameter,  $d^*$ , defined in Eq. 3.4.

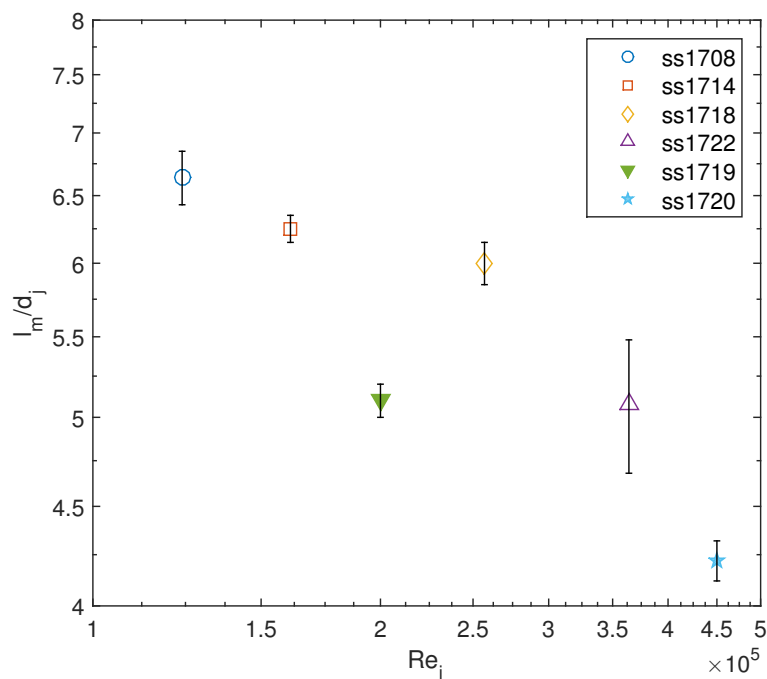


Figure 3.6: Mixing-delay length normalized by the physical orifice diameter plotted against jet Reynolds number. The uncertainty bars reflect the estimated measurement uncertainty discussed in Section 2.2.2.

The mixing-delay length  $l_m$  (cf. Fig 2.12), normalized by the jet-source diameter,  $d^*$ , is plotted in Figure 3.7 against the jet Reynolds number,  $Re_j$ , based on jet diameter,  $d_j$ , for all six experiments listed in Tables 3.1 and 3.2 (runs ss1714 and 1722 are listed in both tables).

---

<sup>4</sup>P. Dimotakis, private communication.

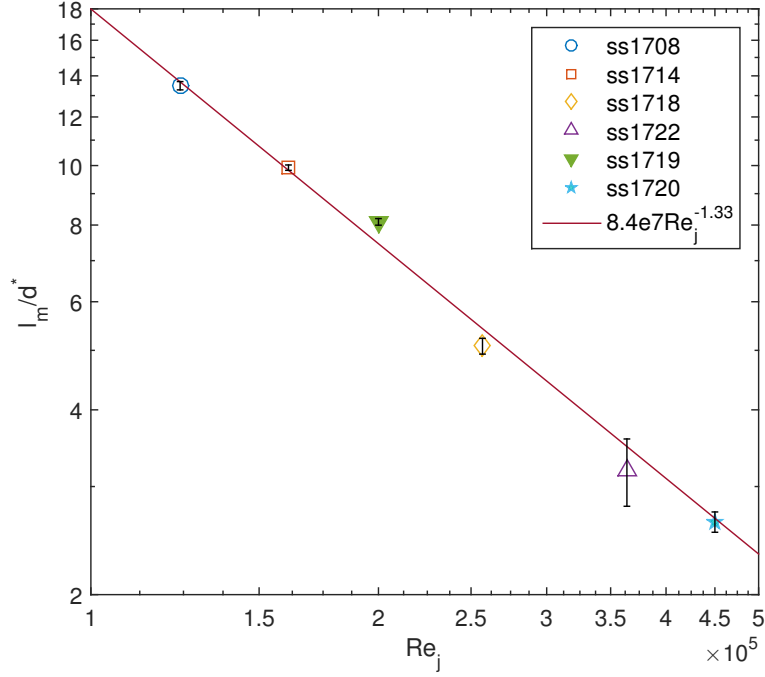


Figure 3.7: Mixing-delay length normalized by jet-source diameter plotted against jet Reynolds number. The uncertainty bars reflect the estimated measurement uncertainty discussed in Section 2.2.2.

Normalized mixing-delay lengths from experiments across a wide range of jet molar mass and different jet diameters collapse as a function of jet Reynolds number onto a power law of the form

$$\frac{l_m}{d^*} = B_l Re_j^{c_m}, \quad (3.7)$$

where  $B_l = 8.4 \times 10^7$ , and  $c_m \simeq -1.33$ . An additional fit parameter was considered as an offset, without noticeable improvement, indicating that a single parameter fit with a zero asymptote is adequate. These results reveal a strong jet Reynolds number dependence of the source-diameter normalized mixing-delay length in a TJISCF, up to jet Reynolds numbers of almost  $5 \times 10^5$ .

### 3.3 Sensitivity to mixing-delay length criteria

In order to determine the sensitivity of the results to the mixing-delay length criterion (selected as the distance between the jet-orifice center and locus of 0.6 of the maximum chemiluminescence signal, cf. Fig. 3.5) the fit illustrated in Fig. 3.7 was performed using mixing-delay length criteria of 0.5, 0.6, and 0.7 of the maximum chemiluminescence signal, shown in Fig. 3.8. The lowest value of 0.5 captured reactions in the boundary layer, that were disregarded.

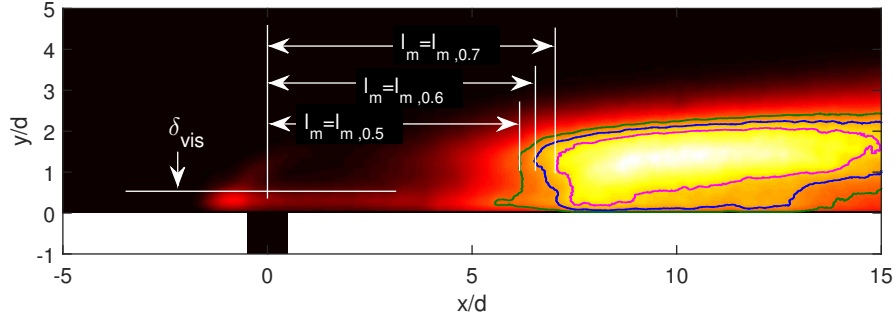


Figure 3.8: Mixing-delay length criteria of 0.5 (green), 0.6 (blue), and 0.7 (magenta) of maximum chemiluminescence signal

The results, shown in Fig. 3.9, illustrate that the prefactor,  $B_l$ , in Eq. 3.7 depends on the choice of mixing-delay length criterion, but the power-law exponent,  $c$ , is not affected by the value of the mixing-delay length criterion.

The jet molar-mass effects on entrainment, dispersion, and mixing observed by Ben-Yakar et al. (2006) and Gruber et al. (1997a) could also be interpreted in terms of jet Reynolds number. For the same dynamic viscosity and heat-capacity ratio, a sonic jet with a higher molar mass,  $W_j$ , will have a higher Reynolds number than a jet with a lower molar mass. Sound speed scales as the inverse of the square root of  $W_j$  while density is linear in  $W_j$ , i.e.,  $Re_j \propto \sqrt{W_j}$  for a sonic jet, if the heat capacity ratio,  $\gamma \neq f(W_j)$ , and viscosity,  $\mu \neq f(W_j)$ . Mixing is delayed in lower  $Re$  (lower- $W_j$ ) jet, which are therefore likely to remain coherent further downstream than higher  $Re$  (higher- $W_j$ ) jets, as observed by Ben-Yakar and Gruber.

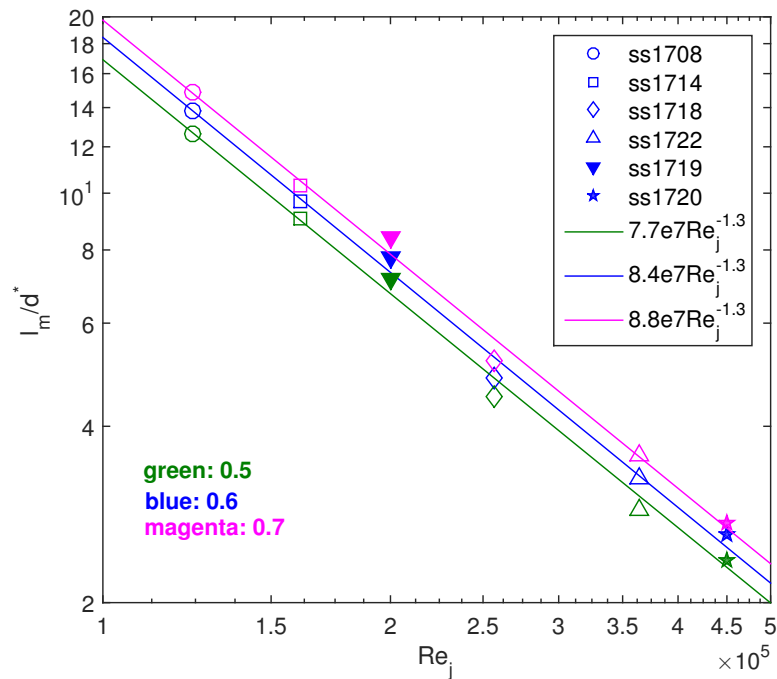


Figure 3.9: Mixing-delay length normalized by jet-source diameter plotted against jet Reynolds number, for mixing-delay length criteria of 0.5, 0.6, and 0.7 of the maximum chemiluminescence signal. Uncertainty bars omitted for clarity.

Experiments discussed in the following section address the relative contribution of mixing and chemistry to the results.

### 3.4 Chemical timescale effects

In this section, the effects of chemical timescale on the observed distance between injection and the location of 0.6 of the maximum chemiluminescence is examined. The results confirm that the observed delay between injection and chemical reactions (and associated chemiluminescence) is primarily mixing driven, i.e., it is a mixing-delay length,  $l_m$ .

In the  $H_2/NO/F_2$  system at a fixed stoichiometry, the characteristic chemical timescale is almost-

linearly dependent on reactant concentration (e.g., Mungal and Frierler 1988). In the current experiments, reactant concentrations ( $\text{H}_2$ ,  $\text{F}_2$ ,  $\text{NO}$ ) in Run ss1712 are double those in Run ss1714 (see also Table 2.2). This halves the chemical timescale (see also Table 2.2, and Fig. 2.13), while the plenum pressures and jet momentum-flux ratio are unchanged. Figure 3.10 shows the chemiluminescence images captured during runs with almost-identical flow parameters and diluent composition, but whose reactivity, as defined by the characteristic chemical timescale, is double (top) the other (bottom). The images show that increased reactant concentration somewhat increases the spatial extent of the chemiluminescence signal that is an indicator for reacting fluid. The distance between injection and the locus of 0.6 of the maximum chemiluminescence only decreases by  $\sim 15\%$ .

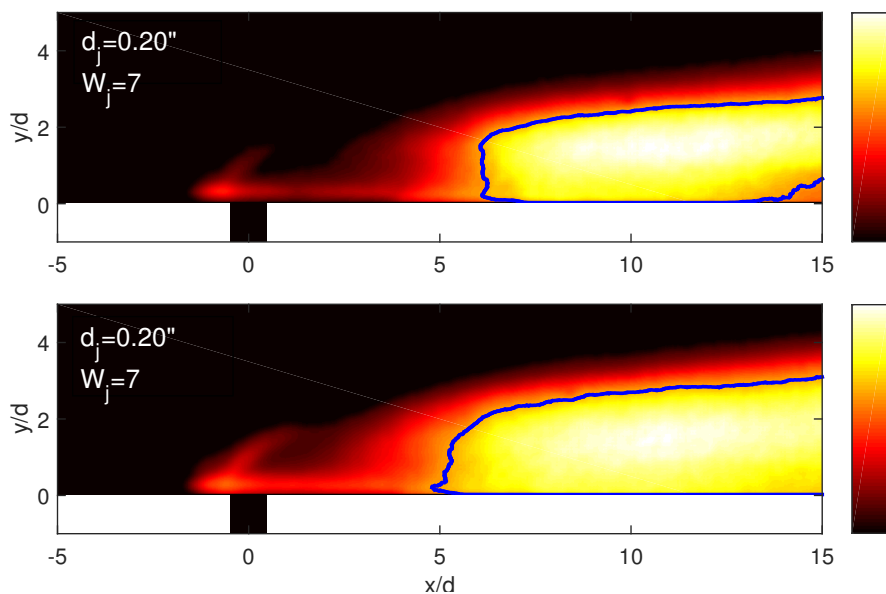


Figure 3.10: Chemiluminescence images from  $\varpi = 4.11$  Runs ss1714,  $t_{\text{chem}} = 21\mu\text{s}$  (top) and ss1712,  $t_{\text{chem}} = 10\mu\text{s}$  (bottom).

The data confirm that, in the current Damköhler number regime ( $3.5 < Da < 7$ ), the primary contributor to the distance between jet-fluid injection and the location of the bulk of chemical reactions and chemiluminescence in the jet wake is mixing, not chemical kinetics, and justifies the definition of the mixing length.

Table 3.3: Chemical-timescale effects

Run	$U_\infty$ (m/s)	$U_j$ (m/s)	$J$	$\varpi$	$l_m$ ( $x/d$ )	$X_{j,dil}$	$t_{chem}$
ss1712	427	686	0.96	4.11	5.3	N <sub>2</sub> :0.09,He:0.9	10 $\mu s$
ss1714*	427	686	0.97	4.11	6.2	He:0.9,N <sub>2</sub> :0.095	21 $\mu s$

\*cf. Table 3.1

In the case of non-hypergolic reactant mixtures with ignition-delay times longer than the chemical timescales of the present set of experiments (i.e., 10-20  $\mu s$ ), both mixing and chemistry would contribute to the mixing-delay length. For stoichiometric ethylene-air ignition at  $T_0 = 1250$  K and atmospheric pressure, for example, with a characteristic ignition-delay time on the order of 100  $\mu s$ , a Mach number of 1.5, and resulting freestream velocity on the order of 1000 m/s (sound speed of air at 1250 K is  $\sim 700$  m/s), the chemical contribution to the reaction-delay length would be on the order of 0.1 m. The primarily mixing-driven reaction-delay lengths observed in the present set of experiments are on the order of 0.025-0.04 m, indicating that reaction-delay lengths in TJISCF systems using non-hypergolic fuels in scramjet-like conditions are likely contributed to by both mixing and chemical reactions.

### 3.5 Jet-inclination effects

The normal-jet flow configuration is the most-widely studied and best-understood jet in supersonic crossflow, and is a baseline flow for studying fundamental aspects of the TJISCF, extending to inclined jets, for example. However, its use in propulsion devices is limited by disturbances it causes to the crossflow. Most importantly, the detached bow shock caused by normal injection reduces total pressure, and would affect scramjet-cycle efficiency.

Inclined jets have been considered as alternatives to normal jets for practical applications. They do not disturb the flow to the same extent, while retaining some desirable characteristics of normal TJISCF. The non-reacting inclined TJICF is not as well-studied as its non-reacting, normal counterpart, and no reacting, inclined TJICF studies have been found in the open literature. McCann and Bowersox (1996) investigated an inclined ( $25^\circ$ ) supersonic ( $M_j = 1.8$ ) jet in supersonic ( $M_\infty = 3$ )

crossflow, and found that the inclined-jet structure is dominated by a counter-rotating vortex pair in the far field, as in normal TJISCF. Lin et al. (2010) performed Raman scattering measurements of normal and inclined ( $30^\circ$ ) sonic,  $J = 1$ , ethylene jets into a  $M_\infty = 2$  crossflow, and found that the time-averaged jet-fluid concentration in the far field was considerably higher in an inclined jet than in a normal jet. This is an indication that crossflow entrainment, dispersion, and mixing could be reduced by jet inclination, negatively affecting one of the more-desirable properties of the TJISCF. Schetz et al. (2010) studied molar-mass effects on mixing in inclined TJISCF, reporting a weak correlation between penetration and jet molar mass.

Table 3.4: Jet-inclination effects

Run	Inj.	$U_\infty$ (m/s)	$U_j$ (m/s)	$J$	$\varpi$	$l_m$ ( $x/d$ )	$X_{j,dil}$
ss1724	RI1	427	635	0.96	3.6	7.5	$N_2:0.135, He:0.86$
ss1719*	RN2	427	686	0.96	4.11	5.1	$He:0.9, N_2:0.095$

\*cf. Table 3.2

Experiments discussed in this section illustrate some of the effects of jet inclination on the reacting flow field and convective velocity of a TJISCF. The jet diameter, crossflow conditions, and jet-fluid conditions were kept close to constant (cf. Table 3.4), while the jet-injection inclination angle was varied from  $90^\circ$  (normal injection) to  $30^\circ$  (inclined injection). The RI1 inclined injector (see 2.3) was investigated at the jet and crossflow conditions listed in Table 3.4, with the M1 reactant mixture (see Table 2.2).

Notably, the inclined jet molecularly mixes, chemically reacts, and emits chemiluminescence further downstream when compared to the normal TJISCF, as shown in Fig. 3.11. The mixing-delay length, defined by the locus of 0.6 of the maximum chemiluminescence in the jet body, increases from  $x/d = 5.1$  with normal injection to  $x/d = 7.5$  with inclined injection.

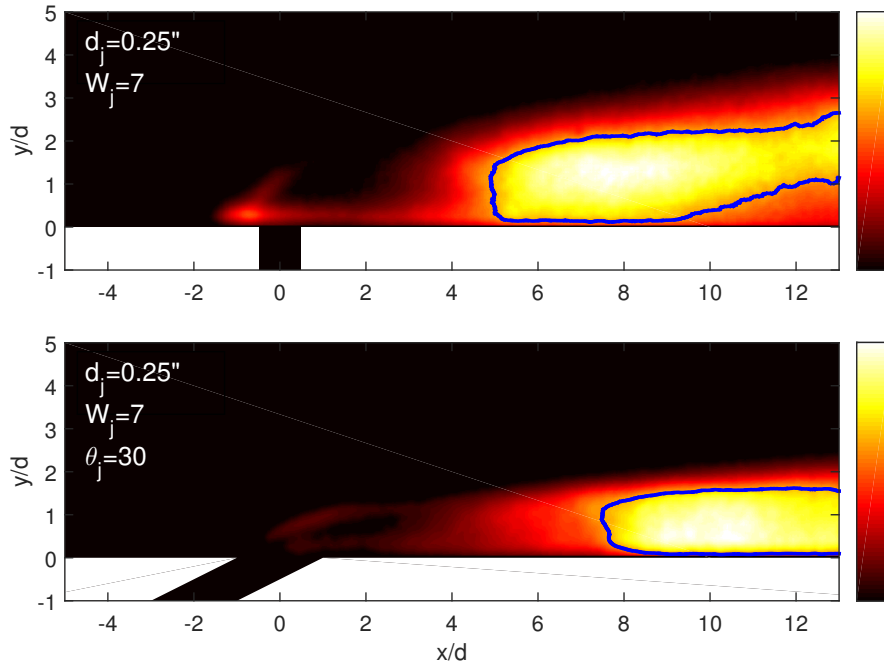


Figure 3.11: Chemiluminescence images from Runs ss1719, normal jet (top) and ss1724,  $30^\circ$  inclined jet (bottom).

Jet penetration decreases with inclination, as expected, and reactions occur closer to the wall. A recirculation zone just upstream of the jet observed in the normal injection case is not discernible in the inclined-injection case, for  $30^\circ$ . This recirculation zone was identified as an important flame-holding mechanism by Gamba and Mungal (2015a) and Ben-Yakar et al. (2006), and in large-eddy simulations detailed in this work (cf. Chapter 5). Its absence in the inclined injection case is noteworthy. On the other hand, the recirculation zone just downstream of the normal jet is also discernible downstream of the inclined jet, even though it's not as prevalent.

The flowfield structure of inclined and normal jets is quite different. Figure 3.12 shows superimposed chemiluminescence and schlieren images from two experiments that compare normal and inclined injection. A notable difference is that of the overall disturbance to the flow. The normal TJISCF generates spherical acoustic waves emanating from the near field of the jet ( $\Delta$  symbol) and a detached bow shock with a prominent  $\lambda$ -shock structure ( $\star$  symbol). The inclined TJISCF exhibits a relatively weak oblique shock, as evidenced by its angle with respect to the freestream flow, with

only a hint of a  $\lambda$ -shock structure, with no spherical acoustic waves readily discernible. Turbulent large-scale structures in the inclined jet wake are more organized and periodic, when compared to the large bulbous structures that penetrate deep into the freestream in the normal-jet wake.

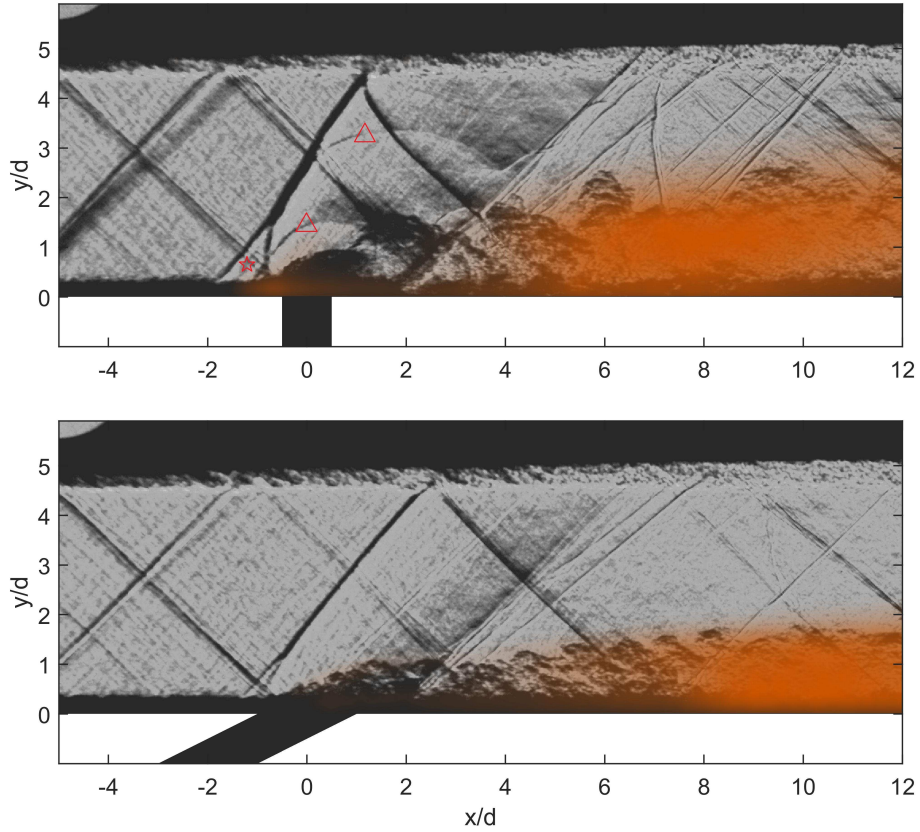


Figure 3.12: Superimposed schlieren and chemiluminescence images from Runs ss1719, normal jet (top) and ss1724, 30° inclined jet (bottom). The  $\lambda$ -shock structure ( $\star$  symbol) and spherical acoustic waves emanating from the near field of the jet ( $\Delta$  symbol) are evident in the normal jet-injection case.

The convective velocity of an inclined jet is, overall, higher than a normal jet. This is to be expected, as the inclined jet contributes a streamwise component of velocity that imparts streamwise momentum on the flow, while the normal jet does not. Figure 3.13 plots the binned convective velocity, as defined in Section 2.2.1, for the inclined and normal TJISCF.

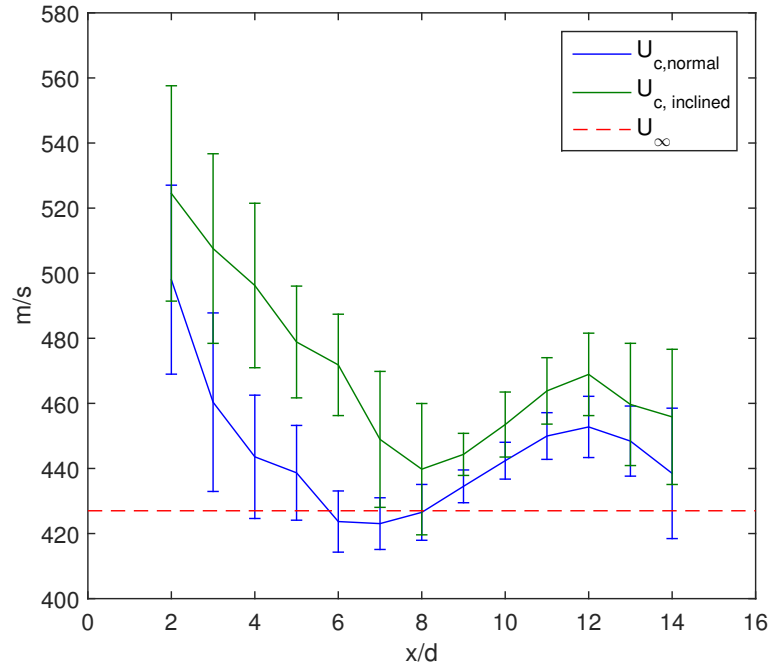


Figure 3.13: Average (binned) convective velocity from Runs ss1719 (normal jet), and ss1724 (inclined jet).

While the trends in convective velocity for the two types of jets are similar (rapid deceleration to some minimum velocity, followed by re-acceleration), the minimum velocity occurs further downstream in the inclined jet compared to that the normal jet.

### 3.6 Control-volume analysis

The effects of mass injection on supersonic flow have been explored based on one-dimensional compressible flow theory by Shapiro (1953), Heiser et al. (1996), and others. Those references describe mass-injection (and other) effects using a differential influence-coefficient matrix. The 1D approach has its limitations, particularly in flows where shocks and boundary layers cannot be ignored. However, the results illustrate important effects of mass, momentum, and energy addition on supersonic flow. An integral approach is preferable to differential approaches if mass is injected at a discrete

location. A mass, momentum, and energy control-volume (integral) analysis of a uniform-area flow with inclined mass injection was performed on the system shown in Fig. 3.14.<sup>5</sup> The boundary of the control volume is the shaded rectangular prism section shown in the diagram.

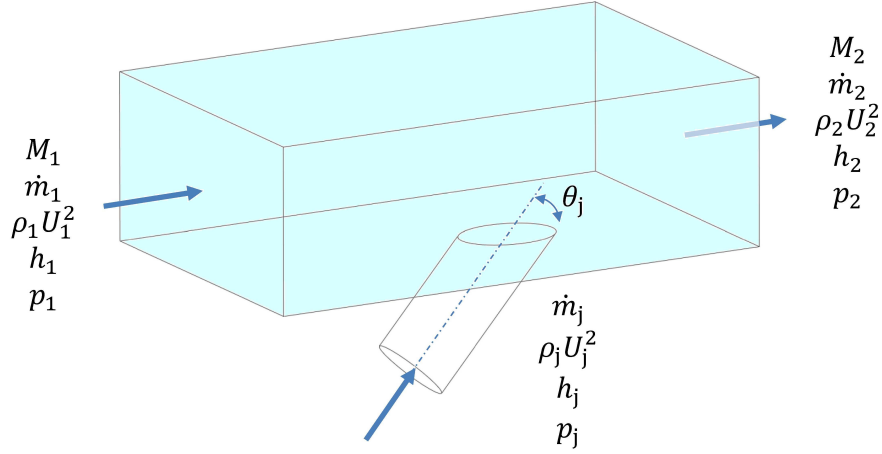


Figure 3.14: Inclined jet-in-crossflow system

Mass conservation is given by

$$\dot{m}_1 + \dot{m}_j = \rho_2 U_2 A = (\rho_1 + \Delta\rho)(U_1 + \Delta U)A, \quad (3.8)$$

where  $\Delta U = U_2 - U_1$  and  $\Delta\rho = \rho_2 - \rho_1$ . Conservation of the streamwise ( $x$  component) of momentum is given by

$$(\rho_j U_j^2 + p_j) \cos(\theta_j) + (\rho_1 U_1^2 + p_1)A = (\rho_2 U_2^2 + p_2)A, \quad (3.9)$$

where  $p_j$  is the pressure of the jet at sonic conditions, that can be larger or smaller than the freestream pressure, depending on whether the jet is under expanded or over expanded. In these experiments, the jet is under expanded, i.e.,  $p_j > p_1$ .  $\theta_j$  is the jet inclination angle. Energy conservation is given

---

<sup>5</sup>P. Dimotakis, private communication

by

$$\dot{m}_1 \left[ h_1 + \frac{U_1^2}{2} \right] + \dot{m}_j \left[ h_j + \frac{U_j^2}{2} \right] = \dot{m}_2 \left[ h_2 + \frac{U_2^2}{2} \right] , \quad (3.10)$$

where  $h$  is the static specific enthalpy. The total specific enthalpy at station (1) is that of the fluid in the hydrogen reactant tank (cf. Fig. 2.1), and the total specific enthalpy at the jet orifice is that of the fluid in the lower plenum. The conditions at station (1) are calculated based on the measured freestream Mach number ( $M_\infty = 1.43$ ). The equation of state at station (1) is

$$p_1 = \rho_1 R_{s,1} T_1 , \quad (3.11)$$

where  $R_{s,1} = R/W_1$ , and  $W_1$  is the mean molar mass at station (1). The equation of state at station (2) is

$$p_2 = \rho_2 R_{s,2} T_2 , \quad (3.12)$$

that can be rewritten as

$$p_1 + \Delta p = (\rho_1 + \Delta \rho) R_{s,2} (T_1 + \Delta T) , \quad (3.13)$$

where  $R_{s,2} = R/W_2$ .  $W_2$  is the anticipated mean molar mass at station (2) that can be estimated as,

$$\frac{1}{W_2} = \frac{Y_j}{W_j} + \frac{1 - Y_j}{W_1} . \quad (3.14)$$

$Y_j$  is the jet-fluid mass fraction in the jet and crossflow mixture at station (2), and is estimated as,

$$Y_j = \frac{\dot{m}_j}{\dot{m}_j + \dot{m}_1} . \quad (3.15)$$

Equations 3.11 and 3.13 are combined to determine  $\Delta p$ , i.e.,

$$\Delta p = (\rho_1 + \Delta\rho) R_{s,2} (T_1 + \Delta T) - \rho_1 R_{s,1} T_1 . \quad (3.16)$$

The temperature change is determined from the enthalpy change,

$$\Delta T = \frac{\Delta h}{\bar{c}_p} , \quad (3.17)$$

where  $\Delta h = h_2 - h_1$ , and  $\bar{c}_p$  is the mean heat capacity, estimated as  $(c_{p,1} + c_{p,2})/2$ .

These equations are solved numerically as a function of jet inclination for the experimental conditions in Run ss1724. The analysis reveals some interesting aspects of inclined, sonic mass injection effects on supersonic channel flow.

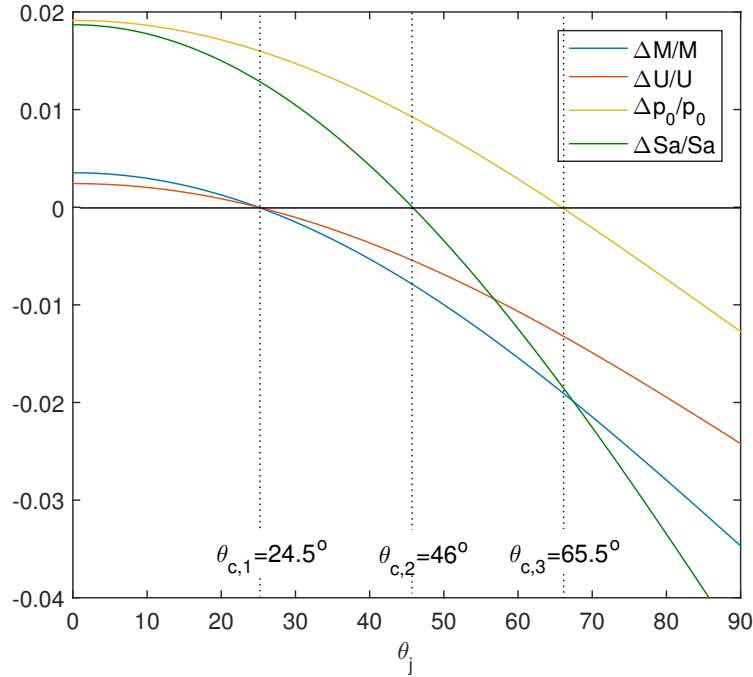


Figure 3.15: Velocity, Mach number, total-pressure, and stream thrust function,  $Sa$ , change plotted against injection angle,  $\theta_j$

Figure 3.15 plots the normalized change in velocity, Mach number, isentropically recovered total-pressure,  $p_0$ , and stream-thrust function,  $Sa$ , Eq. 3.20 (Heiser and Pratt 1994, Eq. 2-63, p. 63) against injection angle, i.e.,

$$\frac{\Delta M}{M} = \frac{M_2 - M_1}{M_1}, \quad \frac{\Delta U}{U} = \frac{U_2 - U_1}{U_1}, \quad \frac{\Delta p_0}{p_0} = \frac{p_{0,2} - p_{0,1}}{p_{0,1}}, \quad \frac{\Delta Sa}{Sa} = \frac{Sa_2 - Sa_1}{Sa_1}, \quad (3.18)$$

where

$$\frac{p_{0,i}}{p_i} = \left(1 + \frac{\gamma_i - 1}{2} M_i^2\right)^{\frac{\gamma_i}{\gamma_i - 1}}, \quad \gamma_i = \frac{c_{p,i}}{c_{v,i}}; \quad i = 1, 2. \quad (3.19)$$

The stream-thrust function is defined as

$$Sa_i = \frac{p_i A}{\dot{m}_i} (1 + \gamma_i M_i^2); \quad i = 1, 2, \quad (3.20)$$

and is commonly used to determine mass-flow rate specific thrust (e.g., Heiser and Pratt 1994).

The results reveal critical injection angles for the experimental conditions investigated. A sign change in the effects of jet injection on velocity and Mach number occurs at  $\theta_{c,1} \simeq 24.5^\circ$ . At an injection angle of  $\theta_{c,2} \simeq 46^\circ$ , the effect of jet injection on stream thrust function changes sign, and at an injection angle of  $\theta_{c,3} \simeq 65.5^\circ$ , the effect of jet injection on total pressure changes sign. A jet inclination of  $\theta_j < \theta_{c,1}$  increases the freestream velocity and Mach number downstream of injection, and the converse is true for  $\theta_j > \theta_{c,1}$ . The total pressure is effectively the recoverable thrust of the system. Total-pressure losses (e.g., in the case of  $\theta_j = 90^\circ$ , a normal jet) would have an adverse effect on a hypothetical scramjet-cycle efficiency, while the converse is true if total pressure is added to the flow. A jet-inclination angle smaller than the third critical angle,  $\theta_{c,3} \simeq 65.5^\circ$ , contributes to the potential recoverable thrust of the flow. Noted here is that the critical angles discussed above are geometry- and flow-dependent. Different configurations or flows would be characterized by different angles that would result from an appropriate analysis.

The jet inclination of  $30^\circ$  that was selected for the current experiments is close to the first critical angle, and smaller than the second and third critical angles, contributing to the reduced disturbance

to the flow that is observed in Fig. 3.12.

Overall, inclined jets disturb the crossflow less than normal jets while adding thrust at sufficiently small inclination angles, but (for equal diameter) do not penetrate as deeply, nor molecularly mix and chemically react as efficiently as normal jets. Conversely, normal jets decrease thrust potential that may not be recovered by combustion and heat-release effects. Accessing crossflow oxidizer with minimal disturbance to the flow, and efficiently mixing and reacting crossflow fluid with jet fluid in practical applications will typically require design trades between jet diameter, strength ( $J$ ), and inclination in simple fuel-injection configurations, such as those considered here.

### 3.7 Conclusions

In summary, the flow field of a chemically reacting TJISCF exhibits a dependence on jet-fluid molar mass, jet diameter, and jet inclination. One may infer that it also depends on cross-flow density (molar mass), even though that parametric dependence was not explored as part of these investigations. Lower- $W_j$ , faster jets have a higher near-field convective velocity, and mix and react farther downstream when compared to higher- $W_j$  jets. For all jet-fluid molar-mass values, the convective velocity approaches that of the freestream within  $\sim 10$  jet diameters. When normalized by the source jet diameter,  $d^*$  (cf. Eq. 3.4), the mixing-delay length exhibits a power-law dependence on jet Reynolds number across the jet-fluid molar mass and jet diameter range explored. Doubling the reactivity of the TJISCF system only slightly reduces the length between jet injection and the location of 0.6 of the maximum chemiluminescence signal, confirming that the observed interval is primarily a mixing-delay length. Jet inclination increases the mixing-delay length and decreases penetration, but decreases disturbances to the crossflow. Inclination effects can be interpreted in terms of a control-volume analysis that reveals flow- and geometry-dependent critical injection angles at which crossflow Mach number and velocity, stream-thrust function, or total pressure can be recovered downstream of injection.

These results have implications in the design of fuel-injection strategies in supersonic combustors. Higher-density gas-phase fuels are anticipated to mix and react further upstream when compared to lower-density fuels, underscoring some of the advantages of large-hydrocarbon fueled scramjets. Increasing the jet temperature has a compound diminishing effect on Reynolds number of a sonic

jet, i.e.,

$$Re = \frac{\rho UL}{\mu} \propto \frac{T^{-1}T^{1/2}}{T^{0.6}} \simeq \frac{1}{T}, \quad (3.21)$$

as sound speed scales with  $\sqrt{T}$ , density inversely with temperature, and viscosity roughly with  $T^{0.6}$ . A decrease in Reynolds number could delay mixing, and this should be taken into account when considering fuel preheating strategies. A balance between mixing efficiency and level of acceptable disturbance to the crossflow will likely dictate injection angles and injection geometry in general.

## Chapter 4

# The evolution variable manifold (EVM) framework

This chapter presents a combustion-modeling framework aimed at efficient simulations of combustion of complex fuels occurring in the distributed-reaction zone (DRZ) regime with autoignition, as encountered in high-speed flows. The framework comprises several elements including an ignition-delay data-driven approach to induction modeling, a Lagrangian convected reactor unit model to describe the small-scale structure of the reaction zone in the DRZ regime, and a chemistry tabulation (manifold) approach for integration in large-eddy-simulations (LES). The proposed integrated framework is referred to as the evolution variable manifold (EVM) approach.

### 4.1 Background and introduction

Multi-species transport in support of detailed chemical-kinetics models for high-speed combustion simulations of complex fuels is beyond computational reach, and will likely remain so for the foreseeable future. As a consequence, both Reynolds-averaged Navier-Stokes (RANS) and LES numerical models of supersonic combustors typically rely on simplified chemical-kinetic mechanisms and the transport of a reduced number of species to model ignition and combustion chemistry. In LES, subgrid-scale closure for the chemical source terms has been modeled in terms of a transported or assumed probability-density function (PDF, Baurle and Girimaji 2003), or an eddy-dissipation concept (EDC, Chakraborty et al. 2000). In the low Mach number approximation, unsteady flamelet

(Pitsch 2000) and flamelet progress-variable approaches (Pierce and Moin 2004) have been used in LES of turbulent combustion with autoignition phenomena. Chemistry-tabulation approaches including flamelet-generated manifold (FGM) methods with complex chemistry and some compressibility corrections have been applied to supersonic combustion (e.g., Sabelnikov et al. 1998, Terrapon et al. 2009, Saghafian et al. 2015) assuming that small-scale reaction-zone structure in a supersonic combustor can be described by laminar-flamelet equations.

It is useful to assess these approaches in the turbulent supersonic hydrocarbon-combustion environment at low supersonic flight Mach numbers. As is known, detailed chemical-kinetic mechanisms do not reliably capture autoignition of hydrocarbons at (initially) low to intermediate temperatures, or at off-stoichiometric conditions (cf. Appendix C). The validity of the laminar-flamelet approximation should also be assessed in the typical turbulent-flow environment anticipated in low supersonic Mach number, high Reynolds number hydrocarbon-fueled scramjet combustors. As discussed below and based on turbulence-chemistry scaling arguments, supersonic combustion of hydrocarbons likely occurs in the distributed reaction-zone (DRZ) regime.

This chapter discusses these issues and proposes a unit-model for the small-scale reaction-zone structure of hydrocarbon combustion in the DRZ regime, based on the Lagrangian balloon-reactor concept introduced by Dimotakis and Hall (1987). This unit-model can be used to generate state-space manifolds (tables) that contain detailed DRZ combustion data as a function of a reduced thermochemical state. Induction and autoignition are treated based on either experimental ignition-delay data-driven models, or on detailed chemical kinetics, in regimes where the latter are expected to be reliable. A LES implementation of the proposed method is demonstrated to capture several important flow features of a complex supersonic reacting flowfield in which autoignition phenomena are important.

## 4.2 Small-scale structure of supersonic combustion

This section identifies two aspects of supersonic hydrocarbon-combustion modeling: autoignition and the small-scale structure of the reacting flow field (Poinsot and Veynante 2005). Supersonic hydrocarbon combustion is typically characterized by intense turbulence that promotes efficient fuel-air dispersion and mixing. Relatively low pre-ignition (induction) temperatures and short residence

times lead to ignition-delay times can be large relative to flow-path timescales, as experimentally confirmed by Gruenig and Mayinger (1999), Micka and Driscoll (2012), and Bateup et al. (2013), for example.

Depending on local ratios of turbulence-to-reaction length and time scales (e.g., Borghi 1984, Peters 1988, 1999), turbulent reacting fluid can (locally) form quasi-laminar flame-sheets, wrinkled or corrugated flame-sheets, thin reaction zones, or distributed reaction zones. As a notional aid, Fig. 4.1 (left) shows a non-premixed hydrocarbon flame at low Reynolds number ( $Re < 10^3$ , Dimotakis 1997). Figure 4.1 (right) shows OH-PLIF in distributed reaction zones of an ethylene jet in a heated supersonic oxygen crossflow (Ben-Yakar 2000), with high Reynolds number. The resolution of the OH-PLIF image on the right is approximately 0.2 mm per pixel, smaller than the flame thickness (Göttgens et al. 1992).

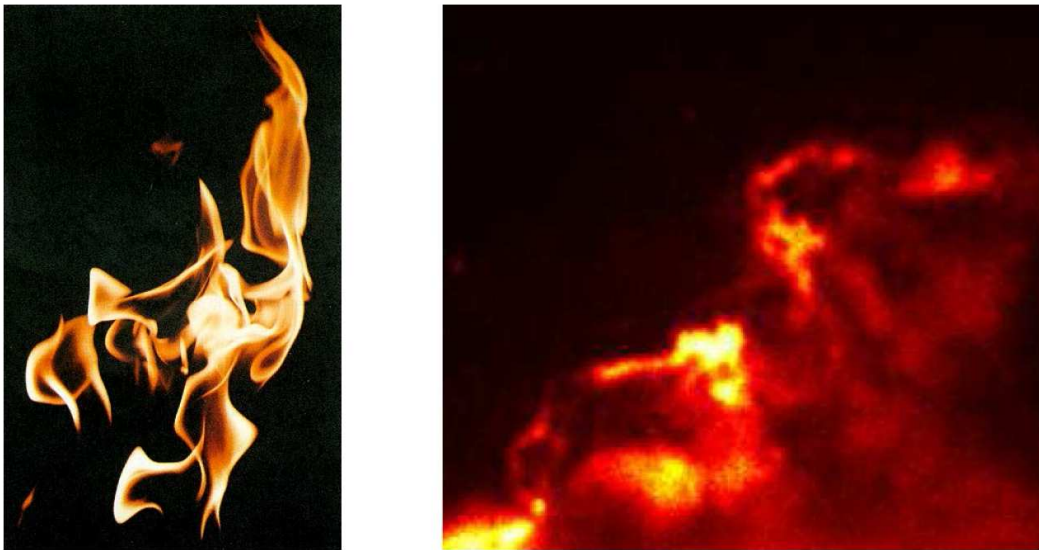


Figure 4.1: Non-premixed hydrocarbon flame (left, Dimotakis 1997, reproduced with permission), and OH-PLIF in a burning ethylene jet in supersonic, heated O<sub>2</sub> crossflow (right, Ben-Yakar 2000, reproduced with permission)

Determining the small-scale structure of low Mach number supersonic and high-subsonic hydrogen- and hydrocarbon-air combustion is challenging. Balakrishnan and Williams (1994) and Ingenito and Bruno (2010) argue that supersonic hydrogen combustion in high Mach number scramjets occurs

in thin flame sheets based on scaling arguments and large-eddy simulations using one-step chemistry. However, arguments based on local strain-rate magnitudes in relevant Reynolds number and Mach number regimes suggest that only a small fraction of chemical-product formation and heat release can occur in such a regime (Egolfopoulos et al. 1996). More recently, Cocks (2011) reaches a similar conclusion and finds that analyses based on one-step chemistry underestimate chemical time scales, suggesting that distributed reactions are present and may dominate, even in kinetically fast supersonic hydrogen-air combustion, as also noted by Gamba and Mungal (2015a) in supersonic jet-in-crossflow hydrogen-air combustion experiments.

Recent combustion experiments of simple hydrocarbon and hydrocarbon-hydrogen blends further support the finding that high-speed combustion of hydrocarbons with sufficiently-high turbulence intensity likely occurs in a distributed reactions regime. Experiments by Zhou et al. (2015) capture the onset of distributed reactions in turbulent high-speed methane-air jet-flames at jet-diameter based Reynolds numbers as low as  $Re_j = 2 \times 10^4$ , consistent with the mixing-transition onset for turbulent jets (Dimotakis 2000). Evidence of thick flames with autoignition in a sonic ethylene-hydrogen jet in a high-subsonic ( $M = 0.62$ ) heated-air crossflow was also noted by Micka and Driscoll (2012).

#### 4.2.1 Autoignition-dominated distributed reaction zone (DRZ) combustion

Intense turbulence generated by fuel-air mixing in supersonic combustors using shear-layer or jet-in-crossflow injection yields Kolmogorov length scales of a few micrometers ( $\mu\text{m}$ ). Kolmogorov-size (and larger) eddies, approximately an order-of-magnitude smaller than the predicted thin reaction-zone thickness of a flame, penetrate the reaction zone and break down local flamelet structures into locally distributed reactions. We note, however, that eddies smaller than  $\sim 50$  times the Kolmogorov scale are in the viscous regime (Dimotakis 2000, Section 3), and those at the Kolmogorov scale do not contain much kinetic energy to ‘stir’ and break down the thin reaction zone of the flame. The disruption of the reaction zone is likely accomplished by more-energetic eddies a few times larger than the Kolmogorov scale.

The onset of distributed reactions at high Karlovitz numbers was observed in numerical simu-

lation (DNS) results by Aspden et al. (2011) and subsequently experimentally observed by Zhou et al. (2015). In the DRZ regime, rapid turbulent mixing at scales smaller than thin reaction zones eliminates the local steep temperature and species gradients encountered in flamelet regimes. This leads to a departure from diffusion-dominated flamelet behavior.

Formally, if the local reaction-zone Karlovitz number, i.e., the square of the ratio of the reaction-zone thickness  $\delta_R$  to the Kolmogorov length-scale  $\lambda_K$ ,

$$Ka_R = \left( \frac{\delta_R}{\lambda_K} \right)^2, \quad (4.1)$$

is larger than  $10^2$ , i.e., for  $\delta_R/\lambda_K > 10$ , combustion can be assumed to occur in the DRZ regime (Zhou et al. 2015).

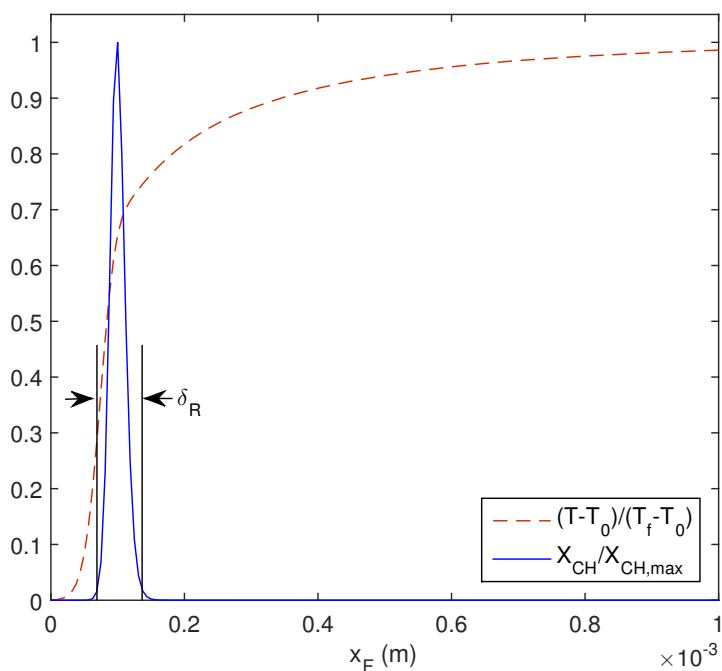


Figure 4.2: Premixed ethylene-air flame structure at combustor inlet conditions anticipated in a  $M_\infty = 6$  scramjet

We consider a hypothetical  $M_\infty = 6$  ethylene-burning scramjet at an altitude of 65,000 ft. with a flight-to-combustor-inlet Mach-number ratio of 3.5, for example. The combustor inlet conditions for such a vehicle are  $T \simeq 1150$  K,  $p \simeq 4$  bar (Heiser and Pratt 1994). The one-dimensional flame structure of a premixed, stoichiometric ethylene-air flame at those conditions was determined from a one-dimensional flame simulation using the UCSD (2012) mechanism, and the Cantera software package (Goodwin 2005). The reaction-zone thickness is on the order of  $\delta_R \simeq 10^{-4}$  m = 100  $\mu$ m, as shown in Fig. 4.2, using CH concentration as a reaction-zone marker (Zhou et al. 2015).  $x_F$  is the flame-normal coordinate.

Assuming Kolmogorov-turbulence scaling, the local Kolmogorov length scales with the local (integral) turbulence length-scale,  $l_0$ , and the turbulence Reynolds number,  $Re'$ , based on the fluctuating (rms) component of velocity  $u'$ ,

$$\lambda_K \simeq l_0 (Re')^{-3/4} , \quad (4.2)$$

where

$$Re' \simeq \frac{u' l_0}{\nu} . \quad (4.3)$$

Values of  $Re'$  are bounded if based on unburnt and burnt-fluid kinematic viscosities, with unburnt-fluid Reynolds numbers  $Re'_u$  larger than burnt-fluid Reynolds number  $Re'_b$ .

The local reaction-zone Karlovitz number can then be expressed as

$$Ka_R \simeq \left( \frac{\delta_R}{l_0} \right)^2 (Re')^{3/2} , \quad (4.4)$$

where the upper and lower bounding values of  $Ka_R$  are dictated, in part, by the local kinematic viscosity in burnt and unburnt fluid mixtures. Supersonic shear-layer turbulence intensity,  $u'$ , is typically 0.15-0.23 of  $\Delta U = U_1 - U_2$ , the high-speed ( $U_1$ ) to low-speed ( $U_2$ ) velocity difference across the shear layer (e.g., Batt 1977, Browand and Latigo 1979, Goebel and Dutton 1991). The

integral turbulence length scale,  $l_0$ , can be approximated by the local shear-layer thickness.<sup>1</sup>

Experimentally determined normal jet-in-crossflow turbulence intensity is between 0.05 and 0.15 of the freestream (crossflow) velocity,  $U_1$ , in the vicinity of the jet (for  $x/d_j < 10$ ; e.g., Santiago and Dutton 1997), while the integral turbulence length scale in the near field can be approximated by the jet diameter,  $l_0 \sim d_j$ . The range of local turbulence Reynolds numbers in burnt and unburnt fluid (using bounding values of burnt and unburnt density and viscosity), based on  $u'$  and the jet diameter for a sonic jet in a  $M_\infty = 1.7$  crossflow, or the local transverse extent of the shear-layer with high-speed side  $M_\infty = 1.7$  and a velocity ratio  $U_1/U_2 = 0.25$ , is then

$$\begin{aligned} 2 \times 10^4 \leq Re'_u \leq 10^5 \\ 5 \times 10^3 \leq Re'_b \leq 2.5 \times 10^4, \end{aligned} \tag{4.5}$$

corresponding to flow above the mixing transition (Dimotakis 2000). Assuming Kolmogorov scaling, the Kolmogorov length scale within the jet-in-crossflow and shear-layer regions is then in the range,

$$3 \mu\text{m} < \lambda_K < 25 \mu\text{m}, \tag{4.6}$$

with the smallest eddies in the unburnt fluid. Corresponding reaction-zone Karlovitz numbers are then  $30 \leq Ka_R \leq 1000$ . Table 4.1 lists the expected range of turbulence intensity, turbulence Reynolds number, and Karlovitz number in a  $M_\infty = 6$  ethylene-fueled scramjet described above, for shear-layer and normal jet-in-crossflow flows. We note that the bounding values of  $\lambda_K$  and  $Ka_R$  are extrema, and the bulk of the flow is expected to have intermediate values of  $\lambda_K$  and  $Ka_R$ .

Table 4.1: Turbulence-chemistry scaling in an ethylene-fueled  $M_\infty = 6$  scramjet

Injection	$U_1$ m/s	$U_2$ m/s	$u'$ m/s	$Re'$	$Ka_R$
Shear-layer	$1.1 \times 10^3$	$3 \times 10^2$	120 to 200	$5 \times 10^3$ to $10^5$	80 to 800
Jet-in-crossflow	$1.1 \times 10^3$		50 to 150	$5 \times 10^3$ to $5 \times 10^4$	20 to 1000

<sup>1</sup>The shear-layer turbulence integral length-scale is estimated using the expression for incompressible shear-layer growth rate, with the growth-rate coefficient  $C_\delta$  halved to account for compressibility and heat-release effects (Dimotakis 1991).

This confirms that distributed-reaction regimes are expected in low Mach number supersonic hydrocarbon combustion with either shear-layer or normal jet-in-crossflow fuel injection.

Here, hydrogen and ethylene ( $\text{C}_2\text{H}_4$ ) are considered as fuels, by way of example. Ethylene and ethylene-containing blends are commonly used in ground tests of supersonic and high-speed combustion to provide validation data for simulations. In flight vehicles, higher-hydrocarbon fuels would be used that would be thermally cracked. Thermal cracking of liquid fuels, including kerosene, into  $\text{C}_1 - \text{C}_3$  gas-phase fuels is used endothermically for engine cooling and thermal balance, also reducing ignition delays by introducing reactive radical species. Ethylene is produced as the principal component of thermally cracked *n*-dodecane, for example, which is a commonly used kerosene surrogate (Nakaya et al. 2015). As a result and to facilitate validation, the EVM simulation framework is initially intended for modeling combustion of ethylene, ethylene blends, or hydrogen (cf. Chapter 5). However, the framework can be extended to larger gas-phase hydrocarbons.

#### 4.2.2 Unit model for DRZ combustion

The small-scale structure of a reacting flow in the distributed reaction-zone (DRZ) regime is described as a collection of convected Lagrangian unsteady well-stirred reactors (e.g., Dimotakis and Hall 1987) that entrain and mix surrounding fluid as they evolve through induction to ignition and combustion, and whose entrainment/mixing and reaction timescales are comparable.

In an Eulerian frame, the general form of the  $\alpha$ -species transport equation (e.g., Dimotakis 2005) is

$$\frac{\partial \rho Y_\alpha}{\partial t} + \frac{\partial}{\partial \mathbf{x}} \cdot [(\mathbf{u} + \mathbf{v}_\alpha) \rho Y_\alpha] = \dot{\omega}_\alpha , \quad (4.7)$$

where  $Y_\alpha$  is the  $\alpha$ -species mass fraction,  $\mathbf{v}_\alpha$  is the  $\alpha$ -species diffusion velocity in the  $\mathbf{u}$  frame, and  $\dot{\omega}_\alpha$  is the  $\alpha$ -species production rate.  $\alpha = 1, 2, 3, \dots, N_\alpha$ , where  $N_\alpha$  is the number of species. Velocity can be further partitioned into  $\mathbf{u} = \bar{\mathbf{u}} + \mathbf{u}'_{\text{R}}$ , where  $\bar{\mathbf{u}}$  is the bulk velocity and  $\mathbf{u}'_{\text{R}}$  are small-scale velocity fluctuations that dominate transport in intense turbulence (as shown experimentally by Barlow et al. 2005), i.e.,  $|\mathbf{u}'_{\text{R}}| \gg |\mathbf{v}_\alpha|$ . Eq. 4.7 can then be rewritten as,

$$\frac{\partial \rho Y_\alpha}{\partial t} + \frac{\partial}{\partial \mathbf{x}} \cdot (\rho Y_\alpha \bar{\mathbf{u}}) + \frac{\partial}{\partial \mathbf{x}} \cdot (\rho Y_\alpha \mathbf{u}'_R) = \dot{\omega}_\alpha . \quad (4.8)$$

The velocity resolved in a LES is the bulk velocity,  $\bar{\mathbf{u}}$ , while small-scale velocity fluctuations,  $\mathbf{u}'_R$ , correspond to subgrid-scale (SGS) velocity fluctuations that must be modeled.

We consider a Lagrangian (convected) material element with volume  $V_R$ , surface area  $\partial V_R$ , and mass  $m_R$ , depicted in Fig. 4.3.

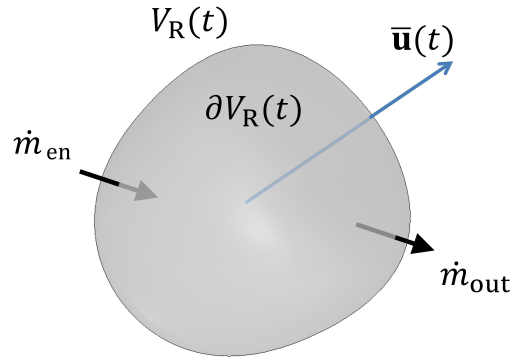


Figure 4.3: Convected material element

The material element is convected at the bulk fluid velocity,  $\bar{\mathbf{u}}$ , while the small-scale velocity fluctuations,  $\mathbf{u}'_R$ , are assumed to contribute to the mass flux entrained into ( $\dot{m}_{\text{en}}$ ) and transported out ( $\dot{m}_{\text{out}}$ ) of the reactor. The species conservation equation in the convected frame of such a material element is then

$$\frac{d\rho Y_\alpha V_R}{dt} = \dot{m}_{\text{en}} Y_{\alpha,\text{en}} - \dot{m}_{\text{out}} Y_{\alpha,\text{out}} + V_R \dot{\omega}_\alpha , \quad (4.9)$$

where  $Y_{\alpha,\text{en}}$  and  $Y_{\alpha,\text{out}}$  are the  $\alpha$ -species mass fractions of the fluid entering and exiting the control volume, respectively.  $Y_{\alpha,\text{out}} = Y_\alpha$  if a homogeneous material element is assumed. Expanding the left-hand side of Eq. 4.9, and assuming a constant-mass material element, i.e.,  $\rho V_R = \text{const.}$ , we obtain,

$$\frac{d\rho Y_\alpha V_R}{dt} = Y_\alpha \frac{d\rho V_R}{dt} + \rho V_R \frac{dY_\alpha}{dt} = \rho V_R \frac{dY_\alpha}{dt}. \quad (4.10)$$

Noting that, for a constant-mass material element,  $\dot{m}_{\text{en}} = \dot{m}_{\text{out}} = \dot{m}$ , we rewrite Eq. 4.9,

$$\frac{dY_\alpha}{dt} = \frac{\dot{m}}{\rho V_R} (Y_{\alpha,\text{en}} - Y_\alpha) + \frac{\dot{\omega}_\alpha}{\rho}. \quad (4.11)$$

We then define an entrainment parameter  $\chi$  that describes the normalized mass flux through the material element caused by small-scale velocity fluctuations,

$$\chi = \frac{\dot{m}}{\rho V_R}, \quad (4.12)$$

and rewrite Eq. 4.11 as an unsteady, well-stirred reactor,

$$\frac{dY_\alpha}{dt} = \chi(Y_{\alpha,\text{en}} - Y_\alpha) + \dot{\omega}_{Y_\alpha}([Y_\alpha], \Theta), \quad (4.13)$$

where the chemical-source term is rewritten as  $\dot{\omega}_{Y_\alpha} = \dot{\omega}_\alpha \rho^{-1}$ . The chemical source term for the  $\alpha$ -species is a function of the overall composition vector,  $[Y_\alpha]$ ,<sup>2</sup> as well as the thermodynamic state of the fluid element,  $\Theta$ . The thermodynamic state can be defined by the internal specific energy,  $e$ , here defined with respect to an ambient state ( $T_{\text{ref}} = 298.15$  K), and density,  $\rho$ , or, alternatively, the specific enthalpy,  $h$ , and pressure,  $p$ , i.e.,

$$\Theta = [e, \rho] \quad \text{or} \quad \Theta = [h, p]. \quad (4.14)$$

At the smallest scales, turbulent combustion in the DRZ regime is then modeled as a Lagrangian convected unsteady well-stirred reactor (WSR), or ‘balloon’ reactor,<sup>3</sup> that is entraining surrounding fluid with composition  $Y_{\alpha,\text{en}}$  at a rate  $\chi$ . The energy-conservation equation (e.g., Landau and Lifshitz 1989) in the convected frame of the material element is

---

<sup>2</sup>Square brackets [...] or bold type  $\mathbf{x}$  denote a vector. For example,  $[Y_\alpha]$  is a vector with  $N_\alpha$  elements.

<sup>3</sup>The terms ‘Lagrangian WSR’, ‘convected WSR’, and ‘balloon reactor’ are used interchangeably in this chapter.

$$\frac{d}{dt}(\rho e V_R) = \dot{m}_{\text{en}} h_{\text{en}} - \dot{m}_{\text{out}} h_{\text{out}} - p \frac{dV_R}{dt}, \quad (4.15)$$

where  $h_{\text{en}}$  and  $h_{\text{out}}$  denote the enthalpy of the fluid entrained into or exiting the reactor, respectively. Using the same assumptions applied to Eq. 4.9, i.e.,  $\dot{m}_{\text{en}} = \dot{m}_{\text{out}} = \dot{m}$ , and  $h_{\text{out}} = h$ , we obtain

$$\frac{de}{dt} = \chi(h_{\text{en}} - h) - \underbrace{\frac{p}{\rho} \left( \frac{1}{V_R} \frac{dV_R}{dt} \right)}_{\text{dilatation}}, \quad (4.16)$$

with a dilatation term, as indicated, that can be rewritten in terms of density, i.e.,

$$\frac{1}{V_R} \frac{dV_R}{dt} = -\frac{1}{\rho} \frac{d\rho}{dt}. \quad (4.17)$$

Noting that  $h = e + p \rho^{-1}$ , Eq. 4.16 can be written as,

$$\frac{dh}{dt} = \chi(h_{\text{en}} - h) + \frac{1}{\rho} \frac{dp}{dt}. \quad (4.18)$$

The pressure of the reactor,  $p(t)$ , entrained-fluid composition vector,  $[Y_{\alpha, \text{en}}]$ , entrained-fluid enthalpy,  $h_{\text{en}}$ , or energy,  $e_{\text{en}}$ , and turbulent entrainment rate,  $\chi$ , are functions of the fluid and flow surrounding the reactor. These quantities are either calculated or assumed to be model inputs. The entrainment rate,  $\chi$ , can be related to turbulence intensity by estimating the magnitude of the small-scale turbulent fluctuations,  $u'_R = |\mathbf{u}'_R|$ , that contribute to mass flux through the reactor,

$$\chi = \frac{\dot{m}}{\rho V_R} \simeq \frac{\partial V_R}{V_R} \frac{u'_R}{2} = \frac{G}{\Delta_R} \frac{u'_R}{2}, \quad (4.19)$$

where  $\Delta_R \simeq V_R (\partial V_R)^{-1}$  is the characteristic reactor dimension, and  $G$  is a geometrical factor relating surface area to volume (3 for a sphere, 6 for a cube, etc.). The factor of 2 in the denominator arises if one assumes that roughly half the velocity fluctuations contribute to mass flux into the control volume, and half to mass flux out of the control volume. The magnitude of the small-scale fluctuations,  $u'_R$ , that contribute to turbulent transport can be approximately related to the kinetic

energy,  $ke_R$ , contained in those scales as

$$u'_R = \sqrt{\frac{2}{3} ke_R}. \quad (4.20)$$

Recall that  $u'_R$  does not represent the rms value of the turbulent fluctuations, rather the magnitude of the small-scale (reactor-scale) velocity fluctuations that are primarily responsible for turbulent transport at the reactor scale, which would correspond to the subgrid-scale in a LES. The characteristic reactor length scale,  $\Delta_R$ , can be approximated as on the order of the (thickened) reaction-zone thickness. Zhou et al. (2015) proposed a reaction-zone thickness threshold of  $4 \times \delta_R$ , where  $\delta_R$  is the laminar-flame reaction-zone thickness, for combustion to be categorized as in the DRZ regime. The characteristic reactor length scale can then be approximated as  $\Delta_R \simeq 4 \times \delta_R$ .

The proposed framework and model is not intended to capture combustion in quasi-laminar flames for which a flamelet-based approach may be more appropriate; it targets the DRZ regime in which reactants (partially) mix, become (nearly) homogeneous at small scales, and react, and which is anticipated in the high-speed/supersonic regimes of interest here, for example.

### 4.2.3 The effects of $\chi$

Increasing  $\chi$  increases the overall reactivity of a Lagrangian WSR described above. Figure 4.4 plots the product mass-fraction source term,  $\dot{\omega}_{Y_P}$ ,

$$\dot{\omega}_{Y_P} = \dot{\omega}_{Y_{CO_2}} + \dot{\omega}_{Y_{CO}} + \dot{\omega}_{Y_{H_2O}} + \dot{\omega}_{Y_{H_2}}, \quad (4.21)$$

against the normalized product mass fraction,  $Y_P/Y_{P,eq}$ , where

$$Y_P = Y_{CO} + Y_{CO_2} + Y_{H_2O} + Y_{H_2}, \quad (4.22)$$

and  $Y_{P,eq}$  is the value of  $Y_P$  at thermodynamic equilibrium, in a constant-enthalpy and pressure WSR.

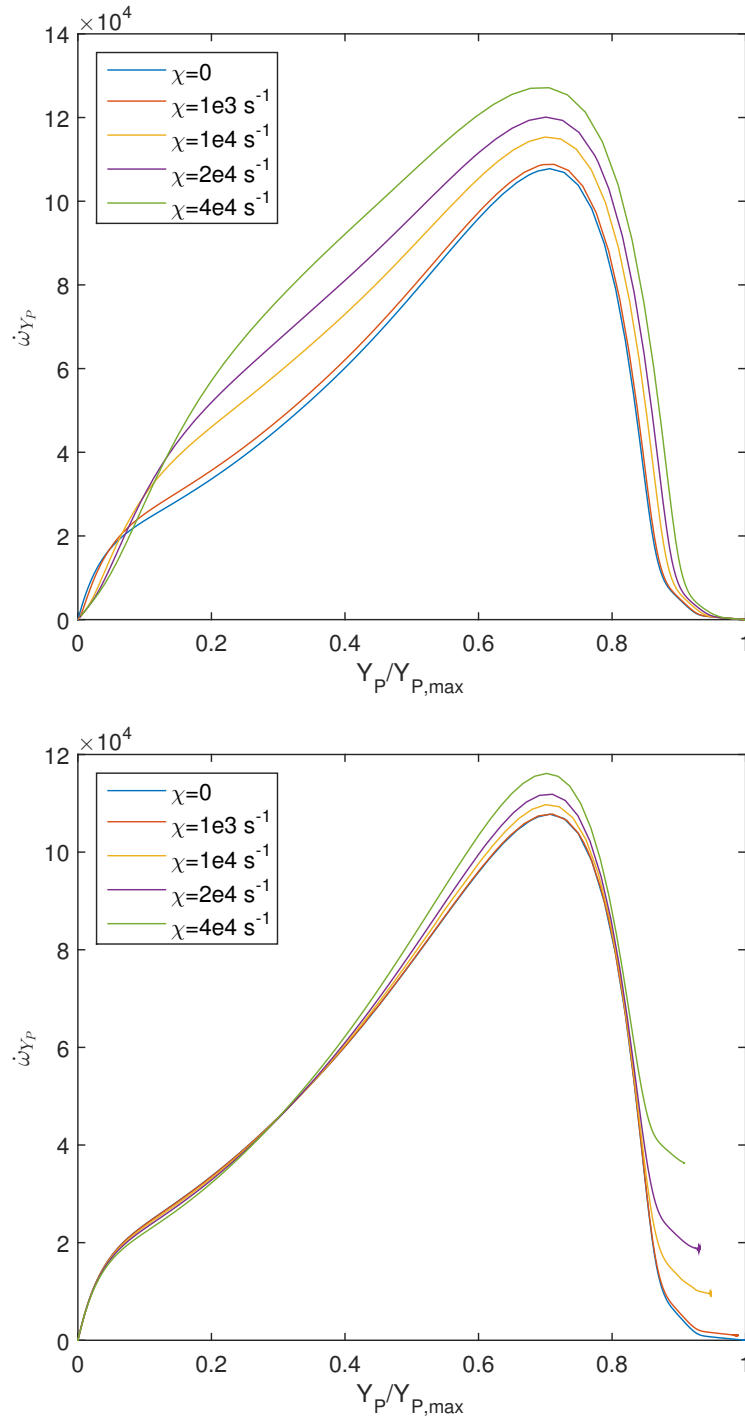


Figure 4.4: Product mass-fraction source term for various values of  $\chi$ , for a WSR entraining burnt fluid (top), and unburnt fluid (bottom)

The reactor entrains stoichiometry-, enthalpy-, and pressure-matched fluid (i.e.,  $h_{\text{en}} = h(t = 0)$ ,  $p = \text{const.}$ ) with various values of  $\chi$ , for a mixture of stoichiometric ethylene-air. Chemical kinetics are determined using the UCSD (2012) mechanism. Figure 4.4 (top) shows the results of a reactor entraining initial reactor fluid at thermochemical equilibrium at constant  $[h, p]$  (burnt fluid), i.e.,

$$Y_{\alpha, \text{en}} = (Y_{\alpha, t=0})_{\text{eq}, [h, p]} , \quad (4.23)$$

while Fig. 4.4 (bottom) shows the results of a reactor entraining unburnt fluid, i.e.,

$$Y_{\alpha, \text{en}} = Y_{\alpha}(t = 0) . \quad (4.24)$$

The extent of combustion completion of the entrained fluid affects the reaction evolution in the reactor. Entraining combustion products (cf. Fig. 4.4, top) increases the aggregate source term of the combustion products,  $\dot{\omega}_{Y_P}$ , relative to a reactor entraining unburnt fluid (Fig. 4.4, bottom). In addition to increasing the reactivity of an already-reacting fluid element, entraining burnt fluid into a reactor with initial (unburnt) conditions below those necessary for autoignition provides a mechanism for autoignition.

### 4.3 Induction modeling in autoignition-dominated flows

Autoignition is important in supersonic and high-speed reacting flows. Efficient and reliable ignition modeling in these flows is challenged by the complexity of existing ignition models, and by their limited reliability in low-temperature or off-stoichiometric conditions anticipated in certain regions of supersonic combustors.

Detailed chemical-kinetic models that track radical-pool evolution during induction leading to autoignition offer adequate ignition-delay predictions in a limited range of conditions. The computational expense of detailed chemical-kinetics in simulations of turbulent high-speed reacting flows places such simulations beyond present reach, especially for reactions involving complex hydrocar-

bons that require transporting a large number of species. Moreover, detailed chemical-kinetic mechanisms and associated reduced/skeletal mechanisms do not agree with experimental ignition-delay data at low temperatures or off-stoichiometric conditions.

An experimental data driven approach to induction modeling is described in this section. The proposed approach is computationally tractable, requiring the transport of only a few variables. In addition, it offers improved reliability relative to detailed chemical-kinetic approaches at low temperatures or off-stoichiometric conditions.

### 4.3.1 Chemical-kinetic mechanisms for induction modeling

Detailed chemical-kinetic mechanisms typically describe the evolution of tens to hundreds of species (reaction intermediates) using Arrhenius-like equations, with parameters that are fit to match experimental or theoretical data. Hydrocarbon oxidation is strongly hierarchical. Complex hydrocarbons ( $C_4$  and larger) break down into smaller hydrocarbons ( $C_1$ ,  $C_2$ , and  $C_3$ ) along various pathways to product-formation and heat-release (e.g., Law 2010). Mechanisms for larger hydrocarbons contain sub-mechanisms for the oxidation of smaller ( $C_1$ - $C_3$ ) hydrocarbons. The reliability of large-hydrocarbon chemical-kinetic models is then also limited by that of its sub-mechanisms. The reliability of autoignition-dominated complex-hydrocarbon combustion simulations depends on the reliability of the chemical-kinetic sub-mechanisms for small hydrocarbons, such as hydrogen, methane, ethane, acetylene, and ethylene, at the simulated conditions. Ignition-delay times predicted by chemical-kinetic models for  $C_1$ - $C_3$  hydrocarbons are reliable at intermediate temperatures ( $1200 \text{ K} \leq T \leq 1600 \text{ K}$ ) and near-stoichiometric conditions, but are less reliable at lower temperatures and off-stoichiometric conditions.

Appendix C assesses the predictive capability of a selection of state-of-the-art and heritage detailed chemical-kinetic mechanisms (Table 4.2) for induction modeling, based on experimental shock-tube ethylene ignition-delay times (Table 4.3). The list of mechanisms in Table 4.2 is not exhaustive, but is representative of detailed chemical-kinetic mechanisms developed over the past two decades for smaller hydrocarbons.

Table 4.2: Detailed chemical-kinetic mechanisms

Name (year) [abbr.]	Species ( $N_\alpha$ )	Reactions	Intended use
Ranzi C <sub>1</sub> -C <sub>3</sub> (2012), RNZ	98	1863	C <sub>1</sub> -C <sub>3</sub> oxidation
UCSD (2012), SD	50	244	C <sub>n</sub> H <sub>m</sub> oxidation
JetSurF 2.0 (2010), JET	348	2163	C <sub>n</sub> H <sub>m</sub> oxidation
USC Mech II (2007), USC	111	784	H <sub>2</sub> /CO/C <sub>1</sub> -C <sub>4</sub> oxidation
LLNL C <sub>1</sub> -C <sub>3</sub> (1998), LLNL	155	689	C <sub>1</sub> -C <sub>3</sub> oxidation
GRI-Mech 3.0 (2000), GRI	53	325	Natural gas combustion
Davis-C3 (1999), DC3	71	469	Propene pyrolysis and oxidation
Laskin, Wang, Law (2000), LWL	94	614	1,3-butadiene oxidation
Dagaut (1990), DAG	71	412	C <sub>2</sub> H <sub>4</sub> pyrolysis and oxydation

The experimental shock-tube ignition-delay data ( $N_i$  individual ignition experiments) in Table 4.3 is for ethylene ignition. Similar ignition-delay data are available for a wide range of practical and research fuels across a large range of thermodynamic conditions, and stoichiometry,  $\phi$ .

Overall, the mean variance between ignition-delay times predicted by recent, well-resolved chemical-kinetic mechanisms and experimental ignition-delay data is on the order of 50-100%, and considerably higher at low temperatures or at off-stoichiometric conditions, or both (for more detail, see Appendix C). This motivates the development of the data-driven induction-evolution model, described in the following section.

Table 4.3: Experimental (shock-tube) ethylene ignition-delay data sets

Reference (year)	$N_i$	$T(K)$	$p$ (bar)	$\phi$	Ignition diagnostic
Kopp et al. (2014)	107	[1000, 1400]	[1, 25]	[0.3, 2.0]	$\Delta p$ , OH*
Saxena et al. (2011)	148	[1050, 1850]	[1.9, 20.2]	[1, 3]	Visible, OH*, CH*
Penyazkov et al. (2009)	42	[1100, 1500]	[6, 16]	[0.5, 2.0]	CH*, OH*, C <sub>2</sub>
Kalitan et al. (2005)	79	[1100, 1750]	[1, 3]	[0.5, 1.0]	OH*
Horning (2001)	27	[1250, 1600]	[1, 4]	1.0	CH*
Colket and Spadaccini (2001)	27	[1100, 1400]	[5, 8]	[0.5, 1]	OH*
Jachimowski (1977)	25	[1800, 2400]	[1.1, 1.7]	[0.5, 1.5]	CO, CO <sub>2</sub>
Hidaka et al. (1974)	77	[1400, 2100]	[2, 5]	[1.0, 3.0]	CH*
Baker and Skinner (1972)	150	[1050, 1900]	[3, 12]	[0.125, 2.0]	OH*
Suzuki et al. (1973)	124	[850, 1300]	[1.0, 3.2]	[0.5, 2.5]	OH absorption
Drummond (1968)	49	[1000, 1700]	[1.0, 2.2]	[1.0, 2.0]	OH*
Gay et al. (1967)	57	[1400, 2300]	[0.2, 0.4]	[1.0, 2.0]	CH*
Homer and Kistiakowsky (1967)	17	[1500, 2300]	[0.3, 0.8]	[0.5, 1.5]	CO, CO <sub>2</sub>

### 4.3.2 Induction evolution based on characteristic ignition-delay time

The overall rate at which a reacting, homogeneous fluid element progresses towards ignition can be approximated as a function of the instantaneous characteristic ignition delay,  $t_{d,c}$ , of the fluid element that integrates to an arbitrary value,  $\kappa$ , at the time of ignition (Williams 1970), i.e.,

$$\int_0^t \zeta_i(t_{d,c}) dt = \tau_i, 0 < \tau_i < \kappa, \quad (4.25)$$

where  $\tau_i$  is an induction-evolution variable (or progress variable), and  $\kappa$  is the value of  $\tau_i$  at ignition. A linear expression for the induction-evolution rate was originally proposed by Williams (1970, 1985),

$$\zeta_i = \frac{1}{t_{d,c}}, \quad (4.26)$$

and has been used to model induction in internal-combustion engines (e.g., Da Cruz 2004, Colin et al. 2005). This linear model, however, does not capture the exponential growth of the radical pool with time. We define the radical pool for ethylene ignition, for example, as the sum of the mass fractions of radicals that contribute to the ignition process, including hydroperoxyl, methyl, vinyl, aldehyde, ethyl, and acetyl (Xu and Konnov 2012), i.e.,

$$Y_{\text{rad}} = Y_{\text{HO}_2} + Y_{\text{CH}_3} + Y_{\text{C}_2\text{H}_3} + Y_{\text{HCO}} + Y_{\text{C}_2\text{H}_5} + Y_{\text{CH}_3\text{CO}}. \quad (4.27)$$

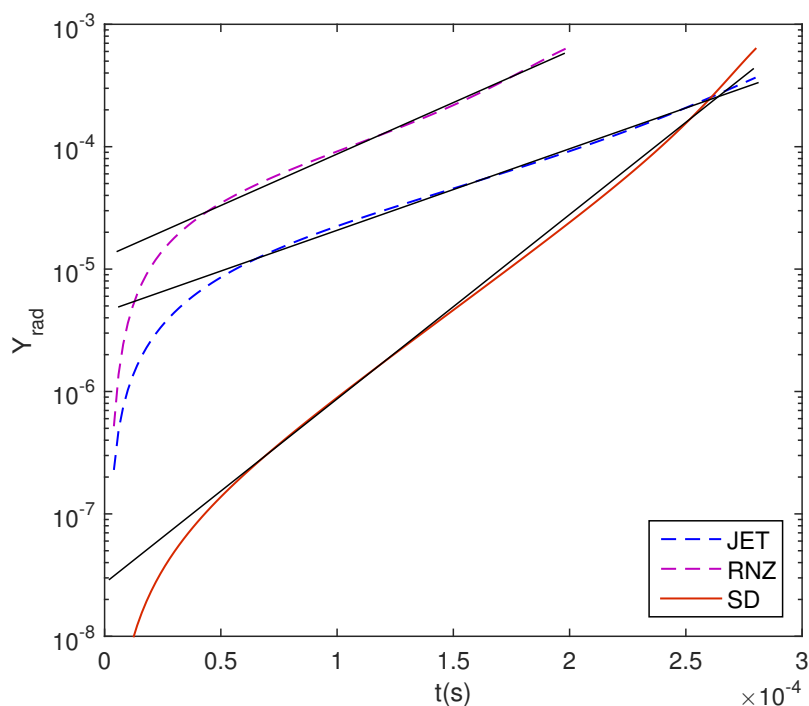


Figure 4.5: Radical-pool concentration-evolution predictions using detailed chemical kinetics

Figure 4.5 plots  $Y_{\text{rad}}$  as predicted by the RNZ, JET, and SD chemical-kinetic mechanisms (cf. Table 4.2) for stoichiometric ethylene-air ignition at atmospheric pressure and an initial temperature of

1200 K, and illustrates the exponential evolution of the radical pool during induction. The radical-pool dynamic range is uncertain. As can be seen in Fig. 4.5, the radical-pool dynamic-range varies between (approximately) two and four decades. Further experimental work would be useful to reduce uncertainty in the dynamic range of the radical-pool concentration during induction.

Differences between linear and exponential growth rates are anticipated to be important if mixing and chemical timescales are comparable. An empirical expression for the overall induction-evolution rate is proposed, tailored to capture the exponential radical-pool growth, i.e.,

$$\zeta_i(\tau_i, t_{d,c}, \kappa, \tau_{i,0}) = \log\left(\frac{\kappa}{\tau_{i,0}}\right) \tau_i \left(\frac{1}{t_{d,c}}\right), \quad (4.28)$$

where  $\tau_{i,0}$  is the induction-evolution variable background value, and  $\kappa/\tau_{i,0}$  is the radical-pool concentration dynamic range during induction. Figure 4.6 plots the evolution of the ethylene-air ignition radical-pool predicted by the UCSD mechanism normalized by the radical pool at ignition,  $Y_{\text{rad,d}}$  (Eq. 4.27), i.e.,

$$\hat{Y}_{\text{rad}} = \frac{Y_{\text{rad}}}{Y_{\text{rad,d}}}. \quad (4.29)$$

The radical-pool evolution predicted by the UCSD mechanism is captured better by the exponential-growth model for  $\tau_i$ , with  $\kappa=1$ , and  $\kappa/\tau_{i,0} = 10^4$ , relative to the linear-growth model that over-predicts the value of  $\tau_i$  throughout most of the induction period (cf. Fig. 4.6).

The characteristic ignition delay,  $t_{d,c}$ , can be estimated *a priori* based on detailed chemical-kinetic simulations using constant volume, or constant-pressure (depending on the application) homogeneous reactors. Alternately, the characteristic ignition delay can be extracted from experimental data. As noted above and as is well-known, using detailed chemical kinetics to determine ignition-delay for hydrocarbons leads to errors at low temperature or off-stoichiometric conditions. A model based on experimental data can offer improved reliability at low temperatures and off-stoichiometric conditions. However, such data are typically not uniformly distributed across their parameter values, may include outliers, may not be available for the regime of interest, and assembling a suitable data set requires a suitable objective methodology.

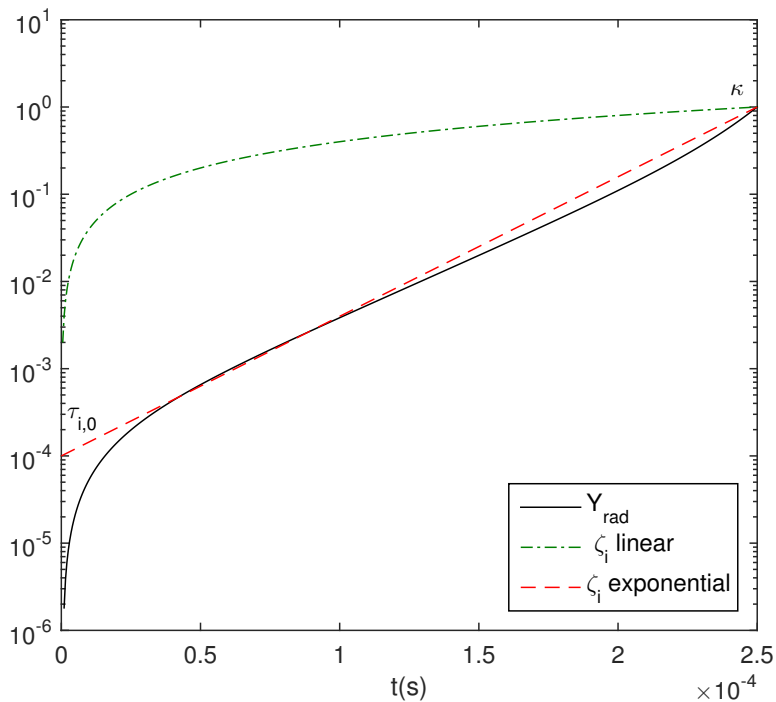


Figure 4.6: Ethylene ignition radical-pool growth (UCSD mechanism)

### 4.3.3 Induction-evolution modeling based on shock-tube data

An exponential-growth function for the induction-evolution variable  $\zeta_i$  can be expressed in terms of an algebraic expression for the characteristic ignition delay, based on suitable experimental ignition-delay data. The principal difficulty lies in collapsing a large, sparse, non-uniform experimental dataset into a tractable expression for  $1/t_{d,c}$  (cf. Eq. 4.28). The proposed approach is to express  $1/t_{d,c}$  in a formulation that captures the dependence of the characteristic ignition-delay on mixture temperature, pressure, and composition. The dependence is well captured by an expression that modifies the Arrhenius form by including a pressure-dependence of the activation energy observed by Kalitan et al. (2005), and a power-law pressure, temperature, fuel, and oxidizer mass-fraction dependence. The expression employed is of the form,

$$\frac{1}{t_{d,c}} = \zeta_0 \theta^a \pi^b \exp\left(\frac{-\beta(1 + \eta\pi)}{\theta}\right) Y_{C_2H_4}^c Y_{O_2}^d, \quad (4.30)$$

in terms of a scaled temperature,  $\theta = T/1000$  K, and pressure,  $\pi = p/1$  bar. The general form of the expression for reciprocal characteristic ignition-delay time was adapted from a modified Arrhenius form with temperature and pressure dependence (e.g., Saxena et al. 2011), with an additional pressure dependence in the exponential to account for the pressure dependence of the activation energy observed by Horning (2001). The seven fit parameters,  $[\zeta_0, a, b, \beta, \eta, c, d]$ , are determined from the experimental data using an iterative fitting and filtering process.

Outliers within the set of  $N_i$  experimental ignition-delay data-points,  $t_{d,n}, n = 1, 2, \dots, N_i$ , are identified and removed by iteratively fitting the reciprocal of the experimental ignition-delay dataset,  $1/t_{d,n}$ , to Eq. 4.30 in a logarithmic least-squares sense, calculating the residual of each of the  $N_i$  data points, i.e.,

$$r_n = \frac{t_{d,c} - t_{d,n}}{t_{d,n}}, \quad n \leq (N_i - k), \quad (4.31)$$

where  $k$  is the iteration number, removing the point with the largest (absolute value) residual, and repeating the process on the remaining  $N_i - k$  datapoints until the maximum residual falls below some threshold  $r_{\max}$ ,

$$r_{k,\max} = [\max(r_n)]_k < r_{\max}, \quad (4.32)$$

or until it becomes evident that the filtering process is no longer rejecting outliers (cf. Fig. 4.7).

As an example, this process is applied to the  $N_i \simeq 950$  ethylene-ignition experiments listed in Table 4.3. The data are sparse in certain regimes (off-stoichiometric composition, relatively high or low temperatures and pressures) and dense in others (stoichiometric composition, intermediate temperatures and pressures). The dataset comprises experimental data recorded over many years, on different experimental setups, whose self-consistency and consistency relative to other data is not well known *a priori*.

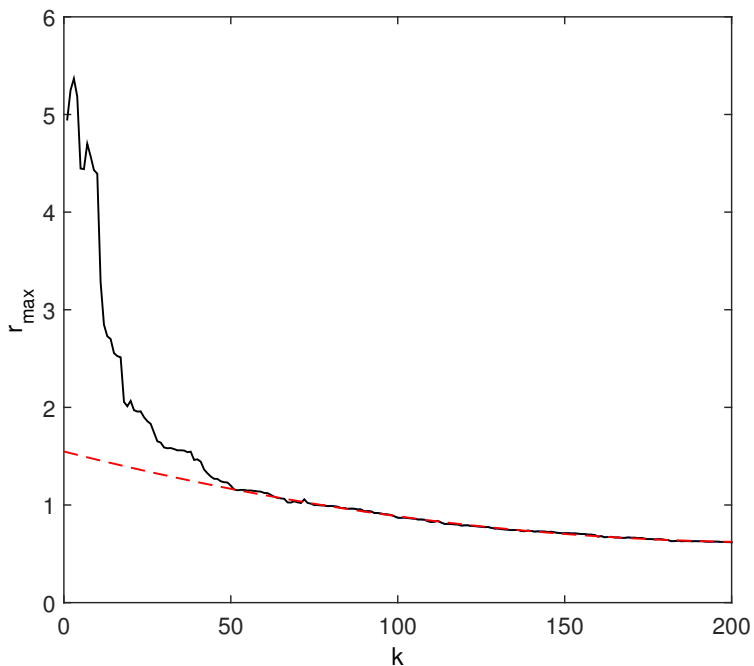


Figure 4.7: Decrease in maximum residual with iteration number  $k$  (solid black). The  $k$ -value cutoff is selected when the residual decay approaches a smooth curve (dashed red).

While removing data responsible for the largest variance will always decrease residuals, plotting  $r_{k,\max}$  versus iteration number  $k$  (Fig. 4.7) shows that only 10-20 out of 950, or so, points ( $\sim 2\%$ ) are responsible for large residuals that range between 2.0 and 6.0 with respect to the rest of the data. The residual and rate of decrease of  $r_{k,\max}$  rapidly decreases with  $k$  in the first  $\sim 50$  iterations, then collapses on a relatively smooth curve, indicating that further filtering no longer rejects outliers. In this case, filtering was stopped after  $k = 50$  iterations ( $r_{k,\max} \simeq 1.2$ ), retaining 900 out of the initial 950 data points.

The retained ( $N_i - k \simeq 900$ ) data points span a temperature range of  $1000 \text{ K} < T < 2300 \text{ K}$  and provide the basis for the determination of the seven fit coefficients for Eq. 4.30. The resulting fit parameters are presented in Table 4.4. The magnitude of  $10^{15}$  of the pre-exponential  $\zeta_0$  offsets the very small magnitude of the exponential that is on the order of  $e^{-30}$ .

Table 4.4: Fit coefficients

$\zeta_0$	$7.81 \times 10^{15} \text{ s}^{-1}$
$a$	-10.6
$b$	0.628
$\beta$	30.0
$\eta$	-0.0026
$c$	0.0564
$d$	0.797

Equation 4.30 is valid within the range of temperature, pressure, and fuel and oxygen concentrations spanned by the experimental data set. It collapses onto a 2-dimensional response surface in  $[\theta, \pi]$ , plotted in Figure 4.8. The surface with the overlaid mesh depicts the region of validity in  $[\theta, \pi]$ -space of Eq. 4.30, while the points plot the experimental data on which the surface is based.

The combined induction-evolution expression then becomes

$$\zeta_i(\tau_i, \kappa, \tau_{i,0}, \theta, \pi, Y_{\text{C}_2\text{H}_4}, Y_{\text{O}_2}) = \log\left(\frac{\kappa}{\tau_{i,0}}\right) \tau_i \zeta_0 \theta^a \pi^b \exp\left(\frac{-\beta(1 + \eta\pi)}{\theta}\right) Y_{\text{C}_2\text{H}_4}^c Y_{\text{O}_2}^d, \quad (4.33)$$

with fit parameter values shown in Table 4.4. Figure 4.9 plots the residuals of the experimental ignition-delay data with respect to Eq. 4.33, vs. (scaled) temperature and pressure.

The mean (absolute value) of the residual across the range of conditions is, approximately, 0.34, and the mean residual is 0.07. The Pearson correlation coefficient of Eq. 4.33 with respect to the data, using the fit coefficients in Table 4.4, is 0.935.

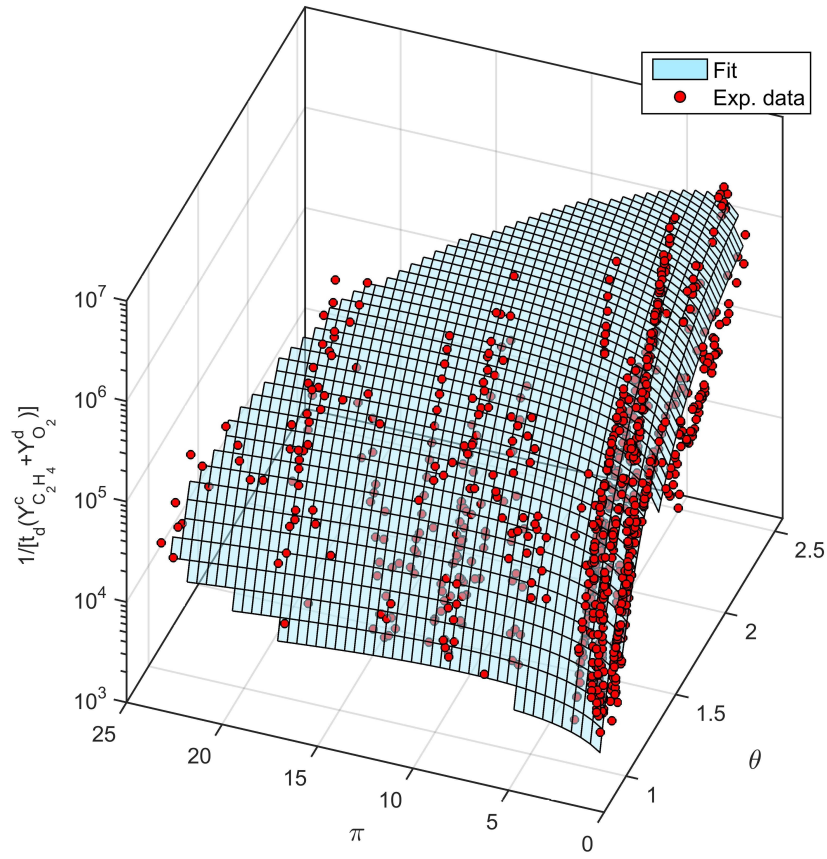


Figure 4.8: Reciprocal ignition-delay surface

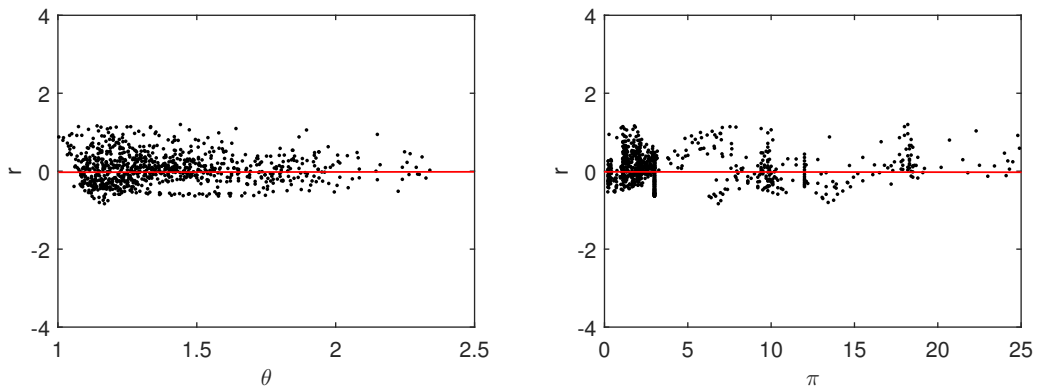


Figure 4.9: Residuals as a function of temperature (left) and pressure (right)

The experimental-data-driven approach to induction modeling described above can improve the reliability of simulations of autoignition-dominated complex-hydrocarbon combustion with regions of low temperature and off-stoichiometric conditions.

## 4.4 Post-ignition manifold

This section describes tabulating the post-ignition detailed composition and combustion-evolution rate as a function of four or five state variables that include the thermodynamic state  $\Theta$  (two variables,  $[h, p]$  or  $[e, \rho]$ ), a combustion-evolution variable,  $\tau_c$  (Eq. 4.34), a conserved mixture fraction,  $Z$  (Eq. 4.37), and a turbulent-entrainment parameter,  $\chi$  (cf. Section 4.2.2). For a reduced number of state variables, the value of  $\chi$  can be fixed to a characteristic value. The state variables are based on the Lagrangian WSR model introduced in Section 4.2.2 to describe the small-scale reaction zone in DRZ combustion. The table, or manifold,<sup>4</sup> contains the species mass-fraction vector,  $[Y_\alpha]$ , and aggregate combustion-evolution rate,  $\zeta_c$  (Eq. 4.36). The (post-ignition) combustion-evolution variable,  $\tau_c$ , that determines the extent of combustion completion in the material fluid element is defined as,

$$\tau_c = \frac{Y_P}{Y_{P,\text{eq}}} , \quad (4.34)$$

where  $Y_P$  is the local instantaneous product mass-fraction, which for hydrocarbons can be assume to be given by,

$$Y_P = Y_{\text{CO}} + Y_{\text{CO}_2} + Y_{\text{H}_2\text{O}} + Y_{\text{H}_2} , \quad (4.35)$$

excluding combustion products with small equilibrium mass fractions (e.g., Van Oijen and De Goey 2002, and others). The quantity  $Y_{P,\text{eq}}$  is the equilibrium value of  $Y_P$  at the local thermodynamic state and stoichiometry, i.e.,  $Y_{P,\text{eq}} = Y_{P,\text{eq}}(Z, e, \rho)$ . The value of  $\tau_c$  is then between zero and unity, i.e.,  $0 < \tau_c < 1$ .

---

<sup>4</sup>These two terms are used interchangeably in this section.

This definition of  $\tau_c$  is similar to the progress variable used by Van Oijen and De Goeij (2002), and others, in the Flamelet-Generated Manifold (FGM) formulation. A key conceptual difference, however, is that in the FGM formulation  $Y_P = Y_P(x_F)$ , where  $x_F$  is the spatial flame-normal coordinate, while in the EVM formulation  $Y_P$  evolves in Lagrangian reactor time,  $Y_P = Y_P(t)$ . The value of  $\tau_c$  is 0 for unburnt reactants and  $Y_P/Y_{P,\text{eq}} = 1$  at the local equilibrium (burnt) state. This allows EVM to track the Lagrangian evolution of the progress of combustion of a fluid element in a simulation.

The overall combustion-evolution rate is defined as,

$$\zeta_c = \frac{\dot{\omega}_{Y_P}}{Y_{P,\text{eq}}} , \quad (4.36)$$

where  $\dot{\omega}_{Y_P}$  is the product mass-fraction source term.  $\zeta_c$  is the source term for the combustion-evolution variable  $\tau_c$ .

The conserved mixture fraction is defined as the mass fraction of the reacting fluid that originates from a particular fuel stream. For the simple case of a single fuel stream in pure (not vitiated) oxidizer, and assuming no differential-diffusion effects in the turbulence environment considered here (cf. Barlow et al. 2005),  $Z$  is represented by elemental (atomic) mass fraction,  $\mathcal{Y}$ , of hydrogen and carbon ( $\mathcal{Y}_H + \mathcal{Y}_C$ ) in the fluid element relative to the elemental mass fraction of hydrogen and carbon in the fuel stream of the system, i.e.,

$$Z = \frac{\mathcal{Y}_C + \mathcal{Y}_H}{(\mathcal{Y}_C + \mathcal{Y}_H)_F} . \quad (4.37)$$

We note that the value of the denominator of Eq. 4.37 in a pure fuel stream is unity. For a pure-ethylene fuel stream, for example,

$$(\mathcal{Y}_C + \mathcal{Y}_H)_{\text{C}_2\text{H}_4} = 1 . \quad (4.38)$$

As an illustrative example, we calculate the value of  $Z$  for combustion products of a mixture of 0.1 ethylene and 0.9 air, by mass, with  $T_0 = 1200$  K, and  $p = 1$  bar. The second column of Table 4.5

lists the mass fractions of the  $i \leq 9$  species (left column) with mass fractions larger than  $10^{-5}$ . The third and fourth columns list the elemental carbon and hydrogen mass fraction contribution of each species, respectively. The right column lists the sum of the elemental hydrogen and carbon mass fraction contribution of each of the species listed. The sum of those contributions is 0.1, recovering the original fuel-stream mixture fraction.

Table 4.5: Mixture fraction,  $Z$ , example

	$Y$	$\mathcal{Y}_C$	$\mathcal{Y}_H$	$(\mathcal{Y}_C + \mathcal{Y}_H)$
N <sub>2</sub>	0.7001	0	0	0
CO	0.1653	0.0709	0	0.0709
H <sub>2</sub> O	0.0707	0	0.0079	0.0079
CO <sub>2</sub>	0.0540	0.0148	0	0.0148
H <sub>2</sub>	0.0058	0	0.0058	0.0058
OH	0.0029	0	0.0002	0.0002
H	0.0004	0	0.0005	0.0005
O <sub>2</sub>	0.0003	0	0	0
O	0.0003	0	0	0
$\Sigma \simeq 1$	$\Sigma = 0.086$	$\Sigma = 0.014$	$\Sigma = 0.1$	

Having defined the quantities  $Z$  and  $\tau_c$ , we can imagine the solution,  $[Y_\alpha(t)]$ , of Eq. 4.13 evolving along a trajectory in  $\mathbb{R}^5$  state space with coordinates  $[\tau_c, Z, \Theta, \chi]$ , starting from an initial point in  $\mathbb{R}^5$ , i.e.,  $[\tau_c, Z, \Theta, \chi]_{t=0}$ , through  $[\tau_c, Z, \Theta, \chi](t)$  (recall,  $\Theta = [h, p]$  or  $[e, \rho]$ ). The question is:

*Can the detailed composition of a Lagrangian fluid element in the DRZ regime, as defined in Eq. 4.13, be expressed only as a function of its state, or the instantaneous value of  $[\tau_c, Z, \Theta, \chi]$ , and not its history, or the trajectory traversed to that state?*

In other words, if Eqs. 4.13 and 4.16 or 4.18 are solved for different initial and entrained-fluid conditions, so that solution trajectories cross at some point in state space, i.e.,

$$[\tau_c, Z, \Theta, \chi]_1 = [\tau_c, Z, \Theta, \chi]_2 , \quad (4.39)$$

will the species mass-fraction vector be the same at that point,  $[Y_\alpha]_1 \simeq [Y_\alpha]_2$ , regardless of the trajectory traversed to reach that state?

If true, the detailed composition and reaction-evolution rate of a reacting fluid element can be expressed as a function of  $\tau_c$ ,  $\Theta$ ,  $Z$ , and  $\chi$ , only. In this approximation, the composition of a fluid parcel at some state is then independent of its history, or path taken (in state space), and can be estimated a priori using Eqs. 4.13, and 4.16 or 4.18. This, of course, needs to be verified. In the following analysis,  $\Theta$  is defined as  $[h, p]$  for simplicity.

Imagine a constant-pressure ( $p = p_0$ ), two-stream system wherein fuel and oxidizer are mixing and reacting. Combustion is assumed to occur in the DRZ regime. The thermochemical state of each stream is then specified by  $[Y_\alpha, h]_F$  and  $[Y_\alpha, h]_{Ox}$ .

We represent the domain by a collection of Lagrangian WSRs that obey Eqs. 4.13 and 4.16 and whose initial conditions  $Y_{\alpha,0}$  and  $h_0$  are linear combinations of the composition and enthalpy of the fuel and oxidizer streams,  $[Y_\alpha, h]_F$  and  $[Y_\alpha, h]_{Ox}$ . Initial and entrained-fluid mixture fractions are defined by  $Z_0$  and  $Z_{en}$ , respectively, where  $Z_0 \in [0, 1]$  and  $Z_{en} \in [0, 1]$ , and the level of combustion completion of the entrained fluid,  $\tau_{c,en}$ . The initial conditions of each reactor are prescribed by

$$[Y_\alpha, h]_{t=0} = Z_0 [Y_\alpha, h]_F + (1 - Z_0) [Y_\alpha, h]_{Ox}. \quad (4.40)$$

If a small quantity,  $\epsilon$ , of combustion products is premixed in the reactor, the initial conditions are given by

$$[Y_\alpha, h]_{t=0} = (1 - \epsilon) (Z_0 [Y_\alpha, h]_F + (1 - Z_0) [Y_\alpha, h]_{Ox}) + \epsilon (Z_0 [Y_\alpha, h]_F + (1 - Z_0) [Y_\alpha, h]_{Ox})_{eq}. \quad (4.41)$$

The subscript ‘eq’ denotes fluid in equilibrium at the enthalpy and pressure of the reactor at  $t = 0$  (combustion products). Fluid is entrained at various levels of combustion completion that range from unburnt to burnt,  $\tau_{c,en} \in [0, 1]$ , and its composition is given by

$$[Y_\alpha, h]_{\text{en}} = (Z_{\text{en}} [Y_\alpha, h]_F + (1 - Z_{\text{en}}) [Y_\alpha, h]_{\text{Ox}})_{\tau_c = \tau_{c,\text{en}}} . \quad (4.42)$$

Entrained fluid with  $\tau_{c,\text{en}} = 0$  is unburnt fluid, while entrained fluid with  $\tau_{c,\text{en}} = 1$  is at equilibrium (burnt fluid). Fluid with an intermediate value of combustion-completion ( $0 < \tau_{c,\text{en}} < 1$ ) is obtained by evolving a homogeneous, constant-pressure reactor to the desired entrained-fluid combustion-completion level.

As  $p$  and  $\chi$  are kept constant, the state-space trajectory of each convected material element in the flow will then evolve in a reduced-dimensionality  $\mathbb{R}^3$  space with coordinates  $[\tau_c, Z, h]$ , generating a set of solutions to Eqs. 4.13 and 4.16 whose trajectories may intersect in  $[\tau_c, Z, h]$ -space.

The intent, here, is to generate a set of intersecting trajectories (solutions), and compare the solution at these intersection points. With these solutions, we can answer the question of whether the species concentration,  $Y_\alpha$ , can be approximated as dependent on the point in  $[\tau_c, Z, h]$ -space, only, and is quasi-independent of the trajectory taken to that state.

We model a subset of Lagrangian fluid elements expected in a constant-pressure ( $p=1$  atm) ethylene-air system with fuel temperature  $T_F=1200$  K and air temperature  $T_{\text{Ox}}=1500$  K, with a constant value of  $\chi = 2 \times 10^4 \text{ s}^{-1}$ . A set of  $3 \times 10^4$  Lagrangian WSRs are initialized with initial conditions determined by Eq. 4.41, initial mixture fraction  $Z_0$ , and initial fraction of combustion product  $\epsilon$  randomly selected from a uniform distribution  $Z_0 \in [0.01, 0.2]$ ,  $\epsilon \in [0, 0.05]$ . The entrained-fluid composition is determined with a mixture fraction  $Z_{\text{en}}$  and level of combustion completion  $\tau_{c,\text{en}}$  randomly selected from uniform distributions  $Z_{\text{en}} \in [0.01, 0.4]$  and  $\tau_{c,\text{en}} \in [0, 1]$ .

In practice, because of lower neighborhood gradients in DRZ combustion, the entrained fluid composition and level of combustion completion would likely be close to that of the reactor, i.e.,  $\tau_{c,\text{en}} \sim \tau_c$  and  $Z_{\text{en}} \sim Z$ .

Scatter plots of the combustion-evolution rate ( $\zeta_c$ , Fig. 4.10) and fuel mass fraction (Fig. 4.11) in the domain are plotted against  $\tau_c$ , conditional on  $Z$  and  $h$  ( $Z = Z_{\text{cond}}$ ,  $h = h_{\text{cond}}$ ). Each point in the scatter plots corresponds to the value of  $Y_{\text{C}_2\text{H}_4}$  and  $\zeta_c$  at  $Z_{\text{cond}}$ ,  $h_{\text{cond}}$  and  $\tau_c$  that has reached that state via a different trajectory (i.e., different initial conditions and entrained-fluid properties). If the scatter plots generate a sufficiently thin line, the assumption of uniqueness may be considered

as adequate. The spread in the resulting scatter plots quantifies the uncertainty stemming from this assumption, i.e., that the resulting composition is a unique function of the fluid  $[\tau_c, Z, h]$ -state.

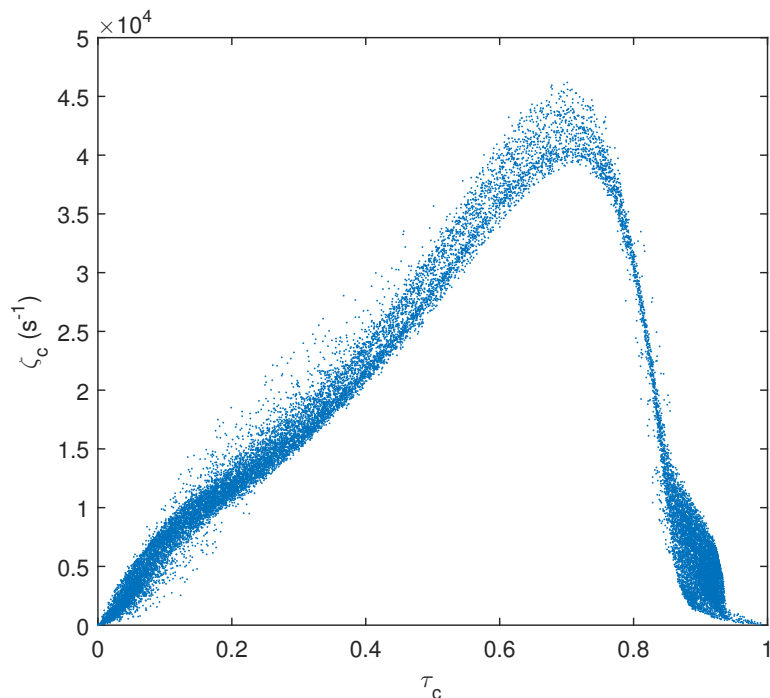


Figure 4.10: Overall reaction rate plotted against the combustion-evolution variable  $\tau_c$ , conditional on  $Z$  and  $h$ , for  $\tau_{c,\text{en}} \in [0, 1]$

The spread in the scatter plots indicates that assuming the composition of the fluid is a unique function of state would result in an error of  $\sim 10\%$  in the combustion-product source term, for the conditions considered here. The spread of the scatter plots, and therefore the error that the assumption of uniqueness entails, is expected to decrease if a more-realistic entrained fluid composition and level of combustion completion had been used, instead of a uniform distribution ( $\tau_{c,\text{en}} \in [0, 1]$ ), i.e., if the entrained fluid had been more similar to the neighboring reactor fluid in the LES. However, this requires adding and tracking an additional manifold coordinate.

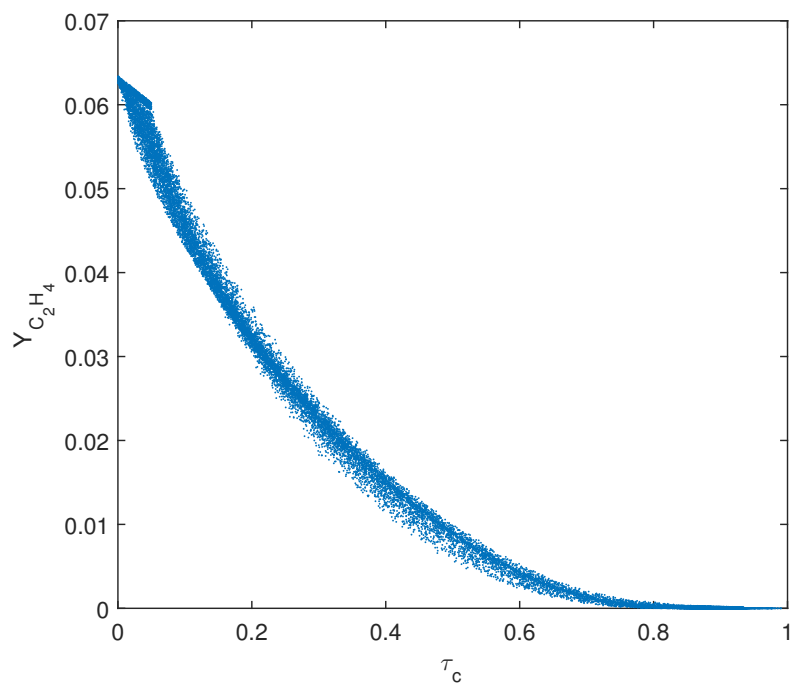


Figure 4.11: Fuel mass-fraction plotted against the combustion-evolution variable, conditional on  $Z$  and  $h$ , for  $\tau_{c,en} \in [0, 1]$

The data in Figs. 4.10 and 4.11 suggest that, under the assumptions of DRZ combustion, the state of a constant-pressure, constant- $\chi$  fluid element at a point in the reduced  $[\tau, Z, h]$ -space can be approximated as path-independent. In other words, it can be approximated as a unique function of  $[\tau, Z, h]$ , even at relatively high values of  $\chi$ , at least for ethylene-air combustion. Validation requires comparing the results of simulations that incorporate this assumption/approximation to supersonic-combustion experiments (cf. Chapter 5).

#### 4.4.1 Manifold-construction process

This concept can be used to build a manifold in state space for the detailed composition and overall reaction rate of a fluid reacting in a domain fed by a pure fuel stream with composition  $Y_{\alpha,F}$ , and a pure oxidizer stream with composition  $Y_{\alpha,Ox}$ . Enthalpy in the domain is bounded by

$h_{\min} < h < h_{\max}$ , pressure in the domain is bounded by  $p_{\min} < p < p_{\max}$ , and the entrainment rate  $\chi$  is bounded by  $0 < \chi < \chi_{\max}$ .

Consider the equations for a convected Lagrangian fluid element, Eqs. 4.13 and 4.18, with  $\Theta = [h, p]$ , reproduced here,

$$\frac{dY_\alpha}{dt} = \chi(Y_{\alpha,\text{en}} - Y_\alpha) + \dot{\omega}_{Y_\alpha}([Y_\alpha, h, p]),$$

$$\frac{dh}{dt} = \chi(h_{\text{en}} - h) + \frac{1}{\rho} \frac{dp}{dt}.$$

The initial conditions for these equations are:

$$\begin{aligned} p(t=0) &= p_0, \\ h(t=0) &= h_0, \\ Y_\alpha(t=0) &= Y_{\alpha,0}, \end{aligned} \tag{4.43}$$

with inputs:

$$\begin{aligned} \chi &= \chi(t), \\ h_{\text{en}} &= h_{\text{en}}(t), \\ Y_{\alpha,\text{en}} &= Y_{\alpha,\text{en}}(t), \\ p &= p(t). \end{aligned} \tag{4.44}$$

Given the relative insensitivity of the fluid-element composition to its history discussed above, the composition of the fluid at some (state) point in the  $\mathbb{R}^5$   $[\tau_c, Z, h, p, \chi]$ -space can be obtained by any trajectory passing through that state, including the simplest-possible trajectory that is a straight line parallel to the  $\tau_c$  axis (cf. Fig. 4.12). As a result,  $Y_\alpha$  and  $\zeta_c$  are tabulated as a function of  $[\tau_c, Z, h, p, \chi]$  using straight-line trajectories in  $[\tau_c, Z, h, p, \chi]$ -space initialized at  $[0, Z, h, p, \chi]$  and evolving to  $[\tau_{c,\max}, Z, h, p, \chi]$ . A straight-line trajectory parallel to the  $\tau_c$  axis is obtained by setting:

$$\begin{aligned}
 \chi(t) &= \chi_0 \\
 h_{\text{en}}(t) &= h_0 \\
 p(t) &= p_0 \\
 Z_{\text{en}}(t) &= Z_0.
 \end{aligned}
 \tag{4.45}$$

Defining  $\tau_{c,\text{en}}$  as a function of the fluid and thermochemical state surrounding the reactor would likely improve the model, adding an additional parameter (coordinate) to the manifold, at the expense of larger and more-complex tables, however. As the effects of  $\tau_{c,\text{en}}$  are weaker than the effects of the other variables, a 5-parameter model excludes  $\tau_{c,\text{en}}$  in favor of  $[\tau_c, Z, h, p, \chi]$ . To generate the tables, we approximate the entrained-fluid composition as pressure, enthalpy, and mixture-fraction matched  $Y_{P,\text{eq}}$ , corresponding to combustion products at equilibrium.

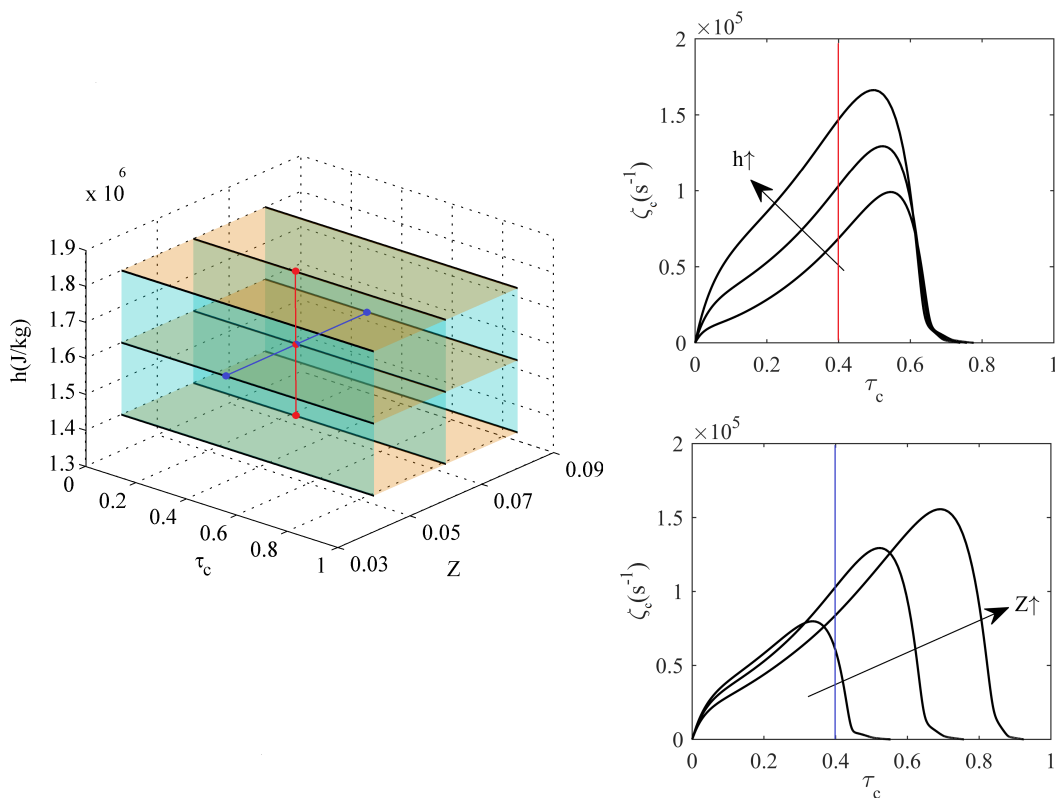


Figure 4.12: Table (left) in  $[Z, h, \tau_c]$ -space tabulating  $\zeta_c$  (right).

Figure 4.12 illustrates how a set of straight-line trajectories parallel to the  $\tau_c$  coordinate, with initial conditions  $[0, Z_{0,i}, h_{0,j}, p_0, \chi_0]$ , where  $Z_{0,i} = [0.04, 0.06, 0.08]$  and  $h_{0,j} = [1.4, 1.6, 1.8]$  MJ/kg generate a table containing  $\zeta_c$  information as a function of  $\tau_c$ ,  $Z$ , and  $h$ . The value of  $\zeta_c$  may be subsequently retrieved as a function of  $[\tau_c, Z, h]$ , with constant values of  $\chi = \chi_0$  and  $p = p_0$ .

The same approach is used to populate a volume in  $\mathbb{R}^5$  space using straight-line trajectories parallel to the  $\tau_c$  coordinate, where  $[Y_\alpha]$  and  $\zeta_c$  are tabulated vs.  $[\tau_c, Z, \Theta, \chi]$ . The following steps describe the process used to generate a uniformly discretized table with  $\Theta = [h, p]$ :

1. Define vectors of initial conditions for Eqs. 4.13 and 4.18, and entrained-fluid conditions that span the range of expected conditions:

$$\begin{aligned} \mathbf{Z}_0 &= [0, \delta Z, 2\delta Z, \dots, (n_Z - 1)\delta Z, 1] , \\ \mathbf{p}_0 &= p_{\min} + [0, \delta p, 2\delta p, \dots, (n_p - 1)\delta p, p_{\max} - p_{\min}] , \\ \mathbf{h}_0 &= h_{\min} + [0, \delta h, 2\delta h, \dots, (n_h - 1)\delta h, h_{\max} - h_{\min}] , \\ \mathbf{\chi}_0 &= [0, \delta \chi, 2\delta \chi, \dots, (n_\chi - 1)\delta \chi, \chi_{\max}] , \end{aligned} \tag{4.46}$$

where  $n_Z + 1$ ,  $n_p + 1$ ,  $n_h + 1$ ,  $n_\chi + 1$  are the lengths of each uniformly-spaced vector (typically on the order of 20-50, see Ch. 5), and  $\delta Z$ ,  $\delta p$ ,  $\delta h$ ,  $\delta \chi$  are their spacing. The conditions in Eq. 4.45 are then imposed to obtain straight-line trajectories parallel to the  $\tau_c$  coordinate.

2. Solve Eqs. 4.13 and 4.18 to steady state, for constant  $[Z, h, p, \chi]$  and for all possible combinations of initial conditions defined in Eq. 4.46, imposing the conditions in Eq. 4.45. This will generate  $(n_Z + 1) \times (n_p + 1) \times (n_h + 1) \times (n_\chi + 1)$  solutions (trajectories). For each solution (trajectory), the resulting species mass fractions,  $[Y_\alpha(t)]$ , and overall combustion-evolution rate  $\zeta_c(t)$ , are expressed as a function of  $\tau_c$  (the product-based combustion-evolution variable), instead of  $t$  through a change of variable,

$$\tau_c(t) = \frac{Y_P(t)}{Y_{P,\text{eq}}} . \tag{4.47}$$

3. Tabulate the values of  $Y_\alpha$  and  $\zeta_c$  of all points on all trajectories in an  $\mathbb{R}^5$  table in terms of their associated values of  $\tau_c, Z, h, p, \chi$  to generate the discretized manifold.

The detailed composition  $Y_\alpha$  and combustion-evolution rate  $\zeta_c$  can be retrieved from the tables

as a function of the local value of the local thermodynamic state ( $[h, p]$  in this case), the conserved mixture fraction  $Z$ , the combustion-evolution variable  $\tau_c$ , and the estimated value of  $\chi$ . The same process can be used to generate a table with  $\Theta = [e, \rho]$ , using Eq. 4.16 instead of Eq. 4.18.

#### 4.4.2 Combined data-driven induction model and post-ignition manifold

Figure 4.13 illustrates the definition of the overall reaction-evolution variable,  $\tau$ , during the various stages of combustion. Prior to ignition,  $\tau$  takes the value of the induction-evolution variable,  $\tau_i$ . Once ignition occurs, at a value of  $\tau = \kappa$ , the reaction-evolution variable takes the value of the combustion-evolution variable  $\tau_c$ .

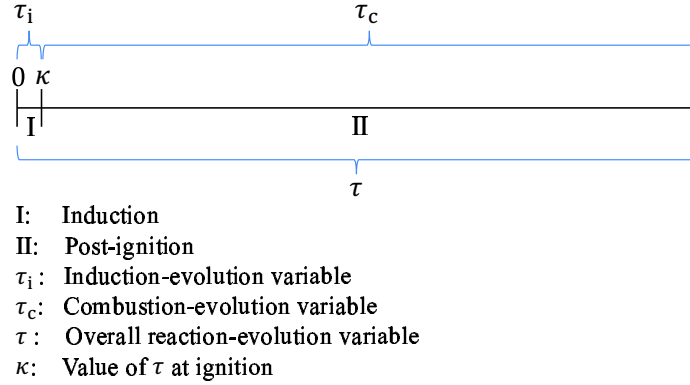


Figure 4.13: Definition of the overall reaction-evolution variable,  $\tau$ , during the various stages of combustion.

The value of the overall reaction evolution rate  $\zeta$  comprising both induction and post-ignition (combustion) is determined from the ignition-delay data-driven expression prior to ignition  $\zeta = \zeta_i$ , and takes the value of  $\zeta = \zeta_c$  post ignition. Ignition occurs when the value of the evolution variable,  $\tau$ , reaches an arbitrary small value, defined as  $\kappa$  (see Section 4.3.2). The value of  $\zeta$  must be continuous at  $\kappa$ , i.e.,  $\zeta_{c,\tau=\kappa} = \zeta_{i,\tau=\kappa}$ . To obtain a continuous curve, we solve for the free variable  $\tau_{i,0}$  in the expression for  $\zeta_i$ , Eq. 4.28, reprinted here:

$$\zeta_i(\tau_i, t_{d,c}, \kappa, \tau_{i,0}) = \log\left(\frac{\kappa}{\tau_{i,0}}\right) \tau_i \left(\frac{1}{t_{d,c}}\right),$$

with  $\zeta_i(\tau = \kappa) = \zeta_c(\tau = \kappa)$ . The value of  $\zeta_c(\tau = \kappa)$  is obtained from the tables for each set of conditions. The resulting value

$$\tau_{i,0} = \kappa \exp\left(-\frac{\zeta_c, \tau=\kappa t_{d,c}}{\kappa}\right), \quad (4.48)$$

is combined with Eq. 4.33 to obtain an expression for  $\zeta_i$  that transitions smoothly to  $\zeta_c$  at  $\tau = \kappa$ ,

$$\zeta = \begin{cases} \zeta_i, & \text{if } \tau < \kappa \\ \zeta_c, & \text{if } \tau > \kappa, \end{cases} \quad (4.49)$$

where  $\tau_i = \tau + \tau_{i,0}$ . Assuming only a small change in composition during induction, the composition vector during induction is that of unburnt fluid,  $Y_\alpha(\tau < \kappa) \simeq Y_\alpha(\tau = 0)$ . This assumption should be valid for ethylene, hydrogen, and for other simple fuels, but may not be valid for larger hydrocarbons that undergo pyrolysis accompanied by considerable heat release during induction. The following chapter illustrates an implementation of the EVM framework in a production LES code to simulate supersonic hydrogen-air combustion, with manifold reduced-dimensionality ( $\mathbb{R}^4$ ) coordinates  $[\tau, Z, \Theta, \chi = \chi_0]$ , where  $\Theta = [e, \rho]$  and  $\chi_0$  is a fixed characteristic value of the entrainment rate.

## Chapter 5

# Application of EVM to large-eddy simulations

This chapter discusses the application of the proposed EVM framework to large-eddy simulation (LES-EVM) modeling of turbulent, compressible, reacting flows in the DRZ regime. To date, several approaches to LES of supersonic combustion have been demonstrated. Berglund et al. (2010) used a partially stirred reactor (PaSR) model in a LES of supersonic combustion, transporting all species used by the chemical kinetics mechanism. Flamelet-generated manifold (FGM) methods with complex chemistry and some compressibility corrections that transport a reduced number of variables have been applied to supersonic combustion (e.g., Sabelnikov et al. 1998, Terrapon et al. 2009, Saghafian et al. 2015). These approaches rely on the assumption that supersonic combustion can be modeled as occurring in a flamelet regime, i.e., that supersonic combustion chemistry may be tabulated, and that the resulting tables are the same as what would be obtained using flamelet unit models.

EVM offers some advantages over these approaches for modeling DRZ combustion of hydrocarbons in LES. LES-EVM requires the transport of fewer variables than are required by chemical-kinetic mechanisms. On the other hand and as discussed above, the reduced dimensionality of transported species/variables places a burden of proof on the proposed framework and may require verification and validation for different combustion flow and chemical-kinetic environments. Additionally, the reliability of autoignition predictions is improved by incorporating experimental ignition-delay data into the model, where appropriate. Intense turbulence is assumed to locally ho-

mogenize the reacting fluid at small (subgrid) scales in the DRZ regime, disrupting the formation of quasi-laminar flamelets and leading to distributed reaction zones, as appropriate for combustion in the very-high Karlovitz number regime. Modeling DRZ combustion is facilitated by an appropriate unit model, such as an unsteady Lagrangian WSR, or ‘balloon’ reactor (Dimotakis and Hall 1987), in the EVM formulation.

## 5.1 LES-EVM overview

The LES transports four variables: energy,  $e$ , density,  $\rho$ , mixture fraction,  $Z$ , and a progress variable,  $C$ , defined as the product mass fraction, i.e.,

$$C = Y_P , \quad (5.1)$$

where, for hydrocarbon-air combustion,  $Y_P = Y_{\text{CO}} + Y_{\text{CO}_2} + Y_{\text{H}_2\text{O}} + Y_{\text{H}_2}$ , and for hydrogen-air combustion,  $Y_P = Y_{\text{H}_2\text{O}}$ , for example. The source term for the progress variable  $C$  is given by

$$\dot{\omega}_C = \dot{\omega}_{Y_P} , \quad (5.2)$$

where  $\dot{\omega}_{Y_P}$  is the sum of the source terms of the combustion products that constitute  $Y_P$ .  $C$  and  $\dot{\omega}_C$  related to  $\tau$  and  $\zeta_c$  by

$$\tau = \frac{C}{Y_{P,\text{eq}}(e, \rho, Z)} \quad (5.3)$$

and

$$\dot{\omega}_C = \zeta Y_{P,\text{eq}}(e, \rho, Z) , \quad (5.4)$$

where  $Y_{P,\text{eq}}(e, \rho, Z)$  is the product mass fraction at equilibrium ( $\tau = 1$ ), and is tabulated. The definition of the progress variable,  $C$ , as the sum of combustion-product mass fractions is typical in

tabulated chemistry (flamelet) approaches (e.g., Pierce and Moin 2004). The key difference is that in the EVM model,  $C$  maps to  $\tau$ , that is defined based on the temporal evolution of the product mass fractions relative to their equilibrium state in a Lagrangian homogeneous reactor (cf. Section 4.2). In flamelet formulations,  $C$  maps to the spatial distribution of product mass fraction along the flame-normal coordinate.

The governing conservation equations for a LES code using the EVM framework for a two-stream (fuel and oxidizer) system are,

$$\partial_t \rho + \partial_{\mathbf{x}} \cdot [\rho \mathbf{u}] = 0 , \quad (5.5a)$$

$$\partial_t(\rho Z) + \partial_{\mathbf{x}} \cdot [(\mathbf{u} + \mathbf{v}_Z)\rho Z] = 0 , \quad (5.5b)$$

$$\partial_t(\rho C) + \partial_{\mathbf{x}} \cdot [(\mathbf{u} + \mathbf{v}_C)\rho C] = \rho \dot{\omega}_C , \quad (5.5c)$$

along with momentum and energy-conservation equations. The variable  $Z$  represents the elemental mass fraction of fluid from a fuel stream (cf. Eq. 4.37). The variable  $C$  is the progress variable, as defined above, and has a source term,  $\dot{\omega}_C$ , that is a function of  $C, Z, e, \rho, \chi$  (cf. Eqs. 4.28 and 4.49). The velocities  $\mathbf{v}_Z$  and  $\mathbf{v}_C$  are the (turbulent) diffusion velocities for  $Z$  and  $C$ , respectively, solved by, or modeled in, the LES. The value of  $\tau$  is computed from  $[C, Z, e, \rho]$  in the LES using relation in Eq. 5.3.

At each time-step, the LES code provides the state vector (five variables),

$$[\Theta, Z, \tau, \chi] , \quad (5.6)$$

where  $\Theta = [e, \rho]$ , for each grid cell to the EVM module, which then returns the detailed fluid composition vector  $[Y_\alpha]$  and the overall reaction-evolution rate  $\zeta$  ( $N_\alpha + 1$  variables, where  $N_\alpha$  is the number of species), as shown in Fig. 5.1.  $[Y_\alpha]$  and  $\zeta$  are tabulated *a priori* based on the Lagrangian WSR and induction-evolution models, as described in the previous chapter. The value of the source term for the progress variable  $C$  is then obtained from  $[\zeta, Z, e, \rho]$  using the relation in Eq. 5.4.

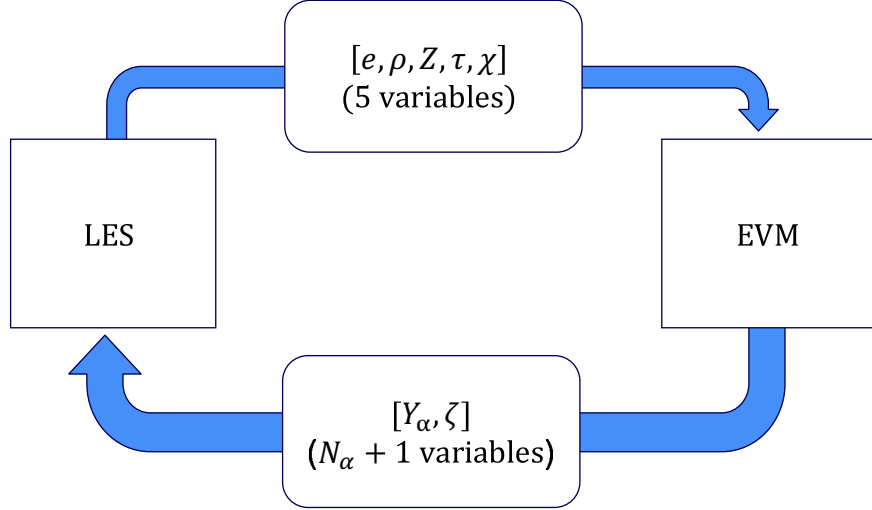


Figure 5.1: LES-EVM interaction diagram

A model estimate of the small-scale entrainment/mixing rate,  $\chi$ , in a LES can be obtained by approximating the small-scale turbulent velocity fluctuations,  $u'_R$ , and characteristic reactor size,  $\Delta_R$ , that define  $\chi$  in the Lagrangian WSR model by the subgrid-scale turbulent fluctuations and LES filter size, i.e.,

$$\chi = \frac{G}{2\Delta_R} u'_R \simeq \frac{G}{2\Delta} u'_{SG} , \quad (5.7)$$

where  $G$  is the geometrical prefactor described in Section 4.2.2, and  $\Delta$  is the spatial LES filter size.  $u'_{SG}$  is the magnitude of the subgrid-scale fluctuations can be approximately related to the (unresolved) subgrid-scale kinetic energy (e.g., Davidson 2009),  $ke_{SG}$ , e.g.,

$$u'_{SG} \simeq \sqrt{\frac{2}{3} ke_{SG}} . \quad (5.8)$$

$\chi$  can be estimated dynamically in the LES based on the local value of  $ke_{SG}$ , or estimated *a priori* based on a characteristic value of  $ke_{SG}$ . The assumption of near-homogeneity at subgrid-scales imposes a criterion on the LES resolution, i.e., that it must be high enough, and with a spatial filter size on the order of the reactor scale  $\Delta_R$ , that can be approximated to be on the order of the (thickened) reaction zone thickness (cf. Section 4.2.2). This can be tested computationally *ex post facto*, becomes a requirement for the application of the proposed framework, and may set the limits of the validity of the approach.

## 5.2 LES-EVM implementation for a reacting hydrogen jet in supersonic crossflow

The EVM method was implemented in the US3D production LES code for compressible reacting flows (Candler et al. 2015),<sup>1</sup> and applied to the hydrogen jet in supersonic heated air crossflow experiment performed by Gamba and Mungal (2015a) [G15a].

Supersonic combustion of hydrogen with air can be adequately simulated using chemical kinetics directly, however, the G15a dataset was determined to be a good candidate TJISCF experiment for comparison with simulation. Saghafian et al. (2015) applied a flamelet-generated manifold (FGM) to LES with compressibility corrections to the G15a experiment and captured the reaction zone at the interface between the jet and crossflow (cf. 5.2). Comparison with their results provides a useful assessment of relative merits and demerits of the two formulations in the same environment. Wang et al. (2015) also used FGM in a LES of the G15a experiment, capturing other reacting-flow features.

---

<sup>1</sup>N. Cymbalist and P. Dimotakis developed the framework and generated the manifolds; G. Candler modified the numerical methods in the US3D code to accommodate the EVM framework, iterated with N. Cymbalist and P. Dimotakis to refine the formulation and its interface with the LES code, generated the grid, and performed the simulations; the results were analyzed by N. Cymbalist, G. Candler, and P. Dimotakis.

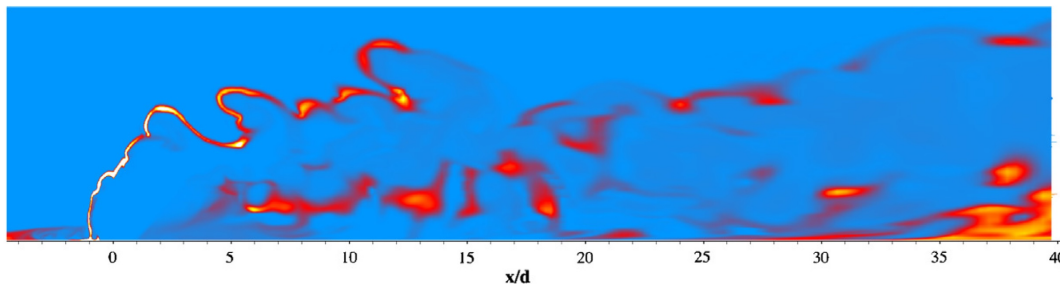


Figure 5.2: Instantaneous OH mass fraction at the centerplane from an LES incorporating a flamelet model with compressibility corrections (Saghafian et al. 2015, Fig. 8, reproduced with permission), of the Gamba and Mungal (2015a) experiment (cf. Fig. 5.5)

### 5.2.1 Manifold construction

Four-dimensional ( $\mathbb{R}^4 = [e, \rho, Z, \tau]$ ) post-ignition manifolds, for the  $\text{H}_2$ -air system were generated by holding  $\chi$  at a fixed value  $\chi_0$ . The value of  $\chi_0$  is selected based on a characteristic value of anticipated turbulence intensity that was approximated as uniform, but which can be variable in more detailed EVM-LES formulations, as circumstances may warrant. As an example, we assume that the LES resolves  $\sim 85\%$  of the turbulent kinetic energy (TKE),  $ke$ , of the flow (e.g., Pope 2004), that can be approximated by

$$ke = \frac{3}{2} u'^2, \quad (5.9)$$

where  $u'$  is the (RMS) magnitude of one component of the turbulent velocity fluctuations, assuming quasi-isotropic flow. The unresolved TKE,  $ke_{\text{SG}} \simeq 0.15 ke$ , contributes to the subgrid-scale velocity fluctuations that determine the value of  $\chi$  (Eq. 5.7). Assuming a characteristic value of  $u' \simeq 0.05 U_\infty$  for a TJISCF (Santiago and Dutton 1997, cf. Chapter 4), where  $U_\infty \simeq 1800$  m/s, the geometrical prefactor is  $G = 3$ , corresponding to a quasi-spherical reactor (Eq. 4.19 and related discussion), and assuming a characteristic reactor size  $\Delta_R$  of  $5 \times 10^{-4}$  m, a characteristic value for  $\chi$  is  $\approx 10^5 \text{ s}^{-1}$ . Half of this value of  $\chi$  was selected for the first implementation described here to facilitate time-integration of the Lagrangian WSR equations. In particular, for the hydrogen-air tables constructed here,  $\chi = 5 \times 10^4 \text{ s}^{-1}$ . Autoignition was modeled with the induction-evolution expression

incorporating characteristic ignition-delay. The characteristic ignition delay was determined using constant-volume homogeneous reactors with detailed chemical kinetics, that are deemed to reliably capture hydrogen-air ignition at the conditions of the experiment. For hydrocarbon combustion, the induction-evolution expression could be based on experimental data, if such data are available.

The Burke et al. (2012) hydrogen-air detailed chemical kinetics mechanism (11 species, 27 reactions) was used for the characteristic ignition-delay estimates, and to populate the post-ignition manifold. The energy,  $e$ , and density,  $\rho$ , range of the table was dictated by the estimated bounding values from the experimental conditions, shown in Table 5.1.

Table 5.1: Gamba (2015a) experimental conditions

$T_{0,j}$	295 (K)
$p_{0,j}$	2034 (kPa)
$T_{\infty}$	1400 (K)
$p_{\infty}$	40 (kPa)
$M_{\infty}$	2.4
$X_j$	H <sub>2</sub> :1
$X_{\infty}$	0.7812:N <sub>2</sub> ,0.2095:O <sub>2</sub> ,0.0093:Ar
$d_j$	2 mm

These conditions resulted in a post-ignition manifold with state range of

$$\begin{aligned}
 0.001(\text{kg}/\text{m}^3) &\leq \rho \leq 2.8(\text{kg}/\text{m}^3), \\
 -4 \times 10^6(\text{J}/\text{kg}) &\leq e \leq 10^7(\text{J}/\text{kg}), \\
 0 &\leq Z \leq 1, \\
 0 &\leq \tau \leq 1.
 \end{aligned}
 \tag{5.10}$$

The discretization is non-uniform in all coordinates. Each sub-figure in Fig. 5.3 shows the coordinate index versus the value at that index, for  $\tau$ ,  $Z$ ,  $e$ , and  $\rho$  coordinates. A higher slope indicates a coarser discretization in that state range. The table range and resolution was approximated based on anticipated flow conditions. Future implementations of such discretized high-dimensional manifolds would benefit from improved table refinement methods, perhaps by extending 3D adaptive mesh

refinement (AMR) algorithms to higher dimensionality.

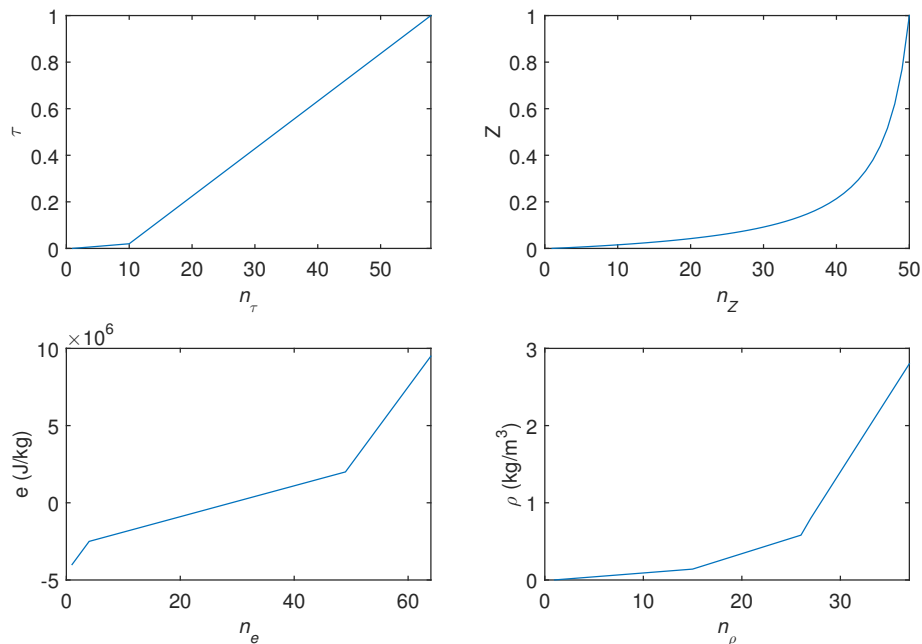


Figure 5.3: Hydrogen-air manifold discretization for the evolution-variable coordinate  $\tau$  (top left), mixture fraction  $Z$  (top right), internal energy  $e$  (bottom left), and density  $\rho$  (bottom right), in terms of the coordinate value plotted against the corresponding index.

Visualizing data held in  $\mathbb{R}^4 = [e, \rho, Z, \tau, \chi = \chi_0]$  tables is challenging. An option is to extract  $\mathbb{R}^3$  volume subsets of the  $\mathbb{R}^4 = [e, \rho, Z, \tau]$  data by holding one coordinate fixed. As an example, Fig. 5.4 (left) shows slices of the H<sub>2</sub>O mass fraction as a function of mixture fraction,  $Z$ , density,  $\rho$ , and the normalized evolution variable,  $\tau$ , for a fixed value of specific energy,  $e = 0$  J/kg (referenced to  $T_0 = 298.15$  K). Figure 5.4 (right) shows slices of H<sub>2</sub>O mass fraction as a function of mixture fraction,  $Z$ , specific energy,  $e$ , and evolution variable,  $\tau$ , for a fixed value of density,  $\rho = 0.5$  kg/m<sup>3</sup>. The grid illustrates the non-uniform discretization along each coordinate. Regions without data (low  $Z$ , high  $e$  region in Fig. 5.4, right) correspond to thermochemical states that are not expected to be visited by the LES.

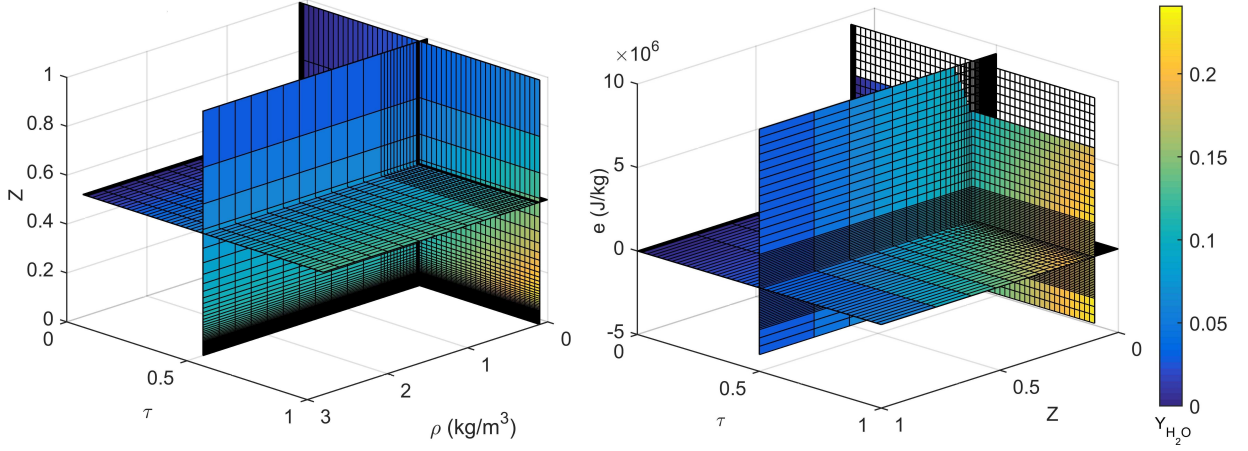


Figure 5.4: Left: H<sub>2</sub>O mass-fraction slices as a function of  $[Z, \rho, \tau]$ , with  $e = 0$  J/kg. Right: H<sub>2</sub>O mass-fraction slices as a function of  $[Z, e, \tau]$ , with  $\rho = 0.5$  kg/m<sup>3</sup>.

The characteristic ignition-delay time was calculated using homogeneous constant-pressure reactors, and tabulated as a function of  $[e, \rho, Z]$ . The induction-evolution rate  $\zeta_i$  determined using simulated characteristic ignition-delay times was incorporated into the table for  $\tau < \kappa$ , where  $\kappa = 0.02$ , using the approach detailed in Section 4.4.2 (Eq. 4.49).

## 5.2.2 Results

We present the results of a large-eddy simulation incorporating the EVM framework for the Gamba and Mungal (2015a) [G15a] reacting jet in crossflow experiments performed on an unstructured, 70-million element grid, with a Smagorinski subgrid-scale model. Details of the numerical approach<sup>2</sup> and subgrid-scale modeling are in Candler et al. (2015a, 2016\*). Results presented here are intended to demonstrate the potential and illustrate the use of the proposed approach by direct comparison of simulated OH concentration with the measured OH-PLIF signal. We note that the simulations described in this chapter have not undergone a grid-convergence study. Improved resolution at the upper interface between the jet and crossflow (cf. Figs 5.5, 5.6) would better capture the thin reaction zones present in those regions.

<sup>2</sup>The numerical methods in the LES were developed specifically for EVM-LES by G. Candler. \*In preparation.

Figure 5.5 (from G15a) shows an OH-PLIF image of the reacting hydrogen TJICF experiment on the jet centerplane, with flow from left to right. Some important elements of the reaction-zone structure are: the thin reaction zone at the interface between the jet and crossflow, the recirculation zone upstream of the jet, and the distributed reaction zone in the boundary layer downstream and surrounding the jet. Gamba identified the latter feature as a principal, and possibly dominant, heat-release mechanism in a reacting TJISCF.

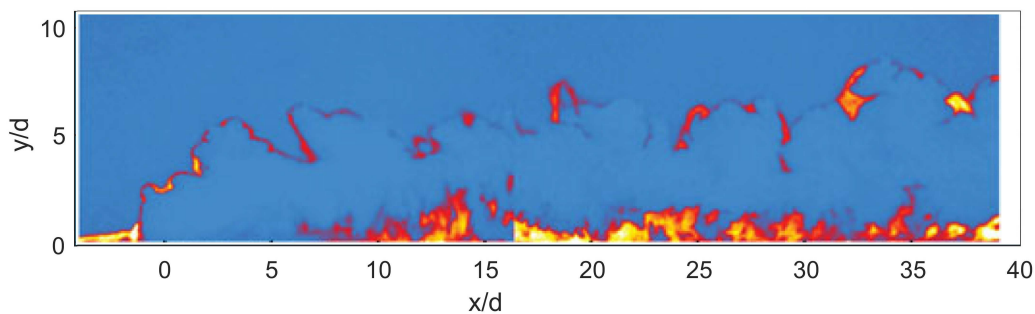


Figure 5.5: OH-PLIF image of the crossplane in a reacting hydrogen-air TJISCF, from Gamba (2015a), Fig. 9, reproduced with permission.

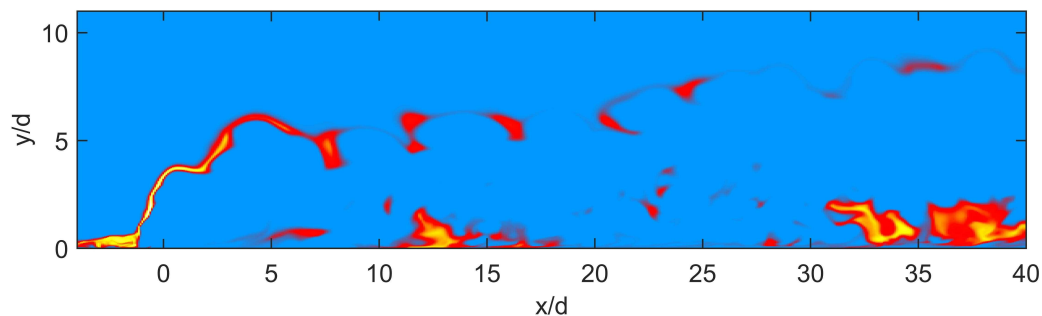


Figure 5.6: Centerplane OH concentration from an EVM-LES simulation of the G15a experiment. Figure based on LES data courtesy of G. Candler.

Figure 5.6 shows the OH-concentration contour on the mid-span plane extracted from a representative instantaneous snapshot from the LES, and plotted with a similar color scheme as the experimental OH-PLIF image in Fig. 5.5.

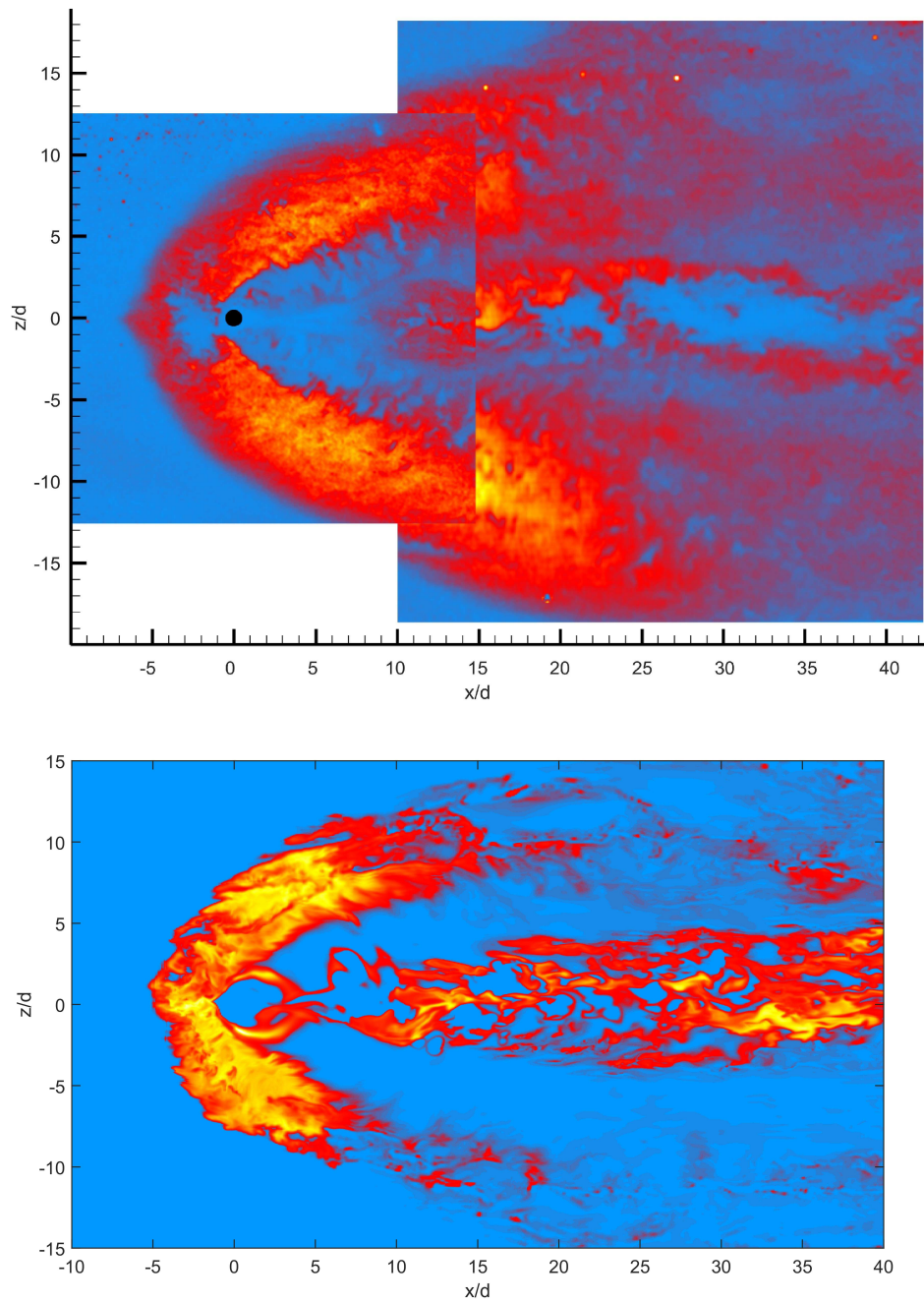


Figure 5.7: Experimental OH-PLIF image (top, Gamba 2015a, Fig. 18, reproduced with permission) and simulated OH mass fraction (bottom, figure based on LES data courtesy of G. Candler.) on a plane parallel to the lower guidewall, at  $y/d_j = 0.25$ .

The simulation captures the broken, thin reaction zones at the interface between the cold hydrogen jet body and the heated-air crossflow reasonably well. The OH layer appears thicker in the simulation than the experimental data. This is caused, in part, by the coarse, perhaps insufficient, grid resolution in those regions.

Additionally, the EVM model assumes that all combustion occurs in the DRZ regime, as opposed to a thin-flamelet regime in places, and this could also contribute to some of the observed differences, in part. The broken/distributed reaction zones under the jet plume are well captured by the LES-EVM, as well as the important near-wall recirculation zone upstream of the jet.

Gamba captured OH-PLIF images of a broad near-wall burning region in the boundary layer that extends laterally 10 to 15 jet diameters on either side of the jet orifice, and 25 diameters downstream of injection, as shown in Fig. 5.7 (top).

The recirculation zone upstream of the jet acts as a flameholder for the bulk of the near-wall burning occurring in the boundary layer, and this mechanism is captured by the LES. Figure 5.7 (bottom) shows the OH concentration on a plane parallel to the lower guidewall, at  $y/d_j = 0.25$ , where  $y$  is the guidewall-normal coordinate. The LES results show regions with OH concentration in the boundary layer that extend laterally from the jet approximately 10 jet diameters, and downstream to approximately 15 jet diameters. The extent of the reaction zones in the LES-EVM is slightly smaller than observed experimentally. Capturing the reactions in the boundary layer requires an accurate model for the turbulent boundary layer and other flow features in the experiment.

Figure 5.8 shows combustion-product ( $\text{H}_2\text{O}$ ) mass fraction (top), and temperature (bottom) fields on the centerplane of the jet obtained from the LES-EVM. Gamba et al. (2015) performed toluene-PLIF thermometry on a cold-flow hydrogen or argon in  $M_\infty = 2.4$  air TJISCF (details in Section 3.1). Gamba et al. captured the development of shear-layer structures on the leading edge of the hydrogen jet that evolve into periodic large structures in the wake of the jet. The LES-EVM captures the evolution of these structures.

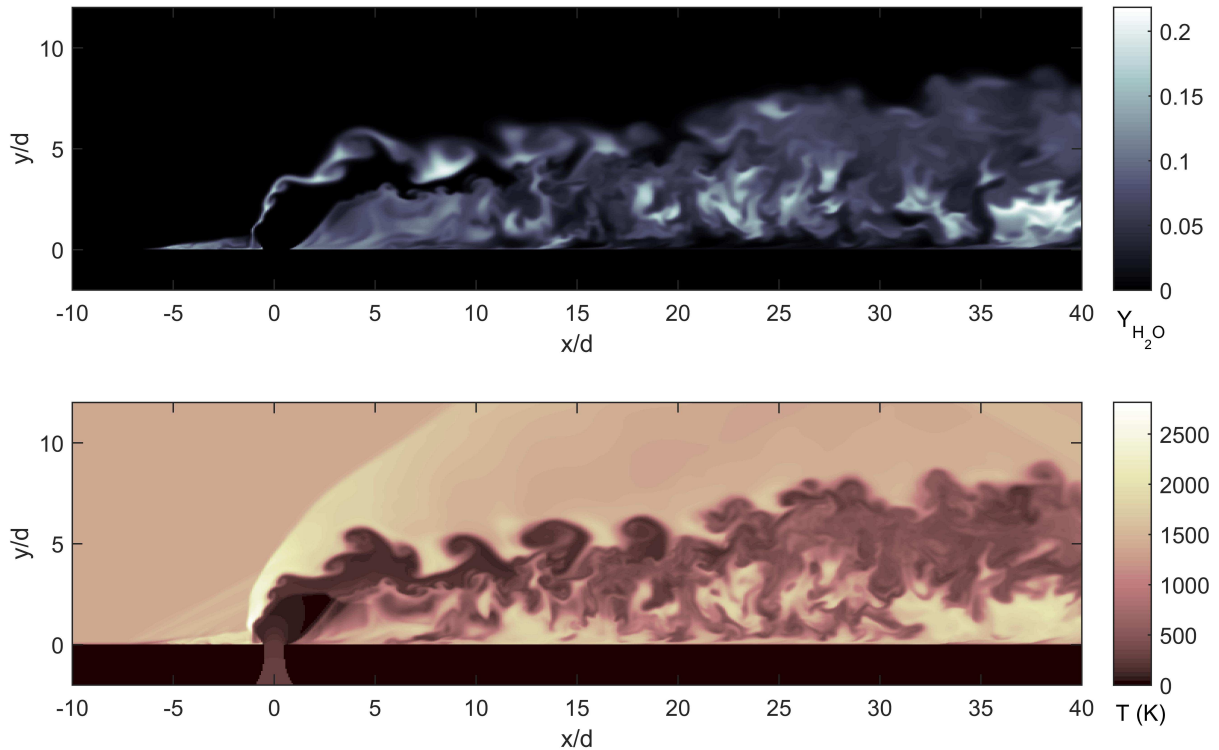


Figure 5.8: Centerplane  $\text{H}_2\text{O}$  mass fraction (top), and temperature (bottom) from the LES-EVM simulation of the G15a experiment. Figure based on LES data courtesy of G. Candler.

We note that the LES-EVM results are sensitive to grid resolution and details of the numerics in the LES. Simulations with different grid resolutions and spatial numerical order of accuracy exhibit some differences in the reacting flow field. Figure 5.9 shows the OH contours of two simulations with different grid resolution and spatial numerical order of accuracy. The top figure shows OH contours at the centerplane from a simulation with 70 million elements, and second-order spatial accuracy (cf. Figs. 5.6 and 5.7), while the bottom figure shows OH contours at the centerplane from a simulation with 14 million elements, and fourth-order spatial accuracy. The instantaneous structure of the reaction-zones under the plume is slightly different, as is the extent of the recirculation zone upstream of the jet.

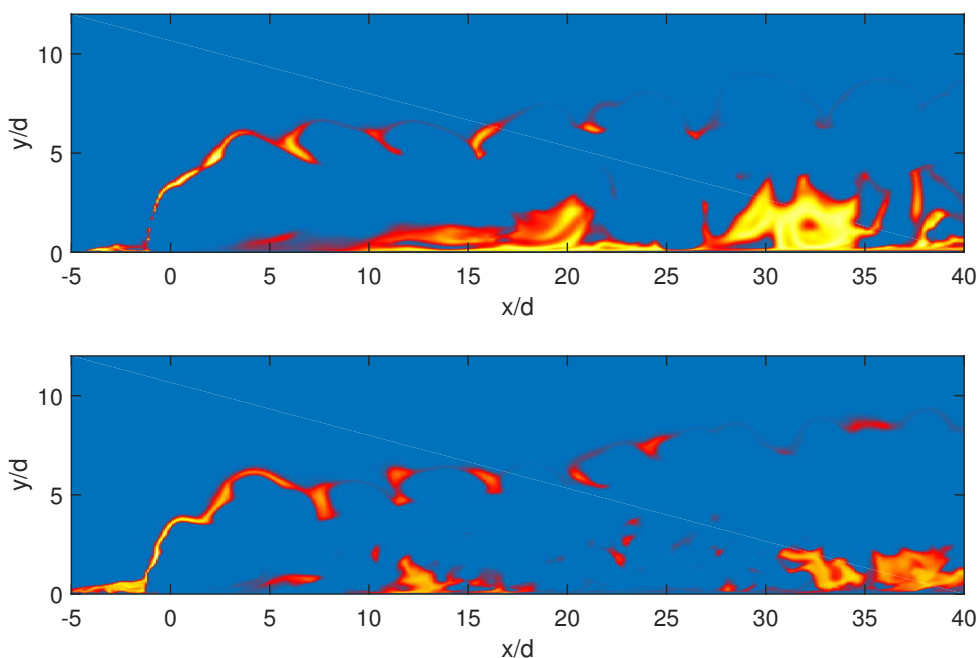


Figure 5.9: OH contours for simulations with grid resolution of 14 million elements, with fourth-order spatial accuracy (top), and 70 million elements, with second-order spatial accuracy (bottom). Figure based on LES data courtesy of G. Candler.

In summary, the results of the LES-EVM simulation of the G15a experiment illustrate some of the capabilities of the EVM framework. Using a reduced number of transported variables, several important features of the reacting flowfield are captured. Improved flow modeling, manifold discretization and dimensionality is expected to further improve the results. The LES-EVM approach in its current form is directly applicable to two-stream (fuel and oxidizer) complex hydrocarbon combustion in relevant conditions, requiring no additional computing resources during runtime. Additional computing resources are required to compute tables based on larger detailed chemical kinetic mechanisms, but these are modest compared to those required by the LES. The tables are reusable for specific fuel-air mixtures. More advanced combustion features, including air vitiation, multiple fuel streams, or hydrocarbons that undergo thermal cracking (e.g., Nakaya et al. 2015) in the combustion chamber may require modifications of the EVM framework.

## Chapter 6

# Conclusions

An experimental investigation of reacting transverse jets in supersonic crossflow (TJISCF) was conducted at the GALCIT S<sup>3</sup>L facility, using chemiluminescence and schlieren image-correlation velocimetry (SICV) diagnostics. The reacting flow field was found to depend on several parameters, including jet-fluid molar mass, jet-orifice diameter, and jet inclination. A framework was developed and implemented for efficient simulation of supersonic combustion occurring in the DRZ regime, with a data-driven induction model. Conclusions were presented in each chapter, and are summarized below.

**Jet Reynolds number.** Increasing the jet-fluid molar mass  $W_j$  and/or jet diameter increases the jet-diameter based Reynolds number,  $Re_j$ . The mixing-delay length normalized by the jet-source diameter (cf. Eq. 3.4) of a normal TJISCF was found to have an inverse power-law dependence on  $Re_j$ , with a zero offset. Higher- $W_j$  jets with a higher Reynolds number mix further upstream when compared to lower- $W_j$  jets, underscoring some of the advantages of large-hydrocarbon (higher  $W$ ) fueled scramjets.

Suggested future experimental work includes expanding the parameter space to higher momentum-flux ratio ( $J$ ) values, and crossflow densities, to determine whether the jet Reynolds number and jet-source diameter scaling of the mixing-delay length is valid outside the range of parameters examined here.

**Jet inclination.** A 30° jet-orifice inclination considerably decreases the normal-jet disturbance on the flow caused by the near-normal bow shock and normal-jet effects on momentum, but reduces

penetration. In an inclined jet, molecular mixing and chemiluminescence occurs approximately 50% farther downstream than for an otherwise similar normal jet. The recirculation zone upstream of a normal jet that anchors the near-wall burning region is not also present in an inclined jet. The results suggest that a balance between efficient mixing and combustion and acceptable disturbance to the crossflow will likely dictate the injection angle in a flight vehicle. Simple control-volume analysis supports some of these conclusions, illustrating the role of jet inclination to overall flow characteristics.

The experiments reported here constitute the first reported inclined reacting jet in supersonic crossflow experiments, and merit considerable follow-up experimental work. In particular, it would be useful to explore a range of jet-inclination angles, to determine the minimum inclination necessary for an upstream flameholding recirculation zone. In addition, it would be interesting to determine whether the jet-fluid molar mass effects observed in the normal-jet experiments are also present in the inclined-jet case.

**Evolution-variable manifold (EVM) framework.** Using turbulence-chemistry scaling arguments, supersonic hydrocarbon combustion in low Mach number supersonic combustors is anticipated to occur primarily in the distributed reaction-zone (DRZ) regime. At the smallest scales, DRZ combustion was modeled as a collection of convected, unsteady Lagrangian reactors that entrain and mix with surrounding fluid, whose turbulent mixing and chemical timescales are comparable. At low temperatures and off-stoichiometric conditions, variances between chemical-kinetic predictions and experimental data can be up to an order of magnitude. An ignition-delay data-driven model for induction evolution with an exponential growth rate can capture the evolution of the radical pool leading to autoignition.

The Lagrangian WSR model was combined with the data-driven induction-evolution model to generate state-space manifolds (look-up tables). These tabulate the approximate thermochemical reacting-fluid state with arbitrarily complex chemistry in the DRZ regime, indexed in terms of a reduced number of transported variables. These tables form the basis of the EVM framework. A first implementation of EVM was integrated in a LES of turbulent combustion of a hydrogen jet in supersonic air crossflow, capturing several important flow features. The results illustrate the potential of the EVM framework for simulating supersonic hydrocarbon combustion in the DRZ regime with important autoignition effects. This would have been challenging to capture

using existing methods. In future implementations of EVM, the framework can be extended to include large hydrocarbons that thermally 'crack' prior to combustion, multi-fuel streams, vitiated-air combustion, and other flow-combustion variants.

# Bibliography

- ANDREOPOULOS, J. AND W. RODI. 1984. Experimental investigation of jets in a crossflow. *Journal of Fluid Mechanics*, **138**:93–127.
- ASPDEN, A., M. DAY, AND J. BELL. 2011. Turbulence–flame interactions in lean premixed hydrogen: transition to the distributed burning regime. *Journal of Fluid Mechanics*, **680**:287–320.
- BAKER, J. A. AND G. B. SKINNER. 1972. Shock-tube studies on the ignition of ethylene-oxygen-argon mixtures. *Combustion and Flame*, **19**(3):347–350.
- BALAKRISHNAN, G. AND F. WILLIAMS. 1994. Turbulent combustion regimes for hypersonic propulsion employing hydrogen-air diffusion flames. *Journal of Propulsion and Power*, **10**(3):434–437.
- BARLOW, R., J. FRANK, A. KARPETIS, AND J.-Y. CHEN. 2005. Piloted methane/air jet flames: Transport effects and aspects of scalar structure. *Combustion and Flame*, **143**(4):433–449.
- BATEUP, M. L., A. PAULL, AND D. J. MEE. 2013. Ethylene augmentation of JP-8+ 100 in a supersonic combustor. *49th AIAA/ASME/SAE/ASEE Joint Propulsion Conference*. AIAA 2013-3700.
- BATT, R. 1977. Turbulent mixing of passive and chemically reacting species in a low-speed shear layer. *Journal of Fluid Mechanics*, **82**(01):53–95.
- BAURLE, R. AND S. GIRIMAJI. 2003. Assumed PDF turbulence-chemistry closure with temperature-composition correlations. *Combustion and Flame*, **134**(1):131–148.
- BECKER, K., W. GROTH, AND D. THRAN. 1972. Mechanism of the air afterglow  $\text{NO} + \text{O} \rightarrow \text{NO}_2 + h\nu$ . *Proceedings of Symposium (International) on Combustion*, **14**(1):353–363.
- BEN-YAKAR, A. 2000. *Experimental investigation of mixing and ignition of transverse jets in supersonic crossflows*. Ph.D. thesis, Stanford University.

- BEN-YAKAR, A., M. MUNGAL, AND R. HANSON. 2006. Time evolution and mixing characteristics of hydrogen and ethylene transverse jets in supersonic crossflows. *Physics of Fluids*, **18**(2):026101.
- BERGLUND, M., E. FEDINA, C. FUREBY, J. TEGNER, AND V. SABEL'NIKOV. 2010. Finite rate chemistry large-eddy simulation of self-ignition in supersonic combustion ramjet. *AIAA Journal*, **48**(3):540–550.
- BERGTHORSON, J. M., M. B. JOHNSON, A. M. BONANOS, M. SLESSOR, W.-J. SU, AND P. E. DIMOTAKIS. 2009. Molecular mixing and flowfield measurements in a recirculating shear flow. Part I: subsonic flow. *Flow, Turbulence and Combustion*, **83**(2):269–292.
- BONANOS, A. M., J. M. BERGTHORSON, AND P. E. DIMOTAKIS. 2009. Molecular mixing and flowfield measurements in a recirculating shear flow. Part II: supersonic flow. *Flow, Turbulence and Combustion*, **83**(2):251–268.
- BOND, C. L. 2000. *Reynolds number effects on mixing in the turbulent shear layer*. Ph.D. thesis, California Institute of Technology.
- BORCHI, R. 1984. Mise au point sur la structure des flammes turbulentes. *Journal de Chimie Physique*, **81**(6):361–370.
- BROWAND, F. AND B. LATIGO. 1979. Growth of the two-dimensional mixing layer from a turbulent and nonturbulent boundary layer. *Physics of Fluids (1958-1988)*, **22**(6):1011–1019.
- BURKE, M. P., M. CHAOS, Y. JU, F. L. DRYER, AND S. J. KLIPPENSTEIN. 2012. Comprehensive H<sub>2</sub>/O<sub>2</sub> kinetic model for high-pressure combustion. *International Journal of Chemical Kinetics*, **44**(7):444–474.
- CANDLER, G. V., N. CYMBALIST, AND P. E. DIMOTAKIS. 2015. Large-eddy simulation of autoignition-dominated supersonic combustion. *45th AIAA Fluid Dynamics Conference*. AIAA 2015-3340.
- CASHION, J. AND J. POLANYI. 1959. Infrared chemiluminescence from the gaseous reaction atomic H+NO → HNO emission. *The Journal of Chemical Physics*, **30**(1):317–318.
- CHAKRABORTY, D., P. PAUL, AND H. MUKUNDA. 2000. Evaluation of combustion models for high speed H<sub>2</sub>/air confined mixing layer using DNS data. *Combustion and Flame*, **121**(1):195–209.

- CLYNE, M. AND B. THRUSH. 1962. Mechanism of chemiluminescent reactions involving nitric oxide - the H+NO reaction. *Discussions of the Faraday Society*, **33**:139–148.
- COCKS, P. 2011. *Large eddy simulation of supersonic combustion with application to scramjet engines*. Ph.D. thesis, University of Cambridge.
- COLIN, O., A. P. DA CRUZ, AND S. JAY. 2005. Detailed chemistry-based auto-ignition model including low temperature phenomena applied to 3-D engine calculations. *Proceedings of the Combustion Institute*, **30**(2):2649–2656.
- COLKET, M. B. AND L. J. SPADACCINI. 2001. Scramjet fuels autoignition study. *Journal of Propulsion and Power*, **17**(2):315–323.
- CURRAN, E. 2001. *Scramjet Propulsion*. AIAA, Reston, VA.
- CYMBALIST, N., E. LUTHMAN, D. LANG, AND P. E. DIMOTAKIS. 2016. Schlieren-image correlation velocimetry for high-speed flows. *In preparation*.
- DA CRUZ, A. P. 2004. Three-dimensional modeling of self-ignition in HCCI and conventional diesel engines. *Combustion Science and Technology*, **176**(5-6):867–887.
- DAGAUT, P., J.-C. BOETTNER, AND M. CATHONNET. 1990. Ethylene pyrolysis and oxidation: A kinetic modeling study. *International Journal of Chemical Kinetics*, **22**(6):641–664.
- DAHM, W. J. AND P. E. DIMOTAKIS. 1987. Measurements of entrainment and mixing in turbulent jets. *AIAA Journal*, **25**(9):1216–1223.
- DAHM, W. J. AND P. E. DIMOTAKIS. 1990. Mixing at large Schmidt number in the self-similar far field of turbulent jets. *Journal of Fluid Mechanics*, **217**:299–330.
- DAVIDSON, D. AND R. HANSON. 2004. Interpreting shock tube ignition data. *International Journal of Chemical Kinetics*, **36**(9):510–523.
- DAVIDSON, L. 2009. Large eddy simulations: how to evaluate resolution. *International Journal of Heat and Fluid Flow*, **30**(5):1016–1025.
- DAVIS, S., C. LAW, AND H. WANG. 1999. Propene pyrolysis and oxidation kinetics in a flow reactor and laminar flames. *Combustion and Flame*, **119**(4):375–399.

- DIMOTAKIS, P. E. 1991. Turbulent free shear layer mixing and combustion. *High Speed Flight Propulsion Systems*, **137**:265–340.
- DIMOTAKIS, P. E. 1997. Cover illustration: Non-premixed hydrocarbon flame. *Nonlinearity*, **10**(1):1–2.
- DIMOTAKIS, P. E. 2000. The mixing transition in turbulent flows. *Journal of Fluid Mechanics*, **409**:69–98.
- DIMOTAKIS, P. E. 2005. Turbulent mixing. *Annual Review of Fluid Mechanics*, **37**:329–356.
- DIMOTAKIS, P. E., J. BROADWELL, AND M. G. MUNGAL. 1984. Turbulent mixing and combustion in a reacting shear layer. *AIAA Journal*, **22**(6):797–800.
- DIMOTAKIS, P. E. AND J. L. HALL. 1987. A simple model for finite chemical kinetics analysis of supersonic turbulent shear layer combustion. *AIAA/SAE/ASME/ASEE 23rd Joint Propulsion Conference*. AIAA 1987-1879.
- DOLVIN, D. 2008. Hypersonic international flight research and experimentation (HiFiRE). *15th AIAA International Space Planes and Hypersonic Systems and Technologies Conference*. AIAA 2008-2581.
- DRUMMOND, L. 1968. Shock-initiated exothermic reactions V. The oxidation of ethylene. *Australian Journal of Chemistry*, **21**(11):2641–2648.
- EGOLFOPOULOS, F. N., P. E. DIMOTAKIS, AND C. BOND. 1996. On strained flames with hypergolic reactants: The  $\text{H}_2/\text{NO}/\text{F}_2$  system in high-speed, supersonic and subsonic mixing-layer combustion. *Proceedings of the Symposium (International) on Combustion*, **26**(2):2885–2893.
- GAMBA, M., V. A. MILLER, M. G. MUNGAL, AND R. K. HANSON. 2015. Temperature and number density measurement in non-uniform supersonic flowfields undergoing mixing using toluene PLIF thermometry. *Applied Physics B*, **120**(2):285–304.
- GAMBA, M. AND M. G. MUNGAL. 2015a. Ignition, flame structure and near-wall burning in transverse hydrogen jets in supersonic crossflow. *Journal of Fluid Mechanics*, **780**:226–273.
- GAY, I., G. GLASS, R. KERN, AND G. KISTIAKOWSKY. 1967. Ethylene Oxygen reaction in shock waves. *Journal of Chemical Physics*, **47**(1):313–320.

- GAYDON, A. AND H. WOLFARD. 1970. *Flames: Their Structure, Radiation and Properties*. Chapman and Hall, London.
- GILBRECH, R. J. 1991. *An experimental investigation of chemically-reacting, gas-phase turbulent jets*. Ph.D. thesis, California Institute of Technology.
- GOEBEL, S. G. AND J. C. DUTTON. 1991. Experimental study of compressible turbulent mixing layers. *AIAA Journal*, **29**(4):538–546.
- GOLDEN, G. 2000. GRI Mech 3.0. ([http://www.me.berkeley.edu/gri\\_mech/](http://www.me.berkeley.edu/gri_mech/)).
- GOODWIN, D. 2005. Cantera object-oriented software for reacting flows. (<http://www.cantera.org>).
- GÖTTGENS, J., F. MAUSS, AND N. PETERS. 1992. Analytic approximations of burning velocities and flame thicknesses of lean hydrogen, methane, ethylene, ethane, acetylene, and propane flames. *Symposium (International) on Combustion*, **24**(1):129–135.
- GRUBER, M., A. NEJAD, T. CHEN, AND J. DUTTON. 1997a. Compressibility effects in supersonic transverse injection flowfields. *Physics of Fluids*, **9**(5):1448–1461.
- GRUBER, M., A. NEJAD, T. CHEN, AND J. DUTTON. 1997b. Large structure convection velocity measurements in compressible transverse injection flowfields. *Experiments in Fluids*, **22**(5):397–407.
- GRUBER, M., A. NEJADT, T. CHEN, AND J. DUTTON. 1995. Mixing and penetration studies of sonic jets in a Mach 2 freestream. *Journal of Propulsion and Power*, **11**(2):315–323.
- GRUENIG, C. AND F. MAYINGER. 1999. Supersonic combustion of kerosene/H<sub>2</sub>-mixtures in a model scramjet combustor. *Combustion Science and Technology*, **146**(1-6):1–22.
- HALL, J., M. RICKARD, AND E. PETERSEN. 2005. Comparison of characteristic time diagnostics for ignition and oxidation of fuel/oxidizer mixtures behind reflected shock waves. *Combustion Science and Technology*, **177**(3):455–483.
- HALL, J. L. 1991. *An experimental investigation of structure, mixing and combustion in compressible turbulent shear layers*. Ph.D. thesis, California Institute of Technology.
- HANK, J. M., J. S. MURPHY, AND R. C. MUTZMAN. 2008. The X-51A scramjet engine flight demonstration program. *15th AIAA International Space Planes and Hypersonic Systems and Technologies Conference*. AIAA 2540-2008.

- HASSELBRINK, E. AND M. MUNGAL. 2001. Transverse jets and jet flames. Part 1. Scaling laws for strong transverse jets. *Journal of Fluid Mechanics*, **443**:1–25.
- HAVEN, B. AND M. KUROSAKA. 1997. Kidney and anti-kidney vortices in crossflow jets. *Journal of Fluid Mechanics*, **352**:27–64.
- HEISER, W., W. MCCLURE, AND C. WOOD. 1996. Simulating heat addition via mass addition in variable area compressible flows. *AIAA Journal*, **34**(5):1076–1078.
- HEISER, W. H. AND D. T. PRATT. 1994. *Hypersonic airbreathing propulsion*. AIAA, Washington, DC.
- HELTSLEY, W. N., J. A. SNYDER, C. C. CHEUNG, M. MUNGAL, AND R. K. HANSON. 2007. Combustion stability regimes of hydrogen jets in supersonic crossflow. *43rd AIAA/ASME/SAE/ASEE Joint Propulsion Conference and Exhibit, Joint Propulsion Conference*. AIAA 2007-5401.
- HERMANSON, J. 1985. *Heat release effects in a turbulent, reacting shear layer*. Ph.D. thesis, California Institute of Technology.
- HIDAKA, Y., T. KATAOKA, AND M. SUGA. 1974. A shock-tube investigation of ignition in ethylene–oxygen–argon mixtures. *Bulletin of the Chemical Society of Japan*, **47**(9):2166–2170.
- HOMER, J. B. AND G. KISTIAKOWSKY. 1967. Oxidation and pyrolysis of ethylene in shock waves. *The Journal of Chemical Physics*, **47**(12):5290–5295.
- HORNING, D. 2001. A study of the high-temperature auto-ignition and thermal decomposition of hydrocarbons. Report no. TSD-135.
- IBARAKI, T., I. KUSUNOKI, AND K. KODERA. 1972. Study of chemiluminescence by means of crossed beams: nitric oxide–oxygen atom system. *Chemistry Letters*, (4):309–312.
- INGENITO, A. AND C. BRUNO. 2010. Physics and regimes of supersonic combustion. *AIAA Journal*, **48**(3):515–525.
- JACHIMOWSKI, C. J. 1977. An experimental and analytical study of acetylene and ethylene oxidation behind shock waves. *Combustion and Flame*, **29**:55–66.
- JOHNSTON, H. S. AND H. J. BERTIN. 1959. Absorption and emission spectra of nitrosyl fluoride. *Journal of Molecular Spectroscopy*, **3**(1):683–696.

- JONASSEN, D. R., G. S. SETTLES, AND M. D. TRONOSKY. 2006. Schlieren PIV for turbulent flows. *Optics and Lasers in Engineering*, **44**(3):190–207.
- KALITAN, D. M., J. M. HALL, AND E. L. PETERSEN. 2005. Ignition and oxidation of ethylene-oxygen-diluent mixtures with and without silane. *Journal of Propulsion and Power*, **21**(6):1045–1056.
- KONRAD, J. H. 1977. *An experimental investigation of mixing in two-dimensional turbulent shear flows with applications to diffusion-limited chemical reactions*. Ph.D. thesis, California Institute of Technology.
- KOOCHESFAHANI, M. AND P. E. DIMOTAKIS. 1986. Mixing and chemical reactions in a turbulent liquid mixing layer. *Journal of Fluid Mechanics*, **170**:83–112.
- KOPP, M. M., N. S. DONATO, E. L. PETERSEN, W. K. METCALFE, S. M. BURKE, AND H. J. CURRAN. 2014. Oxidation of ethylene–air mixtures at elevated pressures. Part 1: Experimental results. *Journal of Propulsion and Power*, **30**(3):790–798.
- LANDAU, L. AND E. LIFSHITZ. 1989. *Fluid Mechanics*. Pergamon Press, New York, NY.
- LASKIN, A., H. WANG, AND C. K. LAW. 2000. Detailed kinetic modeling of 1, 3-butadiene oxidation at high temperatures. *International Journal of Chemical Kinetics*, **32**(10):589–614.
- LAW, C. K. 2010. *Combustion Physics*. Cambridge University Press, New York.
- LEE, M., B. McMILLIN, J. PALMER, AND R. HANSON. 1991. Two-dimensional imaging of combustion phenomena in a shock tube using planar laser-induced fluorescence. *29th Aerospace Sciences Meeting*. AIAA 1991-0460.
- LIN, K.-C., M. RYAN, C. CARTER, M. GRUBER, AND C. RAFFOUL. 2010. Raman scattering measurements of gaseous ethylene jets in a Mach 2 supersonic crossflow. *Journal of Propulsion and Power*, **26**(3):503–513.
- LUTHMAN, E., N. CYMBALIST, D. LANG, AND P. E. DIMOTAKIS. 2016. Artificial schlieren of high-speed flows using geometric optics. *In preparation*.
- MAHESH, K. 2013. The interaction of jets with crossflow. *Annual Review of Fluid Mechanics*, **45**:379–407.

- MARINOV, N. M., W. J. PITZ, C. K. WESTBROOK, A. M. VINCITORE, M. J. CASTALDI, S. M. SENKAN, AND C. F. MELIUS. 1998. Aromatic and polycyclic aromatic hydrocarbon formation in a laminar premixed n-butane flame. *Combustion and Flame*, **114**(1):192–213.
- MATHUR, T., M. GRUBER, K. JACKSON, J. DONBAR, W. DONALDSON, T. JACKSON, AND F. BILLIG. 2001. Supersonic combustion experiments with a cavity-based fuel injector. *Journal of Propulsion and Power*, **17**(6):1305–1312.
- MCCANN, G. J. AND R. D. BOWERSOX. 1996. Experimental investigation of supersonic gaseous injection into a supersonic freestream. *AIAA Journal*, **34**(2):317–323.
- MCDANIEL, J. AND J. RAVES. 1988. Laser-induced-fluorescence visualization of transverse gaseous injection in a nonreacting supersonic combustor. *Journal of Propulsion and Power*, **4**(6):591–597.
- MEINHART, C. D., S. T. WERELEY, AND J. G. SANTIAGO. 2000. A PIV algorithm for estimating time-averaged velocity fields. *Journal of Fluids Engineering*, **122**(2):285–289.
- MICKA, D. J. AND J. F. DRISCOLL. 2012. Stratified jet flames in a heated (1390K) air cross-flow with autoignition. *Combustion and Flame*, **159**(3):1205–1214.
- MUNGAL, M. AND P. E. DIMOTAKIS. 1984. Mixing and combustion with low heat release in a turbulent shear layer. *Journal of Fluid Mechanics*, **148**:349–382.
- MUNGAL, M. AND C. FRIELER. 1988. The effects of Damköhler number in a turbulent shear layer. *Combustion and Flame*, **71**(1):23–34.
- MUNGAL, M. G. 1983. *Experiments on mixing and combustion with low heat release in a turbulent shear flow*. Ph.D. thesis, California Institute of Technology.
- NAKAYA, S., Y. HIKICHI, Y. NAKAZAWA, K. SAKAKI, M. CHOI, M. TSUE, M. KONO, AND S. TOMIOKA. 2015b. Ignition and supersonic combustion behavior of liquid ethanol in a scramjet model combustor with cavity flame holder. *Proceedings of the Combustion Institute*, **35**(2):2091–2099.
- NAKAYA, S., M. TSUE, M. KONO, O. IMAMURA, AND S. TOMIOKA. 2015. Effects of thermally cracked component of n-dodecane on supersonic combustion behaviors in a scramjet model combustor. *Combustion and Flame*, **162**(10):3847–3853.

- PENYAZKOV, O., K. SEVROUK, V. TANGIRALA, AND N. JOSHI. 2009. High-pressure ethylene oxidation behind reflected shock waves. *Proceedings of the Combustion Institute*, **32**(2):2421–2428.
- PETERS, N. 1988. Laminar flamelet concepts in turbulent combustion. *Proceedings of the Symposium (International) on Combustion*, **21**(1):1231–1250.
- PETERS, N. 1999. The turbulent burning velocity for large-scale and small-scale turbulence. *Journal of Fluid Mechanics*, **384**:107–132.
- PIERCE, C. D. AND P. MOIN. 2004. Progress-variable approach for large-eddy simulation of non-premixed turbulent combustion. *Journal of Fluid Mechanics*, **504**:73–97.
- PITSCH, H. 2000. Unsteady flamelet modeling of differential diffusion in turbulent jet diffusion flames. *Combustion and Flame*, **123**(3):358–374.
- POINSOT, T. AND D. VEYNANTE. 2005. *Theoretical and Numerical Combustion*. RT Edwards, Philadelphia, PA.
- POPE, S. B. 2004. Ten questions concerning the large-eddy simulation of turbulent flows. *New Journal of Physics*, **6**(1):35.
- RANZI, E., A. FRASSOLDATI, R. GRANA, A. CUOCI, T. FARAVELLI, A. KELLEY, AND C. LAW. 2012. Hierarchical and comparative kinetic modeling of laminar flame speeds of hydrocarbon and oxygenated fuels. *Progress in Energy and Combustion Science*, **38**(4):468–501.
- RAPP, D. AND H. S. JOHNSTON. 1960. Nitric oxide-fluorine dilute diffusion flame. *The Journal of Chemical Physics*, **33**(3):695–699.
- ROGERS, R. C. 1971. A study of the mixing of hydrogen injected normal to a supersonic airstream. *NASA Rep. TN-D6114*.
- ROTHSTEIN, A. D. 1992. *A study of the normal injection of hydrogen into a heated supersonic flow using planar laser-induced fluorescence*. Master's thesis, Massachusetts Institute of Technology, Department of Aeronautics and Astronautics.
- ROUDAKOV, A. S., V. L. SEMENOV, V. I. KOPCHENOV, AND J. W. HICKS. 1996. Future flight test plans of an axisymmetric hydrogen-fueled scramjet engine on the hypersonic flying laboratory. *7th International Spaceplanes and Hypersonics Systems and Technology Conference*. AIAA 1996-4572.

- SABELNIKOV, V., B. DESHAIES, AND L. F. F. DA SILVA. 1998. Revisited flamelet model for nonpremixed combustion in supersonic turbulent flows. *Combustion and Flame*, **114**(3):577–584.
- SAGHAFIAN, A., V. E. TERRAPON, AND H. PITSCH. 2015. An efficient flamelet-based combustion model for compressible flows. *Combustion and Flame*, **162**(3):652–667.
- SANTIAGO, J. G. AND J. C. DUTTON. 1997. Velocity measurements of a jet injected into a supersonic crossflow. *Journal of Propulsion and Power*, **13**(2):264–273.
- SAXENA, S., M. KAHANDAWALA, AND S. S. SIDHU. 2011. A shock tube study of ignition delay in the combustion of ethylene. *Combustion and Flame*, **158**(6):1019–1031.
- SCHETZ, J. AND F. BILLIG. 1966. Penetration of gaseous jets injected into a supersonic stream. *Journal of Spacecraft and Rockets*, **3**(11):1658–1665.
- SCHETZ, J. A., L. MADDALENA, AND S. K. BURGER. 2010. Molecular weight and shock-wave effects on transverse injection in supersonic flow. *Journal of Propulsion and Power*, **26**(5):1102–1113.
- SCHULTZ, E. AND J. SHEPHERD. 2000. Validation of detailed reaction mechanisms for detonation simulation. *Explosion Dynamics Laboratory Report FM99-5*.
- SETTLES, G. S. 2001. *Schlieren and shadowgraph techniques: visualizing phenomena in transparent media*. Springer, New York.
- SHAPIRO, A. H. 1953. *The dynamics and thermodynamics of compressible fluid flow*, volume 1. Ronald Press, New York.
- SKOLNIK, E. G., S. W. VEYSEY, M. G. AHMED, AND W. E. JONES. 1975. Rate constants for the reaction of fluorine atoms with nitric oxide in the presence of various third bodies. *Canadian Journal of Chemistry*, **53**(21):3188–3193.
- SLESSOR, M. D. 1998. *Aspects of turbulent-shear-layer dynamics and mixing*. Ph.D. thesis, California Institute of Technology.
- SUZUKI, M., T. MORIWAKI, S. OKAZAKI, T. OKUDA, AND T. TANZAWA. 1973. Oxidation of ethylene in shock tube. *Astronautica Acta*, **18**:359–365.
- TERRAPON, V., F. HAM, R. PECNIK, AND H. PITSCH. 2009. A flamelet-based model for supersonic combustion. *Stanford CTR Annual Research Briefs*, pages 47–58.

- UCSD. 2012. Chemical-kinetic mechanisms for combustion applications. San Diego Mechanism web page, Mechanical and Aerospace Engineering (Combustion Research). (<http://combustion.ucsd.edu>).
- VAN OIJEN, J. AND L. DE GOEY. 2002. Modelling of premixed counterflow flames using the flamelet-generated manifold method. *Combustion Theory and Modelling*, **6**(3):463–478.
- VANLERBERGHE, W. M., J. G. SANTIAGO, J. C. DUTTON, AND R. P. LUCHT. 2000. Mixing of a sonic transverse jet injected into a supersonic flow. *AIAA Journal*, **38**(3):470–479.
- WANG, H. 2007. USC Mech version II. High-temperature combustion reaction model of H<sub>2</sub>/CO/C<sub>1</sub>-C<sub>4</sub> compounds. (<http://ignis.usc.edu>).
- WANG, H. 2010. A high-temperature chemical kinetic model of n-alkane (up to n-dodecane), cyclohexane, and methyl-, ethyl-, n-propyl and n-butyl-cyclohexane oxidation at high temperatures, JetSurF version 2.0. (<http://web.stanford.edu/group/haiwanglab/JetSurF/JetSurF2.0/index.html>).
- WANG, H., F. SHAN, Y. PIAO, L. HOU, AND J. NIU. 2015. IDDES simulation of hydrogen-fueled supersonic combustion using flamelet modeling. *International Journal of Hydrogen Energy*, **40**(1):683–691.
- WILLIAMS, F. 1970. Atomization processes and ignition criteria for supersonic combustion with liquid fuel injection. *Astronautica Acta*, **15**(5-6):547–557.
- WILLIAMS, F. 1985. *Combustion Theory, 2nd Ed.* Westview Press, Boulder, CO.
- XU, C. AND A. A. KONNOV. 2012. Validation and analysis of detailed kinetic models for ethylene combustion. *Energy*, **43**(1):19–29.
- ZHOU, B., C. BRACKMANN, Z. LI, M. ALDÉN, AND X.-S. BAI. 2015. Simultaneous multi-species and temperature visualization of premixed flames in the distributed reaction zone regime. *Proceedings of the Combustion Institute*, **35**(2):1409–1416.

# Appendices

## Appendix A

# Schlieren image-correlation velocimetry (SICV)

Extracting convective velocity from multiple image pairs occurs in two steps. First, the images are processed to partially suppress quasi-stationary structures, including shocks and expansions (shown in Fig. A.1, center), and background patterns including fringe patterns from the contact surface of the BK7 glass and Pyrex sheets. The mean intensity of a sequence of  $N$  images,  $\bar{\mathbf{I}}$ , is subtracted from the individual intensity fields from a pair,  $\mathbf{I}_{A,n}$  and  $\mathbf{I}_{B,n}$ , where  $n$  is the index of an image pair in a sequence, i.e.,

$$\tilde{\mathbf{I}}_{[A,B],n} = \mathbf{I}_{[A,B],n} - \bar{\mathbf{I}}, \quad (\text{A.1})$$

where,

$$\bar{\mathbf{I}} = \frac{1}{2N} \sum_{n=1}^N (\mathbf{I}_{A,n} + \mathbf{I}_{B,n}), \quad (\text{A.2})$$

producing image pairs with suppressed stationary structures, as shown in Fig. A.1.

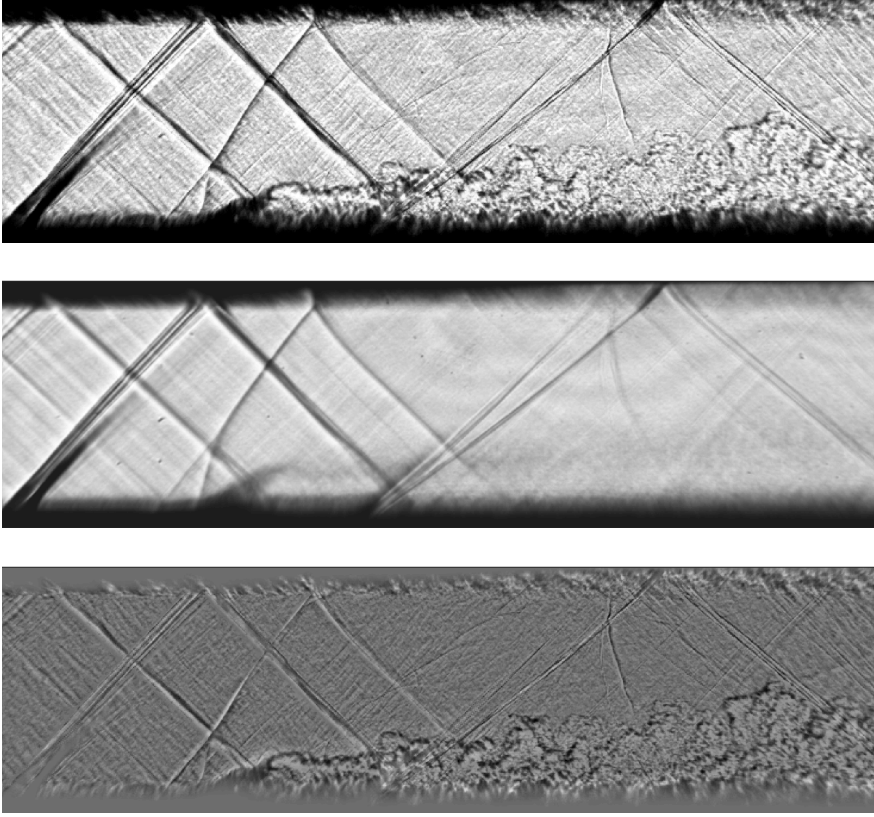


Figure A.1: Representative  $\mathbf{I}_{A,n}$  (top),  $\bar{\mathbf{I}}$  (middle), and  $\tilde{\mathbf{I}}_{A,n}$  (bottom)

Next, sets of  $N$  image-pairs undergo a frame-averaged cross-correlation to determine the time-averaged displacement of coherent structures, and the convective-velocity field.

In a typical single-frame cross-correlation, the displacement at some point is determined by extracting a reduced-size tile  $\mathbf{A}$  from the intensity map  $\mathbf{I}_A$  and a template  $\mathbf{B}$  from the intensity map  $\mathbf{I}_B$ , and cross correlating. The displacement of the  $L \times M$  matrix  $\mathbf{A}$  with respect to the  $P \times Q$  template  $\mathbf{B}$  can be determined from the  $(L + P - 1) \times (M + Q - 1)$  cross-correlation matrix  $\mathbf{C}$ ,

$$\mathbf{C}(i, j) = \sum_{l=0}^{L-1} \sum_{m=0}^{M-1} \mathbf{A}(l, m) \mathbf{B}(l - i, m - j), \quad (\text{A.3})$$

where  $-(P - 1) \leq i \leq L - 1$  and  $-(Q - 1) \leq j \leq M - 1$ . If the cross-correlation signal peak is

strong and well defined, the index of the peak in  $\mathbf{C}$  gives the displacement of matrix  $\mathbf{A}$  with respect to matrix  $\mathbf{B}$ .

If the peak is weak or poorly defined, the location of the peak loses significance, and can produce spurious displacement vectors. This typically occurs if there is no detectable pattern shift between the A and B matrices. In the context of image-correlation velocimetry based on convected turbulent structures, this problem occurs if the structures in the flow are sparse, i.e., if there exist regions in the flow that, instantaneously, do not contain traceable structures. In this case, a frame-averaged cross-correlation approach can be used to determine the mean (time-averaged) convective velocity. To extract the time-averaged convective velocity field, multiple ( $N$ ) image pairs are captured over some period where the flow is statistically steady during that period.

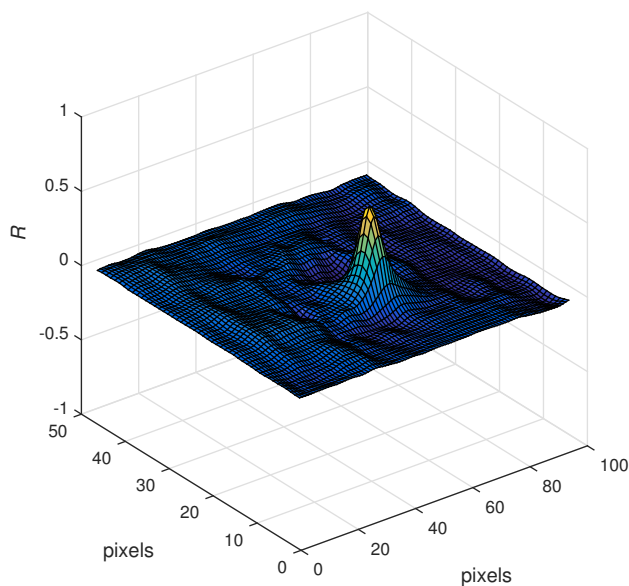


Figure A.2: Average cross-correlation signal  $\bar{C}$  at a location in the jet wake region produced with 32 image pairs.  $x$  and  $y$  axes have units of pixels, while the  $z$  axis is the normalized cross-correlation coefficient,  $R$ , that ranges from -1 to 1

To determine the mean displacement from a set of  $N$  pairs of images, a reduced-size tile  $\mathbf{A}_N$  is extracted from the set of  $I_{A,N}$ , and template  $\mathbf{B}_N$  is from the set of  $I_{B,N}$ . The mean displacement

of the  $L \times M \times N$  matrix  $\mathbf{A}_N$  with respect to the  $P \times Q \times N$  template  $\mathbf{B}_N$  is determined from the  $L + P - 1$  by  $M + Q - 1$  average cross-correlation matrix  $\bar{\mathbf{C}}$ ,

$$\bar{\mathbf{C}}(i, j) = \frac{1}{N} \sum_{n=1}^N \sum_{l=0}^{L-1} \sum_{m=0}^{M-1} \mathbf{A}(l, m, n) \mathbf{B}(l - i, m - j, n) . \quad (\text{A.4})$$

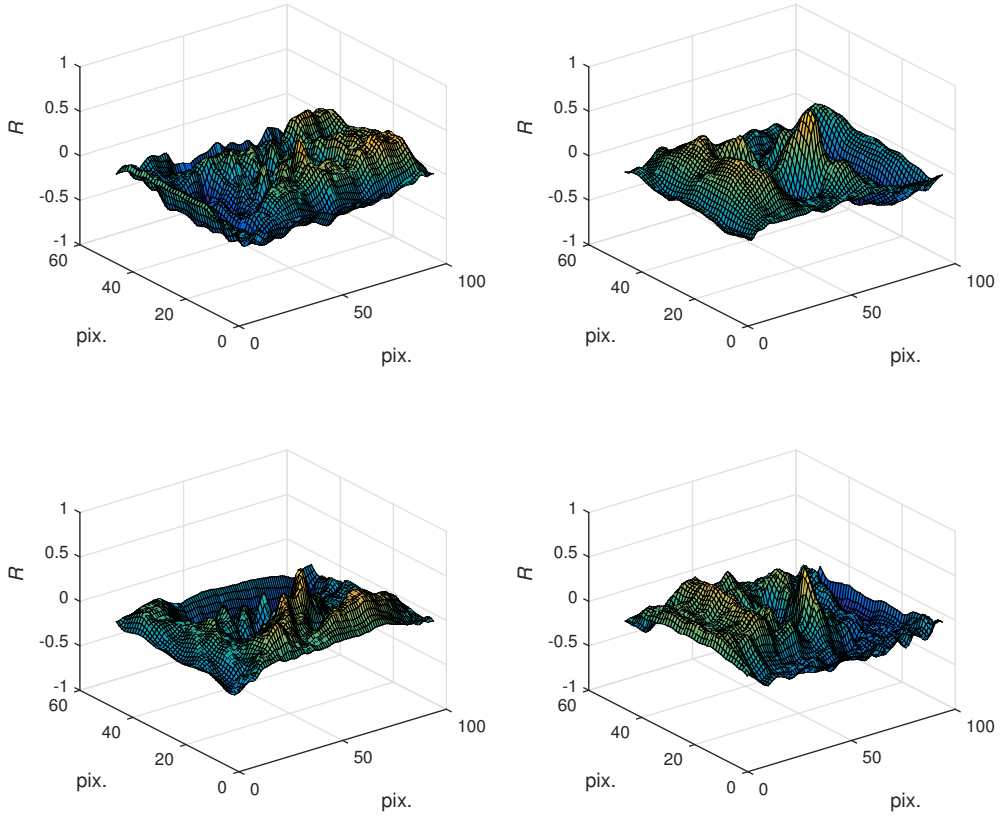


Figure A.3: Four randomly selected sample individual cross-correlation signals  $\mathbf{C}_n$ .  $x$  and  $y$  axes have units of pixels, while the  $z$  axis is the normalized cross-correlation coefficient,  $R$ , that ranges from -1 to 1

The resulting average cross-correlation signal  $\bar{\mathbf{C}}$  is considerably stronger and better-defined than

the individual cross-correlation signals,  $\mathbf{C}_n$ , that are averaged to generate  $\bar{\mathbf{C}}$ . As an example, Fig. A.2 shows the average cross-correlation signal at a location in the jet wake region produced with  $N = 32$  image pairs, while Fig. A.3 shows four (randomly-selected) individual cross-correlation signals,  $\mathbf{C}_n$ , that were averaged (with 28 others, not shown) to produce  $\bar{\mathbf{C}}$ .  $\bar{\mathbf{C}}$  has a strong, distinct peak that can be used to produce reliable displacement vectors, even though the peaks in  $\mathbf{C}_n$  are not strong or distinct enough to produce reliable displacement information, individually.

The location of the correlation peak in the resulting average cross-correlation matrix  $\bar{\mathbf{C}}$  gives the average displacement of tile  $\mathbf{A}_N$  with respect to template  $\mathbf{B}_N$ . Sub-pixel accuracy is obtained by fitting a third-order polynomial to the region around the peak and using the resulting functions' maximum value to correct the displacement vector.

The size of the  $\mathbf{A}_N$  tile,  $\mathbf{B}_N$  template, and the number of images ( $N$ ) used to extract the time-averaged signal depends on the flow, image resolution and quality, and image-pair spacing. For this particular flow,  $[32 \times 16]$  sized tiles and  $[64 \times 32]$  sized templates were extracted from  $N = 32$  image pairs. The tile and template sizes were selected based on typical large-structure displacement between images, and the number of frames sampled was selected to restrict the time averaging to approximately 25 ms.

To obtain convective-velocity field data, processed image-pair sets  $\tilde{\mathbf{I}}_{[A,B],n \in N}$  are sampled randomly for template-tile pair sets to generate average cross-correlation signals. Signals whose peak meets a minimum threshold, defined by a fraction of the average peak signal in the domain, are used to generate a displacement vector.

The SICV method illustrated above and in Ch. 3 can be used to non-intrusively estimate time-averaged convective velocity fields in high-speed flows using sets of image pairs that would not otherwise produce reliable velocity data. The method is broadly applicable to flows with convected refractive-index interfaces resulting from mixing or combustion, for example.

## Appendix B

# Nitrosyl fluoride (NOF) and nitroxyl (HNO) chemiluminescence

The reaction of fluorine atoms (F) with nitric oxide (NO) in the presence of a third body (M) produces nitrosyl fluoride (FNO) in both ground and excited states (Skolnik et al. 1975). The electronically-excited nitrosyl fluoride molecules decay to their ground state by non-radiative and radiative processes. The latter produce emissions in the visible, between 640 and 510 nm, with a peak at 609.5 nm (Johnston and Bertin 1959). The process is represented by the following reactions:



where  $h\nu$  represents an emitted photon. These rate constants are, for the most part, unknown. However, the intensity of emission is directly proportional to the concentration of FNO\* (concentration is denoted here by square brackets, [...]). Assuming steady-state conditions for [FNO\*],

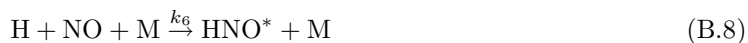
$$\frac{d[\text{FNO}^*]}{dt} = [\text{NO}][\text{F}][\text{M}]k_2 - [\text{FNO}^*]k_3 - [\text{FNO}^*][\text{M}]k_4 \simeq 0 , \quad (\text{B.5})$$

demonstrates that the intensity of the FNO\* chemiluminescence,  $I_{\text{FNO}}$ , is proportional to the concentration of atomic fluorine,

$$I_{\text{FNO}} \propto [\text{FNO}^*] = \frac{k_2[\text{NO}][\text{M}]}{k_3 + [\text{M}]k_4} [\text{F}] . \quad (\text{B.6})$$

Therefore, the chemiluminescence intensity can be estimated using the concentration of atomic fluorine alone, that can be obtained using a reduced F+NO+H<sub>2</sub> mechanism, such as that listed in Hall (1991), shown in Table B.1, for example.

The mechanism that describes HNO\* chemiluminescence is similar to that describing FNO\* (Clyne and Thrush 1962). The process is represented by the following reactions:



and, assuming steady-state conditions for [HNO\*],

$$I_{\text{HNO}} \propto [\text{HNO}^*] = \frac{k_6[\text{NO}][\text{M}]}{k_7 + [\text{M}]k_8} [\text{H}] . \quad (\text{B.11})$$

As is the case with FNO\* chemiluminescence, the intensity of HNO\* depends on the concentration of atomic hydrogen, and can be estimated using a reduced kinetic mechanism (e.g., Hall 1991, Table 2.1), shown in Table B.1. Units are cm, s, and cal/mol for the activation energy, E.

Table B.1: Hydrogen-fluorine chemical-kinetic mechanism

Reaction	A	b	E
$\text{NO} + \text{F}_2 \leftrightarrow \text{NOF} + \text{F}$	4.2E+11	0	2285
$\text{NO} + \text{F} + \text{M} \leftrightarrow \text{NOF} + \text{M}$	3.0E+16	0	0
$\text{H} + \text{F}_2 \leftrightarrow \text{HF} + \text{F}$	3.0E+9	1.5	1680
$\text{F} + \text{H}_2 \leftrightarrow \text{HF} + \text{H}$	2.6E+12	0.5	610
$\text{F}_2 + \text{M} \leftrightarrow \text{F} + \text{F} + \text{M}$	2.12E+13	0	33720
$\text{H} + \text{F} + \text{M} \leftrightarrow \text{HF} + \text{M}$	7.5E+18	-1.0	0
$\text{H} + \text{H} + \text{M} \leftrightarrow \text{H}_2 + \text{M}$	6.4E+17	-1.0	0
$\text{H} + \text{NO} + \text{M} \leftrightarrow \text{HNO} + \text{M}$	5.4E+15	0	-302
$\text{H} + \text{HNO} \leftrightarrow \text{NO} + \text{H}_2$	4.8E+12	0	0

An intensity-response curve for the chemiluminescence system was obtained using a constant light source and a set of neutral-density (ND) filters. A quasi-constant LED light source, modulated by a set of ND filters with known transmittance, was captured using the intensified-chemiluminescence system in the intensity range of interest. The recovered intensity was plotted against each ND filter (and filter combination) transmittance, Figure B.1. The  $x$  axis is the normalized applied intensity modulated by the ND filter, and the  $y$  axis is the normalized measured intensity. The curve shows that the chemiluminescence measurement system has a quasi-linear response in the range of interest.

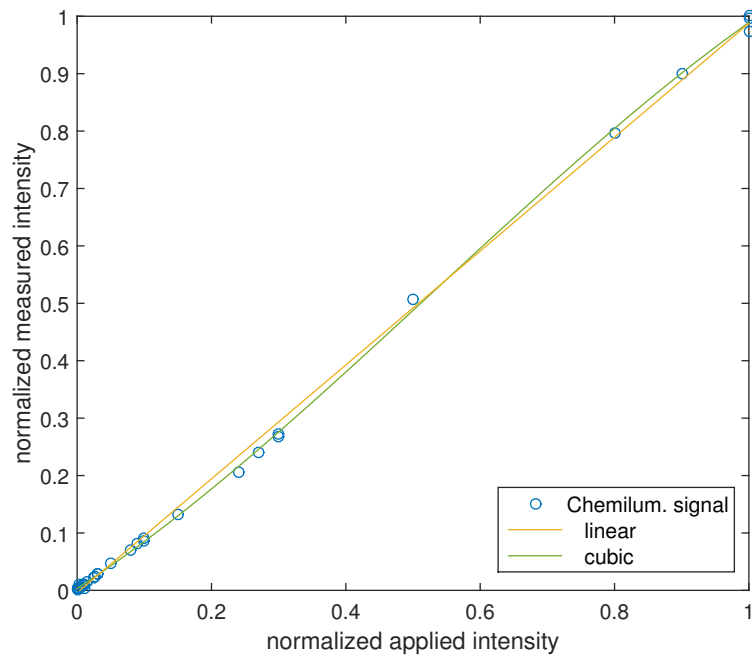


Figure B.1: Chemiluminescence system calibration curve illustrating a quasi-linear response. The  $x$ -axis is the normalized applied intensity, and the  $y$ -axis is the normalized measured intensity.

## Appendix C

# Detailed chemical kinetics assessment

To illustrate and assess the predictive capability for induction modeling, ethylene-ignition simulations using a selection of state-of-the-art and heritage detailed chemical-kinetic mechanisms (Table 4.2) are compared to a set of experimental ethylene ignition-delay times (Table 4.3). The results help assess the variance between experimental ignition-delay data and ignition-delay times predicted by detailed chemical kinetics as a function of conditions during induction. The mechanisms in Table 4.2 are intended to also describe ethylene ignition, with the exception of GRI-Mech-3.0 that is included here for reference only. While this list is not exhaustive, it is representative of detailed chemical-kinetic mechanisms for simple hydrocarbons developed over the past two decades.

A systematic variance between sets of shock-tube experiments can arise from differences in shock-tube geometry, other experimental details, and ignition-delay definition, and is expected. Differences attributable to the choice of ignition marker are estimated to be in the range of 2%-5% at lower temperatures (Davidson and Hanson 2004, Hall et al. 2005), as also shown in Figure C.1, and up to 20% at higher temperatures ( $T_0 > 1600$  K). Various boundary-layer effects in smaller-diameter shock-tubes may affect apparent activation-energy estimates by up to 20% for experiments with conditions resulting in very long ignition delays ( $t_d > 2$  ms). For shorter ignition delays ( $t_d < 500$   $\mu$ s), activation-energy estimates can be expected to be within 5%.

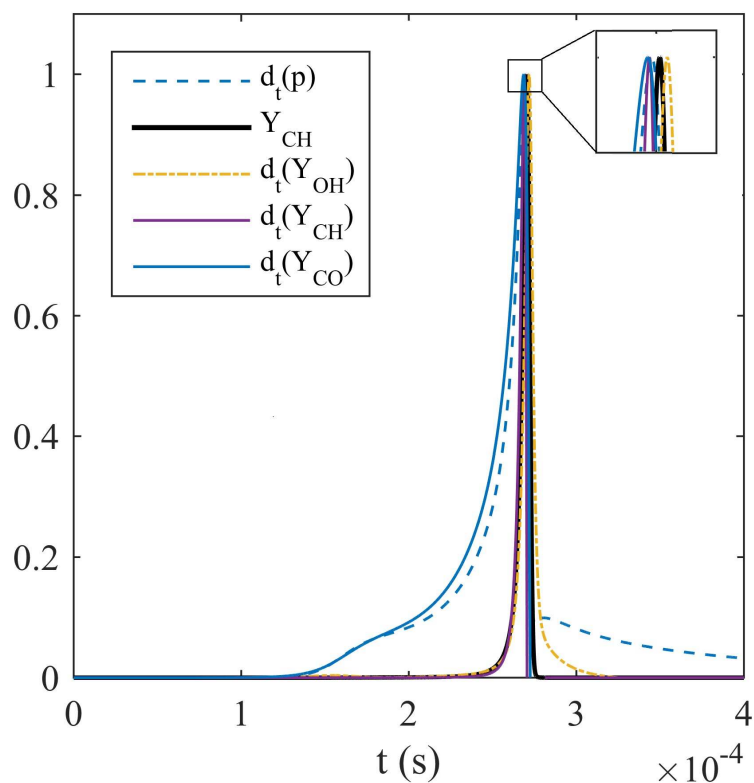


Figure C.1: Comparison of various potential ignition criteria

To a first approximation, ignition of a fuel-oxidizer-diluent mixture in a shock tube can be modeled as a constant-volume homogeneous reactor with an initial pressure and temperature set to those behind the reflected shock, i.e., by ignoring any chemical activity at the lower pressure and temperature prior to shock reflection. A higher-fidelity description would account for spatial and temporal variations in the post-shock mixture conditions caused by boundary-layer effects, and pressure increases after the reflected shock but prior to ignition, for mixtures with particularly long ( $\sim 1$  ms) induction periods. Such higher-fidelity models, however, require more information than is typically provided in shock-tube ignition-delay studies and their use is generally reserved for simulating individual shock-tube experiments with greater parametric detail, e.g., parameterizing the effects of shock-tube diameter. Schultz and Shepherd (2000) and Xu and Konnov (2012) use the simpler first-order approach, which is also adopted in this study.

The species and energy conservation equations for a constant volume and mass reactor are given by,

$$\rho \frac{dY_\alpha}{dt} = \dot{\omega}_\alpha , \quad (\text{C.1a})$$

$$\rho c_v \frac{dT}{dt} = \sum_\alpha e_\alpha \dot{\omega}_\alpha , \quad (\text{C.1b})$$

where  $Y_\alpha$ ,  $e_\alpha$ , and  $\dot{\omega}_\alpha$  are the mass fraction, internal energy, and source term of the  $\alpha$  species, respectively, and are solved using the Cantera software package (Goodwin 2005). Ignition onset is defined here as the time of maximum CH concentration. Figure C.1 shows the normalized positive time rate of change,  $d_t(\cdot)$ , of the OH, CH, CO mass fractions, and pressure, and the CH mass fraction as a function of time. These are computed for a constant-volume reactor with an initial temperature and pressure of  $T_0 = 1250$  K and 1 bar, respectively, and an initial composition of  $Y_{\text{Ar}} = 0.92$ ,  $Y_{\text{O}_2} = 0.06$ ,  $Y_{\text{C}_2\text{H}_4} = 0.02$ . The time of maximum CH mass fraction is very close to the time of maximum (positive) rate of change of quantities and species whose luminescence (estimated as proportional to the species time rate of change) is used as the ignition criterion in the experimental ignition datasets in Table 4.3, justifying the use of  $Y_{\text{CH,max}}$  as the ignition criterion.

The logarithmic variance between each experimental ignition-delay time and the corresponding ignition-delay time calculated with a homogeneous, constant-volume reactor using each of the mechanisms in Table 4.2 is defined as

$$r_{\log} = \log_{10} \left( \frac{t_{\text{d,sim}}}{t_{\text{d,exp}}} \right) . \quad (\text{C.2})$$

Only the experiments that were determined to be consistent with the bulk of the data (cf. Section 4.3.3) were used in the comparison. The (binned) moving average of the variance is plotted in Fig. C.2 (state-of-the-art mechanisms) and Fig. C.3 (heritage mechanisms) against initial-mixture temperature. The large variance between experiment and predictions obtained using chemical-kinetic simulations is evident and well-known, particularly at lower temperatures. More-recent mechanisms (USC, JET, SD, and RNZ) perform better than the older mechanisms at initial mixture temperatures around 1100 K. The variance of the proposed EVM method with respect to experimental data is, overall, less than that of detailed chemical kinetic mechanisms.

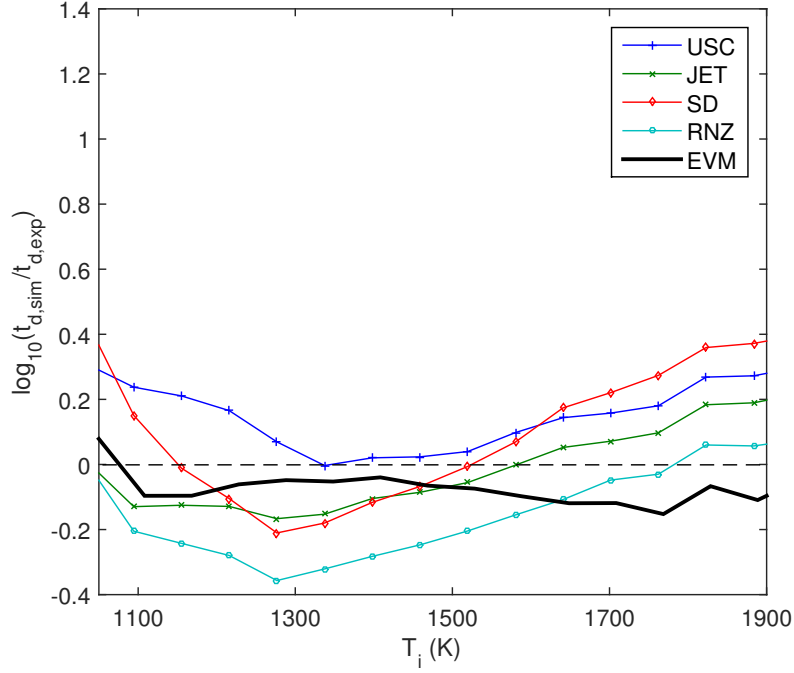


Figure C.2: Logarithmic variance between recent chemical-kinetics mechanisms and experimental ignition-delay data plotted as a function of initial mixture temperature. The thick black line represents the variance between the proposed EVM method and experimental data.

In terms of the mean variance,

$$\bar{r} = \frac{1}{N_{\text{exp}}} \sum_{n=1}^{N_{\text{exp}}} \left( \frac{t_{d,\text{sim}} - t_{d,\text{exp}}}{t_{d,\text{exp}}} \right)_n, \quad (\text{C.3})$$

where  $N_{\text{exp}}$  is the total number of experimental data points, recent mechanisms perform better than older ones, as also seen in Fig. C.4. RNZ and JET are the two largest mechanisms in terms of number of species and reactions, indicating that increased reaction-pathway resolution can improve overall accuracy. All mechanisms perform better at fuel-rich conditions than at stoichiometric conditions. Predicting ignition-delay in lean conditions challenges most mechanisms, with the exception of RNZ and SD.

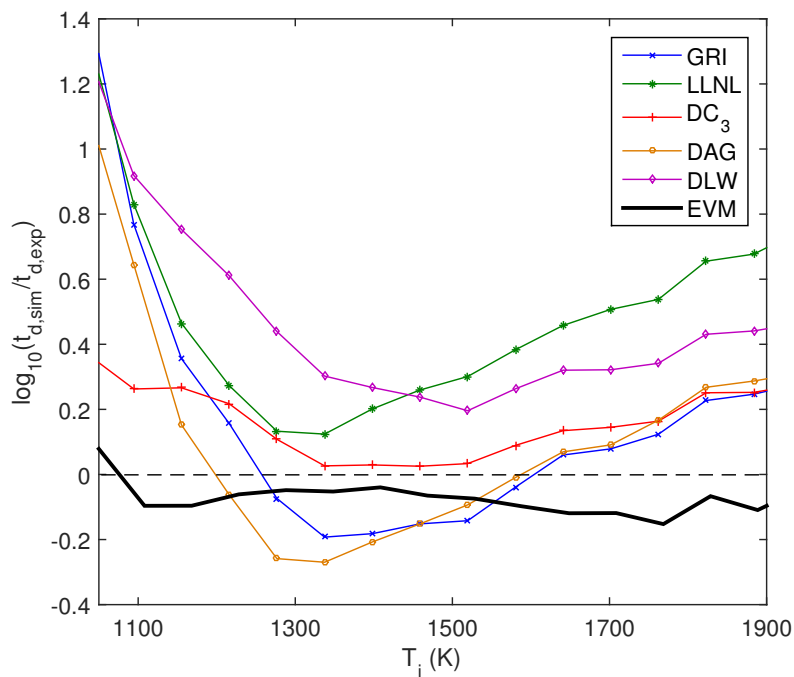


Figure C.3: Logarithmic variance between heritage chemical-kinetics mechanisms and experimental ignition-delay data plotted as a function of initial mixture temperature. The thick black line represents the variance between the proposed EVM method and experimental data.

Overall, the mean variance between ignition-delay times predicted by recent detailed chemical-kinetic mechanisms and experimental ignition-delay data is on the order of 50-100%, and considerably higher at low temperatures or off-stoichiometric conditions. This motivates the development of the data-driven induction-evolution model described in Section 4.3.2 that is, in the author's opinion, more reliable and efficient than the detailed chemical-kinetic mechanisms in Table 4.2, at least in terms of metrics described here.

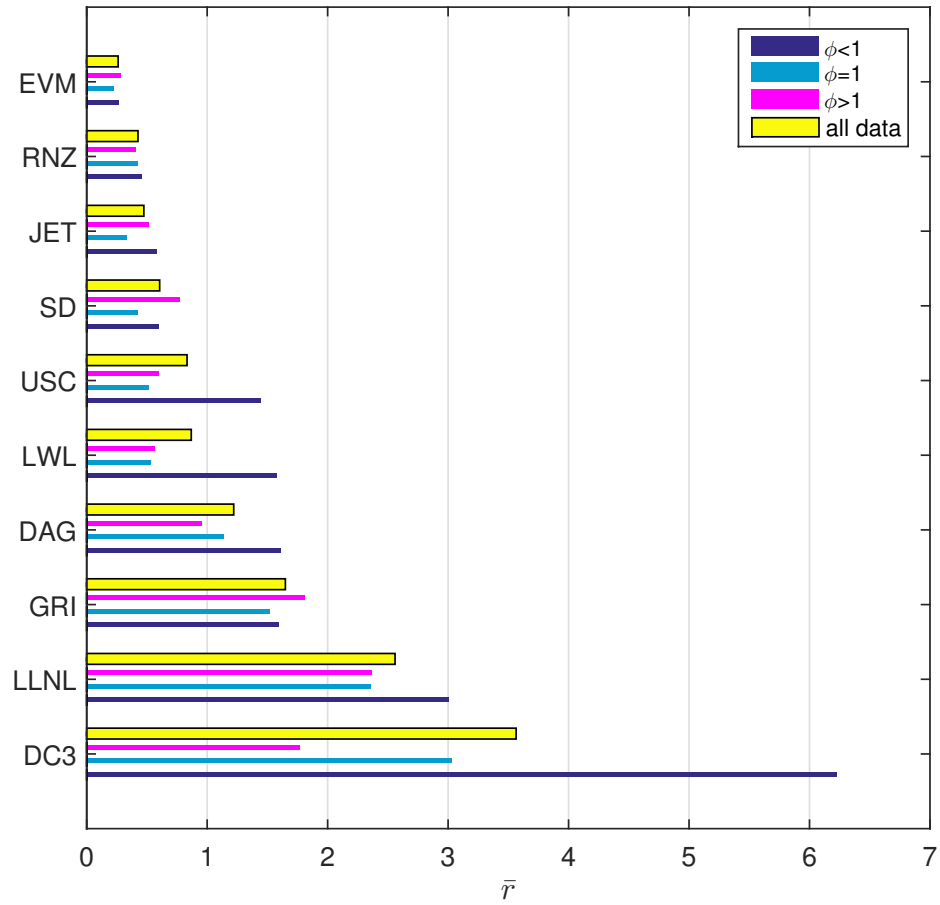


Figure C.4: Mean variance between experimental ignition-delay data and ignition models including detailed chemical-kinetic simulations and the proposed EVM model

## Appendix D

# Experimental conditions

Table D.1 contains the experimental conditions, including composition,  $J$  value, upper and lower plenum pressures, injector orifice, and corresponding run number for the experiments reported in this thesis. The freestream Mach number was measured to be  $M_\infty = 1.43 \pm 0.2$ , the freestream temperature 289 K and the plenum temperature 295 K.

Table D.1: Run parameters

Run	Inj.	$J$	$p_{0,\infty}$	$p_{0,j}$	$X_\infty$	$X_j$
			kPa	kPa		
1708	RN1	0.88	545	510	H2:0.02,NO:0.0015,N2:0.9785	F2:0.005,He:0.995
1712	RN1	0.96	531	558	H2:0.04,NO:0.003,N2:0.957	F2:0.01,He:0.90,,N2:0.09
1714	RN1	0.97	531	558	H2:0.02,NO:0.0015,He:0.04,N2:0.9385	F2:0.005,He:0.9,N2:0.095
1718	RN1	0.98	531	552	H2:0.02,NO:0.0015,He:0.04,N2:0.9385	F2:0.005,Ar:0.495,He:0.5
1719	RN2	0.96	531	545	H2:0.02,NO:0.0015,He:0.04,N2:0.9385	F2:0.005,He:0.9,N2:0.095
1720	RN2	0.95	531	552	H2:0.02,NO:0.0015,He:0.04,N2:0.9385	F2:0.005,Ar:0.995
1722	RN1	0.98	531	565	H2:0.02,NO:0.0015,He:0.04,N2:0.9385	F2:0.005,Ar:0.995
1724	RI1	0.96	531	552	H2:0.02,NO:0.0015,He:0.04,N2:0.9385	F2:0.005,He:0.86,N2:0.135